Electronic properties of graphene in high tilted magnetic fields

Francesca Chiappini

ISBN: 978-94-92380-09-8

Cover design by Irene Pepe

Electronic properties of graphene in high tilted magnetic fields

Proefschrift

ter verkrijging van de graad van doctor
aan de Radboud Universiteit Nijmegen
op gezag van de rector magnificus prof. dr. J.H.J.M. van Krieken,
volgens besluit van het college van decanen
in het openbaar te verdedigen op vrijdag 6 januari 2017
om 16.30 uur precies

door

Francesca Chiappini

geboren op 22 november 1987
te Genua, Italië

Promotor:	Prof. dr. ir. J.C. Maan
Copromotor:	Dr. S.R. Wiedmann
	Dr. U. Zeitler

Manuscriptcommissie:	Prof. dr. K. S.Novoselov
	Prof. dr. A. Fasolino
	Prof. dr. C. Stampfer
	(RWTH Aachen University, Duitsland)

Electronic properties of graphene in high tilted magnetic fields

Doctoral Thesis

to obtain the degree of doctor
from Radboud University Nijmegen
on the authority of the Rector Magnificus prof. dr. J.H.J.M. van Krieken,
according to the decision of the Council of Deans
to be defended in public on Friday, January 6, 2017
at 16.30 hours

by

Francesca Chiappini

Born on November 22, 1987
in Genoa, Italy

Supervisor:	Prof. dr. ir. J.C. Maan
Co-supervisors:	Dr. S.R. Wiedmann
	Dr. U. Zeitler

Doctoral Thesis Committee:	Prof. dr. K. Novoselov
	Prof. dr. A. Fasolino
	Prof. dr. C. Stampfer (RWTH Aachen University, Germany)

Preface

This little book represents a distillate of four intense years of hard and joyful work at the HFML. Before digging into the scientific content, I would like to spend some words to thank those who contributed to this work both on a professional and on a personal level.
First of all, I would like to thank the graphene group at the University of Manchester and especially Kostya Novoselov, for donating me the devices I studied in my experiments. It would have been impossible for me to write any of the following Chapters without these samples. I would like to specially thank Daniel Elias and Artem Mishchenko for bringing to Nijmegen most of the devices and for introducing me to the capacitance measurements.
I would like to thank Misha Titov for his help on the parallel field data and for his kind way of giving feedback on the paper drafts.
Then I would like to express my gratitude to the entire technical staff of the HFML for keeping the magnets running efficiently and for helping me with everything I needed for my experiments (probes, cryostat, helium, advise and good mood). A special thank to Lijnis and Michel for their help with the cryostats, vacuum equipment and for making the measurement probes and the sample holders. Hung, thanks for adapting the data acquisition program to my needs and enabling me to perform two experiments at the same time. Peter Albers, it was a pleasure to work with you in the clean room and with the evaporator. I really appreciated the fact that you were always available for questions and last minute troubleshooting. Thanks to Martin, Ine and Thera for your help with all the administrative issues.
A necessary thank to all the members of the Semiconductors and Nanostructures group for the help, the guidance and the collaborative attitude within the group.

Steffen, your contribution was essential to this work. I am extremely grateful for the huge amount of time (often during nights and weekends) you spent with me in front of the magnets, most of the data presented in this thesis were collected with your help. Andreas and Thomas, thank you for trying to bring the conversations back to English from time to time. I want to thank Erik and Genia for sharing with me their knowledge and secret tricks on how to handle graphene devices properly.

To my office mates (Bhawana, Peter, Veeru, Salvo, Maarten, Rava, Antol, and Jonathan), thank you for making the office a productive (and yet never boring) place. Maarten, thanks for translating the summary into Dutch and Lucas thank you for always finding time to read my drafts and to correct my English. More in general, the HFML has been a very pleasant and stimulating environment thanks to the entire staff. I enjoyed very much all the social events (lab trips, borrels, sport days, the glorious Christmas dinners) and the informal atmosphere of the lunch and coffee breaks. Thanks also to everyone who tried to make the lab an allergy-friendly place cooking special dishes for me or taking the not easy task of baking cakes free of anything an actual cake is usually made of. Of course, I want to thank especially those who had to deal with the least pleasant part of my allergies bringing me to an hospital (Uli), taking me out from an other one (Steffen) and staying with me during a strong reaction (Jonas). Jonas, thanks also for being always kind, smiling and up for a coffee, Thomas and Serg it was great fun going to Japan together. Now you can be happy forever! Laurens, thank you teaching me the real useful Dutch, never mind about the grammar. You pushed me to start talking Dutch in everyday life and, in return, you got some good laugh at my pronunciation. Het hangt er van af! Salvo, it was good fun annoying the rest of the office with our laud chatting in Italian!

But the past 4 years were great also because of the people I met outside the lab. Of course I want to thank the Postweg boys (Sean, Gerardo, Kang-suk and David) for making our house such a great place to live in. I really felt home with you guys! Sean, the space-ghost-train master, thank you for being such a creative partners in singing jingles about broccoli and kitchen routines. Gerardo, thank you for constantly showing me how fabulous life can be and for the updates about the world outside my cave.

I want to thank my capoeira group for the good energy they could transmit me at the end of a very tiring day, for the parties, the training and the good mood. Obrigada! Within this group I met very special people(Eva, Sophie, Teresa, Ken, Anthony) who soon became the core of the group of friends of my Nijmegen life.

Thérèse heel erg bedankt voor de gezellige sfeer tijdens de lessen. Ik heb veel

geleerd!
Questa tesi è l'atto finale di un lungo percorso di studi iniziato dieci anni fa a Genova. E vorrei cogliere l'occasione per ringraziare tutti i fisici genovesi per essere stati meravigliosi compagni di studio e di avventure. Prima di arrivare a questo punto ho dovuto passare Analisi 1, Fisica 2C e Meccanica quantistica 2 e meno male che c'eravate voi a condividere queste fatiche e ad aiutarmi con esercizi, integrali e piccole oscillazioni.
Quindi è giunto il momento di ringraziare le persone a me più vicine. Per prima cosa, vorrei rigraziare le mie Amiche, quelle nuove, quelle ritrovate, quelle che nonostante i mille chilometri di distanza sembra che siano sempre al mio fianco. Ila, incontrarti per caso è stata uno dei colpi di fortuna più grossi della mia vita. La tua compagnia ha reso piacevoli tutti i mesi di scrittura e le lunghe giornate di pioggia. Grazie per le risate, il cibo, il sostegno e congiuntivi. Ire, grazie per tutte le energie che hai investito nel nostro rapporto in questi anni di distanza, per essere una presenza discreta e affettuosa. Grazie per le avventure newyorkesi e la copertina di questa tesi. Ale, amico Gaggio, grazie per l'amicizia ininterrotta di tutti questi anni, per la vicinanza che sai esprimere e la pazienza che hai con me. Per tutte le telefonate che hanno sempre il potere di raddrizzare una giornata storta e farmi tornare il sorriso. Grazie per la spensiertezza e le risate dei viaggi insieme.
Jonathan, grazie per le vacanze in Francia e le cene del venerdì sera. Ma soprattutto, grazie per l'inaspettata e grandissima felicità di questi ultimi mesi.
Infine vorrei ringraziare la mia famiglia. Sono stati anni difficili per tutti ed è stato difficile per me essere così lontana. Michelino, zii, mamma e papà grazie per tutto l'affetto che mi date e la stima che non smettete mai di mostrare nei miei confronti. Vi voglio bene.

Francesca

Contents

CHAPTER 1

Introduction

Graphene is a two dimensional material made of carbon atoms arranged in a honeycomb lattice. Since its experimental discovery in 2004,[1] it has attracted continuous attention from the scientific community because of its remarkable structural and electronic properties, which are commonly described by means of superlatives.[2] Graphene is the strongest, stiffest and thinnest material; its carriers show the highest mobility and the longest mean free path. In addition, graphene is transparent to light and it conducts electricity better than copper. These qualities, which are only a few of the ones attributed to graphene, have made this flat material a promising candidate for many applications, stimulating comparisons with the development and diffusion of plastic in the 20th century. Nowadays, although the "killer" application has not been found yet,[3] graphene is expected or has already proven to have an impact as transparent and flexible conductive layer for touch screens[4] or solar cells,[5] or on printed electronics as a component for conductive inks.[6,7] It can be used as a coating to prevent the corrosion of metals[8] and as a selectively permeable membrane,[9,10] just to mention few areas of interest.

The discovery of graphene has defined a new class of materials, the two dimensional crystals,[11] which beforehand was thought to be non-existent.[12] These crystals are generally produced by mechanical exfoliation of a layered three dimensional crystal (graphite, in the case of graphene) and exhibit properties that are different from those of the bulk material. In the past years, the two dimensional form of many crystals (chalcogenides, layered transition metal oxides and many more) has been obtained, and nowadays metallic, insulating and semiconducting atomic layers are available for research.[13] Interestingly, these different two dimensional layers can be assembled into three dimensional stacks and the properties of these heterostructures can be designed and tuned by the choice of the materials and the thickness of the crystals that compose them or even by varying the angle between the crystallographic axes in each layer. The field of study of these so-called van der Waals heterostructures is in rapid growth and, among all the various materials employed in their fabrication, graphene plays a prominent role.[14]

In addition to the perspective applications and the interesting effects deriving from the combination of graphene and other materials in the van der Waals heterostructures, the intrinsic electronic properties of graphene continue to fascinate the scientific community. Indeed, graphene has been, for the past 12 years, a playground for scientists, who have intensively explored its peculiar properties and have revealed new exciting physics.

Graphene is a zero gap semiconductor and the low energy spectrum is linear as a function of the particle momentum. The charge carriers are regarded as chiral massless particles and are formally described by a Dirac-type Hamiltonian. The formalism of the quantum electrodynamics can be used to describe the physics of graphene and effects typical of relativistic particles, such as the Klein's tunnelling were predicted[15] and probed[16] in a condensed matter system.

When graphene is placed in an external magnetic field, the peculiar linear spectrum evolves into so-called relativistic Landau levels. At low magnetic fields, the Landau levels of graphene are four times degenerate, reflecting the spin and the valley degeneracy of the spectrum of the carriers. Interestingly, the linear dispersion and the chirality of graphene carriers lead to the presence of a level at zero energy which is equally shared by electrons and holes. The Landau level structure of graphene has lead to the discovery of a new type of quantum Hall effect, called *half*-integer or chiral quantum Hall effect.[17,18]

A high magnetic field lifts the Landau level degeneracy and new electronic states can be observed experimentally from the splitting of each level. The properties of these states and their possible spin and/or valley polarization are the main focus of two chapters of this thesis, and are addressed by means of transport and capacitance measurements in high (tilted) magnetic fields. These experimental techniques enable us to access the zero field density of states and that of the split Landau levels of graphene.

The experiments are performed on high quality field-effect transistors and capacitors, where graphene is placed in between two layers of hexagonal boron nitride. These devices are fabricated by researchers of the University of Manchester by exfoliating the crystals of the different materials and stacking the resulting atomic layers on top of each other. The encapsulation of graphene between the two insulating layers of hexagonal boron nitride, prevents undesired doping and contamination and preserves the high electronic quality of graphene, limiting the disorder in the devices. Therefore, it is possible to observe experimentally the Landau level splitting and address the contribution of interactions and Zeeman effect in determining it.

A key point in the discussion is that, because of the truly two-dimensional nature of graphene and the negligible spin-orbit coupling, the different mechanisms which contribute to the Landau level splitting depend on different components of the external magnetic field. The Zeeman splitting is due to the total magnetic field (B_T) applied to the devices, while interactions depends solely upon the component of the field perpendicular to the graphene plane. By tilting the sample with respect to the direction of the magnetic field by an angle θ and keeping the perpendicular component of the field ($B_\perp = B_T \cos\theta$) constant, one can tune the different effects and disentangle their contribution to the splitting of each level.

The high magnetic fields available at the HFML are a unique tool to investigate the electronic properties of graphene and probe the spin polarization of the electronic states. Indeed, the subtle effects due to the spin are often overshadowed by the prominent effects related to the orbital motion of the carriers (Landau quantization, electron-electron interactions) and high tilt angles are necessary to bring them to light. Since in our devices the splitting of the Landau levels is found experimentally to occur for $B_\perp$ between 4 and 17.5 T, high magnetic fields are necessary to achieve high angles, while keeping $B_\perp$ constant.

This thesis is organized as follows. In Chapter 2 we provide an introduction to the electronic properties of graphene and to the experimental techniques employed throughout this thesis. Chapters 3, 4 and 5 report the experimental results of this work.

In more detail, in Chapter 3 we examine the splitting of the Landau levels presenting both transport and capacitance data in a tilted magnetic field. We address the spin polarization of the electronic states resulting from the lifting of the Landau level degeneracy and compose a splitting scenario for all the observed Landau levels.

In Chapter 4 we focus exclusively on the lowest energy Landau level. We use capacitance spectroscopy to directly access the density of states and the chemical potential of the system, and examine the energy gaps associated to the electronic states observed once the degeneracy of the level is removed. The high tilt angles reached in these experiments enable us not only to probe, but also to change the spin polarization of the different states.

Chapter 5 reports magnetotransport experiments, where the graphene plane is parallel to the magnetic field ($\theta = 90°$). In this configuration, the external

magnetic field cannot couple to the motion of the carriers, therefore, the Landau levels do not form even at the highest fields. Since graphene is only one atom thick, these experiments enable us to address the effect of the Zeeman splitting on the transport properties of a truly two dimensional electron system.
This thesis is concluded by a general summary which describes the main findings of this work.

References

[1] K. Novoselov, A. Geim, S. Morozov, D. Jiang, Y. Zhang, S. Dubonos, I. Grigorieva, and A. Firsov, "Electric Field Effect in Atomically Thin Carbon Films", *Science* **306**, 5696, 666 (2004).

[2] A. K. Geim, "Status and Prospects", *Science* **324**, 1530–1534 (2009).

[3] W. Ren and H.-M. Cheng, "The global growth of graphene.", *Nature Nanotechnology* **9**, 10, 726–730 (2014).

[4] J. Ryu, Y. Kim, D. Won, N. Kim, J. S. Park, E.-K. Lee, D. Cho, S.-P. Cho, S. J. Kim, G. H. Ryu, H.-A.-S. Shin, Z. Lee, B. H. Hong, and S. Cho, "Fast synthesis of high-performance graphene films by hydrogen-free rapid thermal chemical vapor deposition.", *ACS Nano* **8**, 1, 950–6 (2014).

[5] K. Kim, S.-H. Bae, C. T. Toh, H. Kim, J. H. Cho, D. Whang, T.-W. Lee, B. Özyilmaz, and J.-H. Ahn, "Ultrathin organic solar cells with graphene doped by ferroelectric polarization.", *ACS applied materials & interfaces* **6**, 5, 3299–304 (2014).

[6] F. Withers, H. Yang, L. Britnell, A. P. Rooney, E. Lewis, A. Felten, C. R. Woods, V. Sanchez Romaguera, T. Georgiou, A. Eckmann, Y. J. Kim, S. G. Yeates, S. J. Haigh, A. K. Geim, K. S. Novoselov, and C. Casiraghi, "Heterostructures produced from nanosheet-based inks.", *Nano Letters* **14**, 7, 3987–92 (2014).

[7] D. J. Finn, M. Lotya, G. Cunningham, R. J. Smith, D. McCloskey, J. F. Donegan, and J. N. Coleman, "Inkjet deposition of liquid-exfoliated graphene and MoS 2 nanosheets for printed device applications", *J. Mater. Chem. C* **2**, 5, 925–932 (2014).

[8] S. Chen, L. Brown, M. Levendorf, W. Cai, S.-Y. Ju, J. Edgeworth, X. Li, C. W. Magnuson, A. Velamakanni, R. D. Piner, J. Kang, J. Park, and R. S. Ruoff, "Oxidation Resistance of Graphene-Coated Cu and Cu/Ni Alloy", *ACS Nano* **5**, 2, 1321–1327 (2011).

[9] S. P. Koenig, L. Wang, J. Pellegrino, and J. S. Bunch, "Selective molecular sieving through porous graphene.", *Nature Nanotechnology* **7**, 11, 728–32 (2012).

[10] M. Lozada-Hidalgo, S. Hu, O. Marshall, A. Mishchenko, A. N. Grigorenko, R. A. W. Dryfe, B. Radha, I. V. Grigorieva, and A. K. Geim, "Sieving

hydrogen isotopes through two-dimensional crystals.", *Science* **351**, 6268, 68–70 (2016).

[11] K. S. Novoselov, D. Jiang, F. Schedin, T. J. Booth, V. V. Khotkevich, S. V. Morozov, and a. K. Geim, "Two-dimensional atomic crystals.", *Proceedings of the National Academy of Sciences of the United States of America* **102**, 30, 10451–10453 (2005).

[12] N. D. Mermin, "Crystalline Order in Two Dimensions", *Physical Review* **176**, 1, 250–254 (1968).

[13] M. Xu, T. Liang, M. Shi, and H. Chen, "Graphene-like two-dimensional materials.", *Chemical Reviews* **113**, 5, 3766–98 (2013).

[14] A. K. Geim and I. V. Grigorieva, "Van der Waals heterostructures.", *Nature* **499**, 7459, 419–25 (2013).

[15] M. I. Katsnelson, K. S. Novoselov, and a. K. Geim, "Chiral tunnelling and the Klein paradox in graphene", *Nature Physics* **2**, 9, 1986 (2006).

[16] A. F. Young and P. Kim, "Quantum interference and Klein tunneling in graphene heterojunctions", *Nature Physics* **5**, 3, 13 (2008).

[17] K. S. Novoselov, A. K. Geim, S. V. Morozov, D. Jiang, M. I. Katsnelson, I. V. Grigorieva, S. V. Dubonos, and A. A. Firsov, "Two-dimensional gas of massless Dirac fermions in graphene", *Nature* **438**, 7065, 197–200 (2005).

[18] Y. Zhang, Y.-W. Tan, H. L. Stormer, and P. Kim, "Experimental observation of the quantum Hall effect and Berry's phase in graphene", *Nature* **438**, 7065, 201–204 (2005).

CHAPTER 2

Introduction to graphene and to the experimental techniques

2.1 Introduction to graphene

Graphene is a two dimensional (2D) material made of carbon atoms arranged in a planar honeycomb lattice. Graphene constitutes the fundamental building blocks of graphite, which is made of a stack of graphene planes held together by van der Waals interactions. Due to the weak nature of these bonds, it is possible to mechanically exfoliate small pieces of graphite down to a single atomic layer and obtain graphene.[1]

The history of the investigation of the electronic properties of graphene begins in 1947, when Wallace calculated the band structure of graphene using a tight binding approach.[2] It took more than half a century before graphene was isolated for the first time and became accessible for experimentalists. Since then, this material has attracted much attention from the scientific community, stimulating both fundamental and applied research.[3]

In the following sections we describe the electronic properties of graphene from a theoretical point of view. We do not aim for a complete description, which can be found in several review articles and textbooks.[4–6] We address the basic concepts that are relevant in order to understand the results reported in the following chapters.

2.1.1 Honeycomb lattice and band structure

The lattice structure of graphene is a consequence of the sp^2 hybridization of carbon atoms. The atomic orbitals $2s$, $2p_x$ and $2p_y$ hybridize forming strong bonds between the atoms. These bonds, called σ-bonds, are planar and form an angle of 120° between each other. The length a of the σ-bonds, and therefore the distance between two neighbouring atoms is $a = 1.42$ Å. The remaining $2p_z$ orbital is perpendicular to the plane and forms a π-bond.

The carbon atoms occupy the corners of the hexagons composing the honeycomb structure, which is described as a triangular Bravais lattice with two atoms in the basis (see Figure 2.1 (a)). One representation of the triangular lattice is provided by the vectors $\boldsymbol{a_1} = a/2(3, \sqrt{3})$ and $\boldsymbol{a_2} = a/2(3, -\sqrt{3})$. The carbon atoms occupy the inequivalent sites A and B.

In the reciprocal space, the first Brillouin zone is hexagonal and at the corners one finds the K and K' inequivalent points (see Fig.2.1(b)). These points occupy the positions defined by the vectors

$$\boldsymbol{K} = (\frac{2\pi}{3a}, -\frac{2\pi}{3\sqrt{3}a}) \qquad \boldsymbol{K'} = (\frac{2\pi}{3a}, \frac{2\pi}{3\sqrt{3}a}). \tag{2.1}$$

The K and K' points in the Brillouin zone play a crucial role for the electronic properties of graphene since the low energy excitations occur in the vicinity of these points.

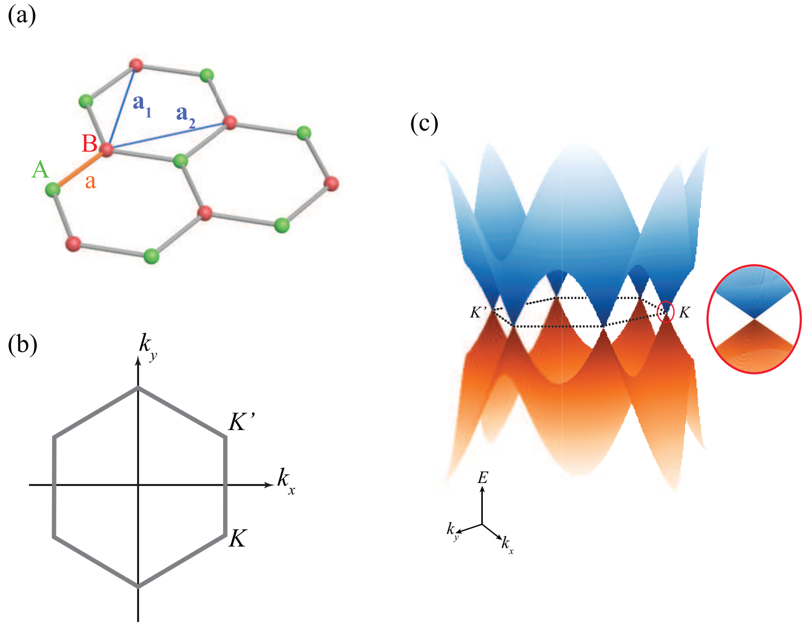

Figure 2.1: *The lattice and the band structure of graphene. (a): Graphene honeycomb lattice. The vectors $\boldsymbol{a_1}$ and $\boldsymbol{a_2}$ (in blue) define the triangular Bravais lattice. The nearest neighbours are separated by the distance a. The two atoms of the basis occupy the sites A and B, defined as the green and red spheres, respectively. (b): First Brillouin zone of graphene with the K and K' points. (c): Graphene band structure. The valence (orange) and conduction band (blue) touch each other at the six corners of the Brillouin zone. Inset: Zoom of the linear dispersion around the K point.*

The band structure of graphene can be calculated in the tight-binding approximation considering the π states only and the hopping between nearest neighbours. This approach was first used by Wallace in 1947 and, despite its simplicity, captures the essential feature of the electronic properties of graphene: the linear dispersion around the K and K' points.
Solving this tight binding problem, one finds[2]

$$E(k_x,k_y) = \pm t\sqrt{3 + 2\cos(\sqrt{3}k_y a) + 4\cos(\frac{\sqrt{3}}{2}k_y a)\cos(\frac{3}{2}k_x a)} \tag{2.2}$$

where $t \approx -3\,\text{eV}$ is the hopping parameter between the nearest neighbour sites.

The dispersion of eq.2.2 is plotted as a function of the wave vectors k_x and k_y in figure 2.1 (c). The conduction and the valence band (+ and − signs in eq.2.2, respectively) touch each other at the corners of the Brillouin zone, called Dirac points. For pristine graphene, the valence band is completely filled while the conduction band is completely empty thus, the Fermi energy is exactly at the Dirac points. Therefore, undoped graphene is regarded as a zero gap semiconductor.

Around the Dirac points, say K, the dispersion is conical (see the zoomed inset of Figure 2.1 (c)) and can be described by

$$E(\boldsymbol{q}) = \pm\hbar v_F(\boldsymbol{k} - \boldsymbol{K}) = \pm\hbar v_F \boldsymbol{q} \tag{2.3}$$

where $\boldsymbol{q} = \boldsymbol{k} - \boldsymbol{K}$ is the quasiparticle momentum and $v_F = \frac{3a|t|}{2\hbar} \approx 10^6$ m/s is the Fermi velocity at the Dirac points, which does not depend on the momentum. Figure 2.1 (c) shows that the states at the inequivalent points K and K' are degenerate in energy. Such a twofold degeneracy is referred to as valley degeneracy.

The density of states (DOS) for a 2D material can be calculated as

$$DOS(E) = \frac{d\mathcal{N}(E)}{dE} \tag{2.4}$$

where $\mathcal{N}$ is the number of states per unit area in a certain energy band below the energy E. Using the dispersion in eq.2.3 one can derive DOS for graphene

$$DOS(E) = \frac{8\pi|E|}{h^2 v_F^2} \tag{2.5}$$

which is shown in Figure 2.2. The DOS depends linearly on energy and is symmetric for electrons and holes. In the case of pristine graphene, the DOS vanishes at the Dirac point ($E = 0$).

Given the DOS, we can calculate the electron density n

$$n = \int_0^\infty DOS(E) f(E)\, dE \tag{2.6}$$

where $f(E)$ is the Fermi distribution function $(1 + e^{(E-\mu)/(k_B T)})^{-1}$, μ is the chemical potential of the system, k_B is the Boltzmann constant and T is the temperature. In the limit of zero temperature, μ equals the Fermi energy E_F of the system. For Fermi distribution function, one has $f(E) = 1$ for $E < E_F$ and $f(E) = 0$ for $E > E_F$. Solving the integral in eq.2.6 gives $n = 4\pi E_F^2/(h^2 v_F^2)$. Thus, the Fermi energy in graphene depends on the square root of the charge carrier concentration

$$E_F = \hbar v_F \sqrt{\pi n}\,. \tag{2.7}$$

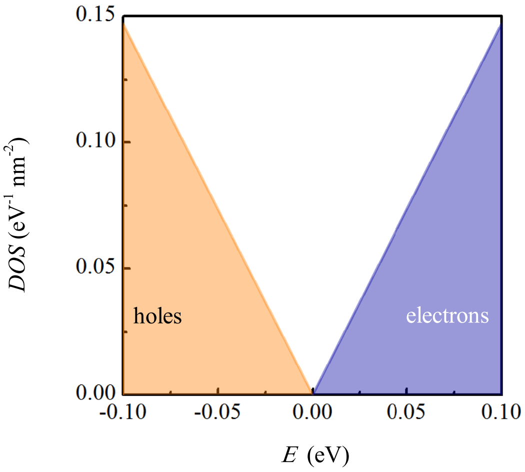

Figure 2.2: *DOS as a function of energy for pristine graphene at $T = 0$. The orange area indicates the DOS for holes and the blue area the one for electrons.*

The linear dispersion in eq.2.3 resembles the one of massless relativistic particle moving with a constant velocity, as in the case of photons with $v_F \approx \frac{1}{300}c$. Formally, the low energy excitations within one valley can be described by the Dirac Hamiltonian

$$\hat{H} = \hbar v_f \boldsymbol{\sigma} \cdot \boldsymbol{q} \tag{2.8}$$

$\boldsymbol{\sigma}$ are the Pauli matrices in their 2D form. Here, the Pauli matrices do not describe the actual spin of electrons but the degree of freedom introduced by the two different sublattices. In this formalism, two states correspond to the sublattices A and B, which are referred to as pseudospin. The eigenstates of the Hamiltonian in eq.2.8 are two component spinors of the form

$$\Psi = \begin{pmatrix} \psi_A \\ \psi_B \end{pmatrix} \tag{2.9}$$

where $\psi_{A,B}$ is the wavefunction for electrons on the sublattice A or B, respectively. For carriers in graphene, one can define the quantity *chirality* which is the projection of the pseudospin in the direction of the motion of the carriers.[7] At the Dirac point, the chirality is positive for electrons and negative for holes and testifies that electrons and holes with opposite momenta originate from the same sublattice.[3,4] The chiral nature of charge carriers in graphene has consequences on the formation of the energy levels of the carriers in an external magnetic field (see Section 2.3).

2.2 Graphene based ambipolar field-effect transistors

The peculiar band structure and *DOS* of graphene can be studied by means of transport measurements using graphene based ambipolar field-effect transistors (FETs).[1] In such devices, the chemical potential can be tuned through the valence and the conduction band by means of a back gate, allowing one to access both the hole dominated and the electron dominated transport.

In our devices, the graphene is encapsulated between two thin layers of hexagonal boron nitride (hBN). This material is an insulator which is used in the devices in order to preserve the electronic quality of the graphene[8] (see Section 2.5).

In order to make a FET, a heterostructure of hBN/graphene/hBN is placed on top of a heavily doped Si/SiO_2 wafer (see Figure 2.3 (a)). The graphene and the Si substrate are coupled capacitively, therefore, by applying a dc voltage between them it is possible to induce charge carriers in the graphene. The Si substrate acts as a back gate and the induced charge carrier density n is proportional to the voltage V_G applied between the graphene and the Si substrate

$$n = \alpha V_G \tag{2.10}$$

where the coefficient α gives the efficiency of the gate and depends on the thickness on both SiO_2 and hBN and their dielectric constants. Typically, our devices have 280 nm of SiO_2 and few tens of nm of hBN leading to a value for α between 4×10^{14} and $6 \times 10^{14}\,\mathrm{m^{-2}V^{-1}}$, depending on the device. These values are found experientially from the periodicity of the Shubnikov-de Haas oscillations at a fixed magnetic field (as an example, see Section A.1 in Appendix A, where this calculation is performed on data obtained from a graphene based capacitor).

The graphene is shaped into a Hall bar geometry by electron beam lithography and successive etching, and it is connected to 6 electrical contacts (see Figure 2.3 (b)). These devices have a typical length of approximately $10\,\mu$m. The width of the channel W and the distance between the voltage contacts L are approximately 1.5 and $3\,\mu$m, respectively.

In a transport experiment an ac current I in the order of $10 - 100$ nA is sent through the device and the voltage drop along the current direction (V_{xx}) is measured. One obtains the longitudinal resistance of the sample as

$$R_{xx} = \frac{V_{xx}}{I}. \tag{2.11}$$

Figure 2.3(c) shows a typical trace of R_{xx} as a function of the gate voltage V_G at 4.2 K. The signal is characterized by a sharp peak which reaches its maximum

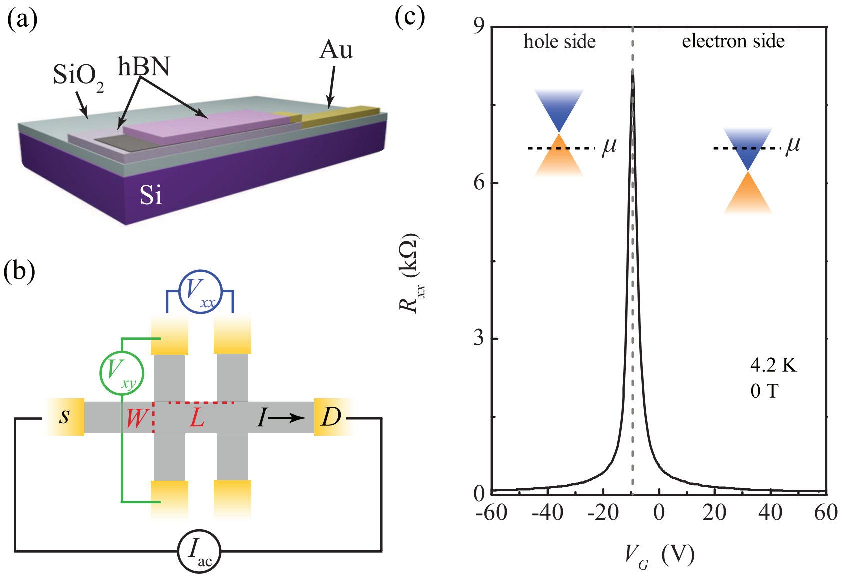

Figure 2.3: *General structure of graphene-based FETs and zero field transport. (a): Schematic representation of a lateral section of a device. The graphene (grey area) is sandwiched between two layers of hBN and connected to an Au contact. The whole structure is placed on top of a Si/SiO$_2$ wafer. (b) Hall bar geometry of the devices. The current I flows between the source and drain contacts (s and D, respectively). W and L are the width of the channel and the distance between the voltage contacts, respectively. V_{xx} is the potential drop along the current direction, V_{xy} is the voltage drop perpendicular to it. (c) Gate sweep at 0 T and 4.2 K. R_{xx} is measured as function of the gate voltage V_G. The CNP occurs at $V_{CNP} \approx -9.5$ V.*

as the chemical potential μ is swept through the charge neutrality point (CNP), where $n = 0$. For all the devices considered in this work the value of R_{xx} and the CNP was found to be between 5 and 10 kΩ for temperatures down to 1.4 K. On both sides of the CNP, when μ is either in the valence band or in the conduction band, R_{xx} decreases rapidly to reach values of few hundreds Ohms for high V_G.

In the studied samples, the maximum of R_{xx} occurs at $V_G \neq 0$ V which indicates the presence of doping in the device.[9] Therefore, the actual charge carrier concentration is described by $n = \alpha(V_G - V_{CNP})$, where V_{CNP} is the gate voltage value of the CNP.

Knowing the longitudinal resistance and the geometrical factors L and W for the device, one can calculate the resistivity

$$\rho_{xx} = R_{xx}\frac{W}{L} \tag{2.12}$$

and the longitudinal conductivity $\sigma_{xx} = 1/\rho_{xx}$. A typical trace of σ_{xx} is shown in Figure 2.4. σ_{xx} exhibits a minimum at the CNP and increases as the chemical potential is swept into the valence (conduction) band. At high values of n, σ_{xx} is linear. Therefore, in the high n region, one can apply the semi-classical Drude model in order to describe σ_{xx}

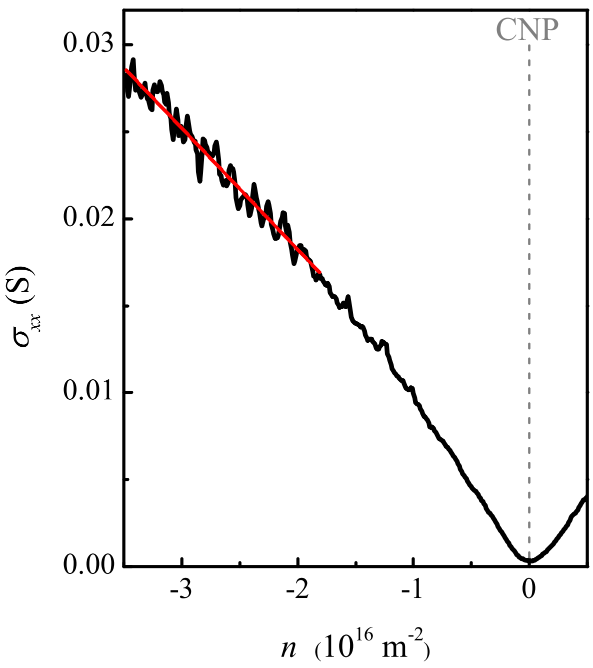

Figure 2.4: *Conductivity of a graphene FET (black line) as a function of the charge carriers concentration n at $1.4\,K$. The red line is the linear fit to the data performed in order to extract the mobility of carriers μ_n.*

$$\sigma_{xx} = ne\mu_n \tag{2.13}$$

where μ_n is the mobility of charge carriers. By performing a linear fit to the data (red line in Figure 2.4), one can obtain μ_n. For this specific sample we obtain $\mu_n \approx 40000\,\mathrm{cm}^{-2}\mathrm{V}^{-1}\mathrm{s}^{-1}$.

When one of the devices is placed in a perpendicular magnetic field, the Hall effect produces a voltage drop V_{xy} in the direction perpendicular to the current flow (see Figure 2.3 (b)). The Hall resistance R_{xy} is defined as

$$R_{xy} = \frac{V_{xy}}{I} = \rho_{xy}\,. \tag{2.14}$$

ρ_{xx} (defined in eq.2.12) and ρ_{xy} are the components of the resistivity tensor in a magnetic field and can be used to calculate the components of the conductivity tensor as (see Ref. 10 for a complete description)

$$\sigma_{xx} = \frac{\rho_{xx}}{\rho_{xx}^2 + \rho_{xy}^2},\ \sigma_{xy} = \frac{\rho_{xy}}{\rho_{xx}^2 + \rho_{xy}^2} \tag{2.15}$$

These relationships can be inverted in order to obtain the resistivities given the values of the longitudinal and Hall conductivities σ_{xx} and σ_{xy} as

$$\rho_{xx} = \frac{\sigma_{xx}}{\sigma_{xx}^2 + \sigma_{xy}^2},\ \rho_{xy} = \frac{\sigma_{xy}}{\sigma_{xx}^2 + \sigma_{xy}^2}. \tag{2.16}$$

2.3 Graphene in a magnetic field

2.3.1 Landau levels in graphene

When graphene is placed in a perpendicular magnetic field, the energy dispersion changes dramatically owing to the Lorentz force experienced by the charge carriers. The continuous bands described in eq.2.2 transform into a series of discrete energy levels, called Landau levels (LLs). The dispersion of these levels can be calculated substituting the momentum operator in eq.2.8 with $\boldsymbol{q} - e\boldsymbol{A}$, where $\boldsymbol{A}$ is the vector potential chosen in the Landau gauge $\boldsymbol{A} = (0, Bx, 0)$. The eigenvalues of the modified Hamiltonian are the LLs for the system. In the case of graphene the LLs have the dispersion[11]

$$E = \operatorname{sign}(M) v_F \sqrt{2e\hbar B|M| + \frac{1}{2} \pm \frac{1}{2}} \tag{2.17}$$

where $M = 0, \pm 1, \pm 2, \pm 3, \ldots$ is called Landau level index, which is positive for the electrons and negative for the holes. The square root dependence on the magnetic field is a direct consequence of the linear relationship between energy and momentum reported in eq.2.3 and therefore the Landau levels of graphene are referred to as relativistic Landau levels. The ±1/2 term is due to the chirality of carriers. Unlike the Landau levels for other 2D systems with a parabolic dispersion, the LLs for graphene are not equidistant. One can introduce the index $N = \mathrm{sign}\,(M)(|M| + 1/2 \pm 1/2) = 0, \pm 1, \pm 2, \pm 3, \ldots$ and obtain the energy levels

$$E_N = \mathrm{sign}\,(N) v_F \sqrt{2e\hbar B|N|} \tag{2.18}$$

shown in Figure 2.5 (a). The blue (orange) lines represents the energy levels for the electrons (holes). One consequence of the linear dispersion and of the chirality of charge carriers in graphene, is the presence of the $N = 0$ level populated equally by electrons and holes. For simplicity, in the following parts, when talking about Landau levels in graphene, we will refer only to the energy levels reported in eq.2.18 and to the index N.

The LLs in graphene are four fold degenerate, two times for spin and two times for valley. Each level can host a number of carriers given by

$$n_L = \frac{eB}{h} \tag{2.19}$$

thus, given a fixed density of charge carriers n, the external magnetic field defines the number of filled Landau levels. This number is called filling factor and is defined as

$$\nu = \frac{n}{n_L} = \frac{nh}{eB}. \tag{2.20}$$

The eigenstates of the Hamiltonian in a magnetic field are also two component wave functions. For $N \neq 0$, an electron residing in one valley has the same probability to occupy both sublattices, while for the $N = 0$ level the carriers in one valley can reside only on one sublattice. Therefore, among the graphene LLs, the $N = 0$ LL represents a special case since the valley index (K or K') corresponds to the sublattice index (A or B) in real space.

2.3.2 The quantum Hall effect in graphene

The density of states of a 2D system in a perpendicular magnetic field can be described by a series of delta functions. In case of graphene, these are centred at the energy values described by eq.2.18.

In a real sample, however, the disorder induces a broadening of the levels. The shape of the LLs can be approximated by a Gaussian, as shown schematically in Figure 2.6. The broadening of each level, Γ, is defined as the full width at half maximum (FWHM) of each peak.

The LLs host two types of electronic states: localized and extended states. The first occupy the tails of each level (shaded areas in Figure 2.6) and do not contribute to the electrical conduction. The latter occupy the central part of

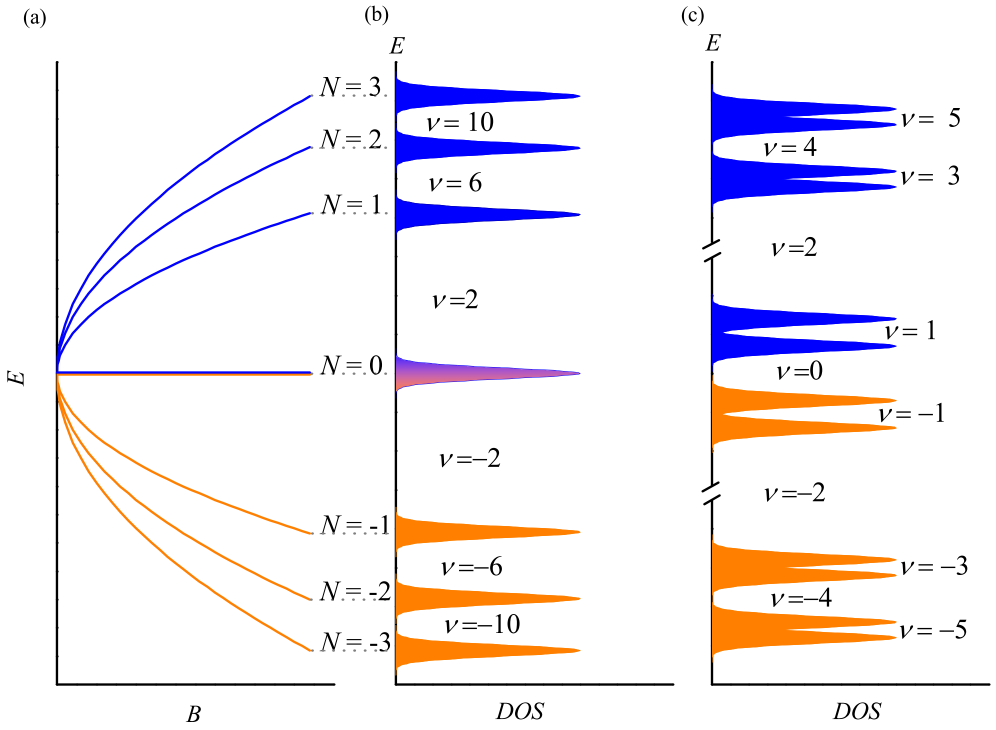

Figure 2.5: *Landau levels of graphene. (a): Energy of the LLs for $|N| \leq 3$ as a function of the magnetic field for electrons (blue lines and positive values of N) and holes (orange lines and negative values of N). (b) Four fold degenerate Landau levels depicted as broadened peaks in the DOS as a function of energy. (c) Lifting of the Landau level degeneracy for the $|N| \leq 1$ levels. Each level is split into 4 distinct ones leading to the observation of the additional filling factors $\nu = 0, \pm 1, \pm 3, \pm 4$ and ± 5. This schematic picture shows that different ν are associated to different energy gaps, as found experimentally (see Chapter 3).*

each level (light blue areas in Figure 2.6) and are responsible for the electrical conduction.

If the separation between the Landau levels is larger than their broadening and than the thermal energy, one can observe the quantum Hall effect (QHE). The phenomenology of the QHE is a direct consequence of the 2D nature of graphene making that at high fields there are no states between LL, and the distinction between localized and extended states. When the chemical potential lies within the extended states, the system is conducting and both σ_{xx} and σ_{xy} are non

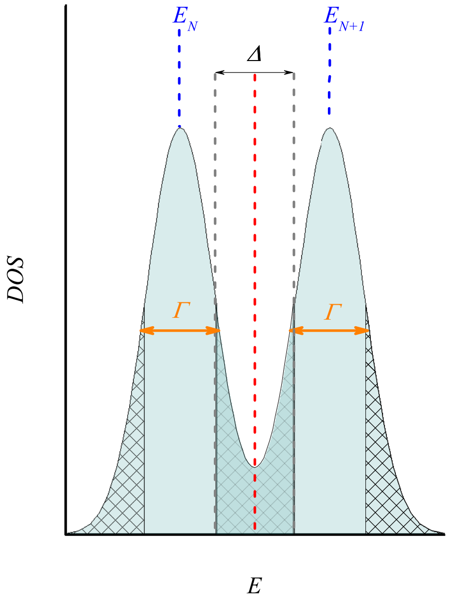

Figure 2.6: *Schematic representation of two broadened LLs depicted as Gaussian peaks occupied by extended states (light blue areas) and localized states (shadowed areas) and centred around the energy values* E_N *and* E_{N+1}*. The broadening of each level is given by the FWHM* Γ.

zero (and therefore, following eq.2.16, ρ_{xx} and ρ_{xy} have a finite value as well). When the chemical potential crosses a region of the *DOS* of localized states, the conduction through the bulk is zero ($\sigma_{xx} = 0$). The bulk of the system is insulating and conduction occurs only through dissipation-less edge states. In this regime the longitudinal resistivity is $\rho_{xx} = 0$ and the Hall resistivity (or conductivity σ_{xy}) is quantized

$$\rho_{xy} = \frac{h}{\nu e^2} = \sigma_{xy}^{-1} \tag{2.21}$$

where ν is the filling factor defined in eq.2.20. Remarkably, the quantization of ρ_{xy} does not depend on the material and on the size of the device under investigation.[12]

The QHE for graphene is different from that of conventional 2D system. In the following part we describe the characteristics of the QHE in graphene.

A typical magnetotransport measurement at low magnetic field and low temperature for a graphene based FET is shown in Figure 2.7. The longitudinal

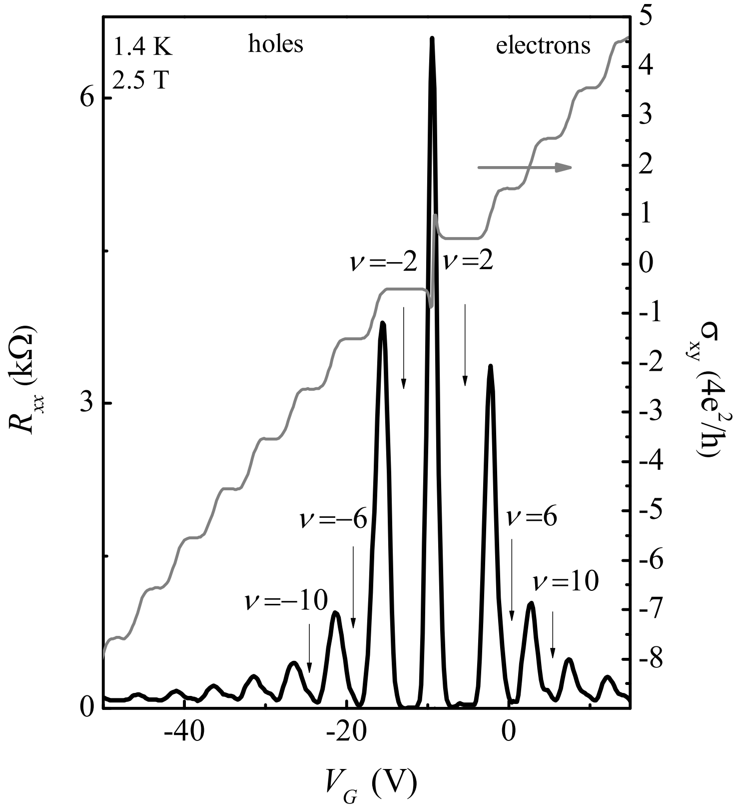

Figure 2.7: *Magnetotransport of single layer graphene at* 2.5 *T and* 1.4 *K and the observation of the half integer quantum Hall effect.* R_{xx} *(black trace) and* σ_{xy} *as a function of the back gate voltage.*

resistance and the Hall conductivity are plotted as a function of the gate voltage at 2.5 T. R_{xx} shows several oscillations and σ_{xy} presents several steps. The plateau values of σ_{xy} are given by

$$\sigma_{xy} = \pm\frac{4e^2}{h}(|N| + \frac{1}{2}) \tag{2.22}$$

where the factor 4 is given by the spin and valley degeneracy of the LLs, N is the index defined in eq.2.18 and the 1/2 term is a consequence of the Berry phase for graphene.[13–15]

Therefore, at low magnetic fields, the QHE in graphene occurs at the filling factors $\nu = \pm 4(|N| + 1/2)$ and experimentally one can observe the sequence

$$\nu = \pm 2, \pm 6, \pm 10 \ldots \tag{2.23}$$

for $N = 0, \pm 1, \pm 2, \pm 3, \ldots$. This sequence is a direct consequence of the quantization of the DOS schematically depicted in Figure 2.5 (b). The step of four in between the ν reflects the four fold degeneracy of the LLs, while the fact that at low density the first filling factors observed are $\nu = \pm 2$, is a direct consequence of the presence of the $N = 0$ LL. The experimental observation of the filling factor sequence reported in eq.2.23 is considered as the conclusive evidence of the Dirac or chiral nature of charge carriers in graphene.[15,16]

The QHE in graphene is different from the one occurring in conventional 2D systems with a parabolic dispersion because of the presence of the field-independent $N = 0$ Landau level shared between electrons and holes. In order to emphasize this fundamental difference, the QHE in graphene has been called *half*-integer quantum Hall effect as the Hall conductivity is quantized according to eq.2.22. Moreover, in contrast to the other 2D systems, for which the quantum Hall effect is a low temperature phenomenon, graphene shows the QHE up to room temperature.[17]

2.3.3 Lifting of the Landau level degeneracy

Soon after the discovery of the half-integer QHE, several works employing transport experiments in high magnetic fields, reported the observation of integer filling factors outside the sequence of eq.2.23. In particular, new plateaus in σ_{xy} were observed at $\nu = 0, \pm 1$ and ± 4. The presence of these states was explained as a consequence of the lifting of the LL degeneracy induced by high magnetic fields.[18–21] In this picture, each spin and valley degenerate LL, can split into four non degenerate ones leading to the observation of three additional integer filling factors, as schematically depicted in Figure 2.5 (c).

In order to understand why the lifting of the degeneracy can occur in first place, one has to consider that the eigenvalues reported in eq.2.18 are obtained for a Hamiltonian which does not explicitly consider the spin of the carriers or the interactions between them. Including these terms, the dispersion of eq.2.18 and consequently the sequence of ν (eq.2.23) are modified. As an example, if the spin of electrons is taken into account, an external magnetic field B lifts the degeneracy dependent on the spin degree of freedom, and the electronic states with opposite spin will be separated in energy by the Zeeman effect

$$E_Z = g\mu_B B = 1.2\,[\mathrm{KT}^{-1}] \times B \tag{2.24}$$

where $g = 2$ is the g-factor in absence of strong interactions and μ_B is the Bohr magneton.

These first experiments were performed on FETs where the graphene was deposited directly onto the SiO_2 layer and were characterized by low charge carriers mobilities ($\mu_n < 20000\,\mathrm{cm^{-2}V^{-1}s^{-1}}$). The extraction of the energy gaps associated to the states reveals two different regimes; when the partial lifting of the degeneracy of one Landau level occurs, as in the cases of $\nu = 0$ in Ref. 20 and $\nu = 4$ in Ref. 18, this is attributed to the single particle Zeeman effect. When the full splitting of one level occurs and three additional filling factors are observed (as in the case of the $N = 0$ LL with $\nu = 0$ and ± 1 in Ref. 19), energy gaps larger than E_Z are observed. In these cases, the Zeeman effect alone cannot explain the splitting of the levels.

Later experiments performed on higher quality devices (suspended and hBN supported) with higher carrier mobilities, revealed filling factors occurring at all integer values indicating the complete splitting of the levels and the lifting of both spin and valley degeneracies for all LLs. The full splitting of the LLs can be explained only if one takes into account the electron-electron interactions. This hypothesis is supported by the experimental observation of large energy gaps associated to the newly observed states.[22–27]

The comparison between the different experiments indicates that the quality of the devices influences the splitting of the LLs. For low quality devices, the splitting is partial and induced by the single particle Zeeman effect and high magnetic fields ($> 20\,\mathrm{T}$) are required in order to observe it. Instead, for higher quality devices, electron-electron interactions induce the complete splitting of all levels, which occurs at much lower fields (see also Chapter 3 and 4).

2.3.4 Quantum Hall Ferromagnetism

The role of interactions in the splitting mechanism has been addressed extensively from a theoretical point of view. Many theoretical works[5, 28–36] suggested that the splitting of the LLs can occur spontaneously to minimize the Coulomb repulsion between electrons. In this picture, if disorder in the sample is sufficiently low, the system minimizes the electrostatic repulsion forming states where the symmetries of the system (in the case of graphene: spin and valley) are spontaneously broken and energy gaps are formed at any integer ν.[28] A formal description is provided by the so-called quantum Hall ferromagnetism model.[37] In the quantum Hall ferromagnetism picture, the splitting of the Landau levels is governed by the Coulomb interaction between electrons given by

$$E_C = \frac{e^2}{4\pi\epsilon_0\epsilon_r\ell_B} = \frac{643}{\epsilon_r}\,[\mathrm{KT^{-1/2}}] \times \sqrt{B} \tag{2.25}$$

where ϵ_r is the dielectric constant, which depends on the media surrounding the graphene[5] and $\ell_B = 26\,\mathrm{nm}/\sqrt{B[\mathrm{T}]}$ is the magnetic length.
This theory, however, does not predict the properties of the states obtained by the splitting of the LLs, since the Coulomb interaction does not distinguish between the different valley or spin states. Indeed, the selection of a specific state, e.g. valley or spin polarized, is determined by the competition of different effects.[28, 29] The first one is the already mentioned Zeeman effect (eq.2.24) which will favour a spin polarized state.
Another mechanism relevant for the selection of a specific state is provided by the lattice scale anisotropies which describe electron-electron interactions and electron-phonon interactions at a lattice scale.[38–40] These terms find an origin, for instance, in the Coulomb repulsion between electrons residing on the same lattice site, or on different sites within the same sublattice or within opposite sublattices.
The lattice scale anisotropies are predicted to scale in first approximation as[38, 39]

$$E_{LS} \approx E_C \frac{a}{\ell_B} \approx \frac{3.5}{\epsilon_r}[\mathrm{KT}^{-1}] \times B \tag{2.26}$$

where a is the lattice spacing.
Depending on the competition between E_Z and E_{LS}, a certain ground state prevails but, since the energy scales typical of these interactions are comparable, it is difficult to predict which kind of polarization is realized at each filling factor.[29]
The quantum Hall ferromagnetism model for graphene has been confirmed experimentally by Young and co-workers[22] who have addressed the spin polarization of the broken symmetry states by means of transport experiments in tilted magnetic fields. However, many questions still remain open: what is the interplay between single particle and many-body effects? How does the quality of the devices influence the different states? Is the influence of E_Z and E_{LS} the same for all LLs? A part of this thesis is devoted to addressing these questions and the experimental results are presented in Chapter 3 and 4.

2.3.5 Thermally activated transport

The different energy scales discussed in the previous sections determine the size Δ_ν of the energy gaps associated to each filling factor. As an example, the gap size for filling factor 2 is given by the distance in energy between the levels $N = 0$ and $N = 1$ reduced by the broadening of each level (see Figure 2.6). Assuming the same field independent broadening Γ for both $N = 0$ and $N = 1$

LLs, the gap is

$$\Delta_2 = E_{N=1} - E_{N=0} - \Gamma = v_F\sqrt{2e\hbar B} - \Gamma. \tag{2.27}$$

Therefore, by measuring the size of energy gaps and their dependence on the magnetic field, one can obtain information about the underlying mechanism. In Chapters 3 and 4 we address the splitting of the Landau levels and the properties of the resulting electronic states through the study of the energy gaps.

One way to obtain Δ_ν for the different filling factors, is to perform thermally activated transport measurements. The gaps can be extracted from the temperature dependence of the oscillations in R_{xx} in the so-called temperature activated regime. As shown in figure 2.7 and 2.8 (a), each filling factor corresponds to a minimum in R_{xx}. In Figure 2.8 (a), we show R_{xx} as a function of V_G at 17.5 T for different temperatures between 1.4 and 18 K. At the lowest temperatures we observe the lifting of the LL degeneracy at $\nu = -1, -3, -4, -7$ and -8. The resistance value at the different minima increases as the temperature increases. Eventually for a high enough temperature, the resistance minima due to the splitting of the LLs vanish.

The physical mechanism behind the increase in resistance can be explained as follows: charge carriers are excited due to the temperature from localized states in between two Landau levels to the closest extended state. The carriers contribute therefore to the electrical conduction leading to an increase of the sample conductivity σ_{xx}. Using the relations 2.16, we see that for a quantum Hall state ($\sigma_{xy} >> \sigma_{xx}$ and is constant) $\rho_{xx} \propto \sigma_{xx}$. Thus, an increase in the longitudinal conductivity due to the thermal activation of carriers is reflected by an increase in the longitudinal resistivity.

The temperature dependence of R_{xx} can be modelled using the Fermi-Dirac distribution

$$R_{xx} \propto \frac{1}{1 + e^{\Delta/2k_BT}} \tag{2.28}$$

where Δ is the distance in energy between the extended state region in two consecutive LLs (see Figure 2.6), k_B is the Boltzmann constant and T is the temperature. This description holds if one assumes that the thermal activation occurs between Dirac-δ-like states.

In order to extract the gap size Δ_ν, we plot the value of R_{xx} for a minimum as a function of the temperature and perform a fit to the data according to eq.2.28. As an example of a typical fit for one of the filling factors resulting form the LL degeneracy lifting, we show in Figure 2.8 (b) the value of the resistance minima corresponding to $\nu = -1$ at 17.5 T (symbols) and the fit according (black solid line).

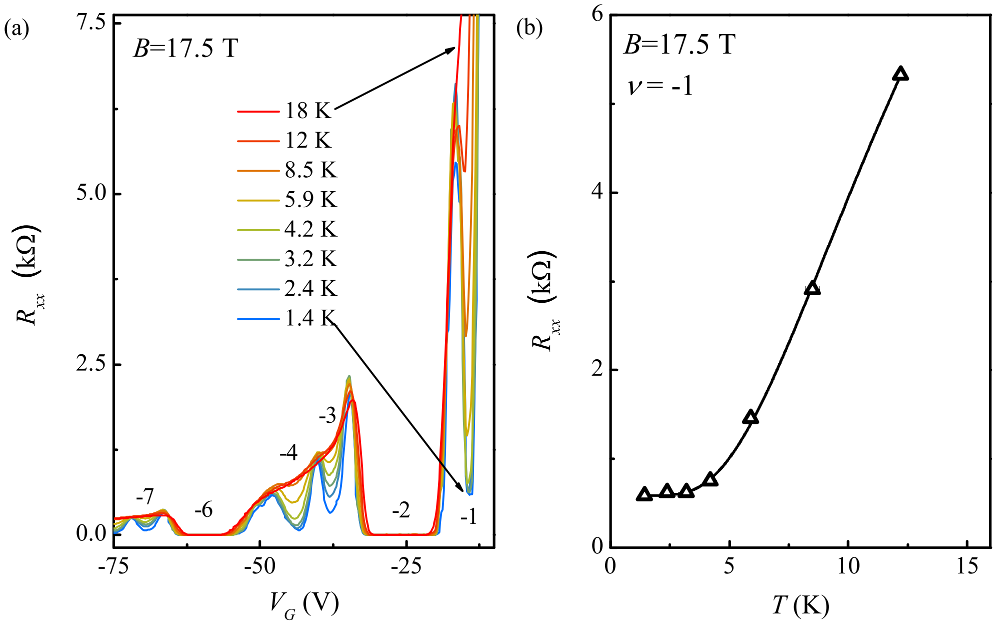

Figure 2.8: *Thermally activated transport. (a): Temperature dependent magnetotransport.* R_{xx} *as a function of* V_G *at* $B = 17.5$ T *for different temperatures. The number close to the minima of* $R_x x$ *indicate the filling factor. (b):* R_{xx} *minima for* $\nu = \pm 1$*(symbols) as a function of temperature at 17.5 T. The solid line is the fit to the experimental data according to eq.2.28.*

2.4 Capacitance spectroscopy

The electronic properties of graphene and, in particular, its *DOS* can be addressed directly by means of capacitance spectroscopy. Capacitance spectroscopy is an experimental technique widely used in the study of the electronic properties of two dimensional electron gases[41–46] as it provides a direct access to the density of states of the system[47] by measuring the capacitance between the electron gas and a gate electrode.

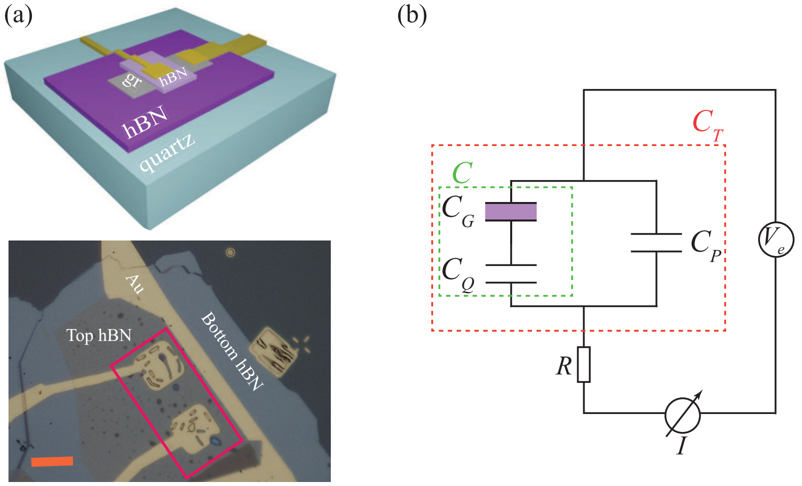

Figure 2.9: *Graphene based capacitors. (a): Device description. Top panel: general structure of the devices under investigation. The graphene (the gray stripe) is placed between two layer of hBN (purple layers) on top of a quartz substrate (light blue volume). The Ti/Au electrode (gold area) is placed on top of the topmost hBN layer. Bottom panel: optical picture of one sample presenting 2 different plates (inside the red box) on the same graphene flake. The orange bar corresponds to 15 μm. (b) Electrical circuit equivalent to the devices depicted in panel (a).*

The devices studied in the experiments are graphene based capacitors. The general structure of such devices can be seen in the top panel of figure 2.9 (a). A large quartz substrate (light blue in the figure) supports an heterostructure of graphene and hBN prepared using a dry transfer technique.[48] The graphene, depicted as the gray area, is sandwiched between two thin layers of hBN (the two purple areas). The graphene is connected to a Ti/Au contact and on top of the upper hBN layer is evaporated a wide Ti/Au electrode.

The bottom panel of figure 2.9 (a) is an optical picture of two devices on the same chip. It is possible to identify the two gold electrodes on top of the hBN layer (surrounded by the red box in the picture). The design of the electrodes is specific to each sample and is made such to avoid bubbles visible at the hBN surface. The formation of the bubbles takes place during the stacking process when some residuals of the chemicals involved in the fabrication remain trapped between adjacent layers of graphene and hBN.[49] The other contact visible in the picture is directly connected to the graphene (invisible in such a picture). It is worth noting that, since hBN is an insulator, there is no direct electrical connection between the gold plate on top of the hBN layer and the graphene. Therefore, this system can be regarded as a parallel plate capacitor where the two plates (the graphene layer and the Au electrode) are spatially separated by a dielectric (the thin hBN layer, brown area in the optical picture).

Typically, for the samples used in this study, the thickness of the hBN layer between the graphene and the gold electrode varies between 25 and 45 nm and the surface area of the electrode ranges between 185 and 340 μm^2.

The capacitance of the system is measured applying an ac excitation voltage V_e (20-30 mV) across the device and reading the current I which flows through the capacitor. The system can be modelled in first approximation as a circuit made of a capacitor with capacitance C_T and a resistor R, as depicted in Figure 2.9 (b). Ignoring the inductive contribution to the signal, the impedance of the system Z can be expressed in terms of two components

$$Z = R + \frac{1}{j\omega C_T} \tag{2.29}$$

where R and C_T are the the resistance and the capacitance of the system, respectively, $\omega = 2\pi f$ and f is the frequency of the ac voltage signal. R incorporates all the resistive contributions due to the experimental setup (e.g. cables, wiring, contact resistance), as well as the resistance of the graphene sheet. The total capacitance of the system C_T is determined by several contribution which are described in section 2.4.1.

The current flowing through the device is given by Ohm's law

$$I = \frac{V_e}{Z} \tag{2.30}$$

and therefore, we obtain the real and imaginary components of I

$$\mathrm{Re}(I) = V_e \frac{\omega^2 R C_T^2}{1+\omega^2 R^2 C_T^2} \tag{2.31}$$

$$\mathrm{Im}(I) = V_e \frac{\omega C_T}{1+\omega^2 R^2 C_T^2}, \tag{2.32}$$

respectively. For $1/(RC_T) >> \omega$ we find

$$\mathrm{Re}(I) \approx V_e R \omega^2 C_T^2 \tag{2.33}$$

$$\mathrm{Im}(I) \approx V_e \omega C_T. \tag{2.34}$$

In an experiment, the component of I at 90° degree phase with respect to V_e ($\mathrm{Im}(I)$) gives C_T. The component of the current in phase with respect to the external excitation ($\mathrm{Re}(I)$) is related to the dissipation in the system and is referred to as *Loss* and given by

$$\mathit{Loss} = \mathrm{Re}(I)/(\omega V_e). \tag{2.35}$$

The ac voltage V_e is superimposed to a larger dc bias voltage (V_G) applied across the capacitor plates in order to tune the charge carrier concentration of the graphene.

The capacitance of the devices is measured either by a capacitance bridge (AH2700) or by a current amplifier (Keithley 428) connected to a lock-in.

2.4.1 Electrostatics of the devices

The measured capacitance can be modelled in first approximation as a system of ideal capacitors C and C_P connected in parallel, as depicted in figure 2.9 (b). C is the capacitance of the device, while C_P is referred to as parasitic capacitance. The capacitance C of the devices can be described as the system of two different capacitors acting in series[47]

$$\frac{1}{C} = \frac{1}{C_G} + \frac{1}{C_Q} \tag{2.36}$$

where $C_G = \epsilon_0 \epsilon_{BN} S/d$ is the geometrical capacitance of the parallel plate capacitor having a plate area S, and a hBN spacer of thickness d and dielectric constant ϵ_{BN}.

The so-called quantum capacitance, C_Q, is the quantity that we want to access in the measurements. It is directly proportional to the density of states of the system[42] through the area S of the device and the electron charge e

$$C_Q = S e^2 \frac{dn}{d\mu} \tag{2.37}$$

where n is the charge carrier density, μ is the chemical potential and the ratio $\frac{dn}{d\mu}$ is the DOS.
The parasitic capacitance C_P includes all the spurious contributions to the signal due to the experimental set-up (e.g. cable, wiring of the sample, etc.).
Therefore, the total measured capacitance is given by:

$$C_T = C + C_P. \tag{2.38}$$

In contrast to graphene FETs discussed in section 2.2, the relationship between V_G and the induced carrier density n is not linear. Indeed, the effect of an increase in n on the system is twofold: it induces a potential drop ϕ due to C_G and a shift in the chemical potential of the system μ. In case of graphene, the chemical potential is directly proportional to the square root of n (see eq.2.7). Therefore, one finds

$$eV_G = e\phi + \mu = en\frac{d}{\epsilon_0\epsilon_{BN}} + \hbar v_F\sqrt{\pi n}\ . \tag{2.39}$$

With the typical parameters of the devices $n = 1 \times 10^{16}\,\mathrm{m}^{-2}$, $d = 30\,\mathrm{nm}$ and $\epsilon_{BN} = 2.42$ (for this last values see Appendix A), one finds that the two terms on the right side of eq.2.39 are within the same order of magnitude and neither of them can be neglected.[23,46] This is not the case for the conventional FETs having a Si/SiO$_2$ back gate with $d = 280\,\mathrm{nm}$. In these devices, the electrostatic voltage drop ϕ dominates the right term of eq.2.39 and the charge carrier concentration induced in the devices is considered to depend linearly on the gate voltage, as described by eq.2.10.

2.4.2 Experimental data

Typical results of a capacitance measurement for graphene based devices are reported in Figures 2.10 and 2.11, the latter in the presence of a an external magnetic field. In both figures, we can see that C_T strongly varies as a function of V_G. The dependence of C_T on V_G is due to C_Q, since C_G and C_P do not depend on the external bias.
At $B = 0$ (figure 2.10), the signal is characterized by a sharp minimum at low V_G. The specific behaviour of C_T can be understood qualitatively as follows. When the chemical potential is located at the Dirac point (the density of states has a minimum and ideally approaches zero, see Figure 2.2), C_Q dominates the value of C_T. On the other hand, when μ lies in the valence or in the conduction band and many states are populated, the contribution of C_Q vanishes and C_T approaches the saturation value $C_T = C_G + C_P$. In zero magnetic field the *Loss*

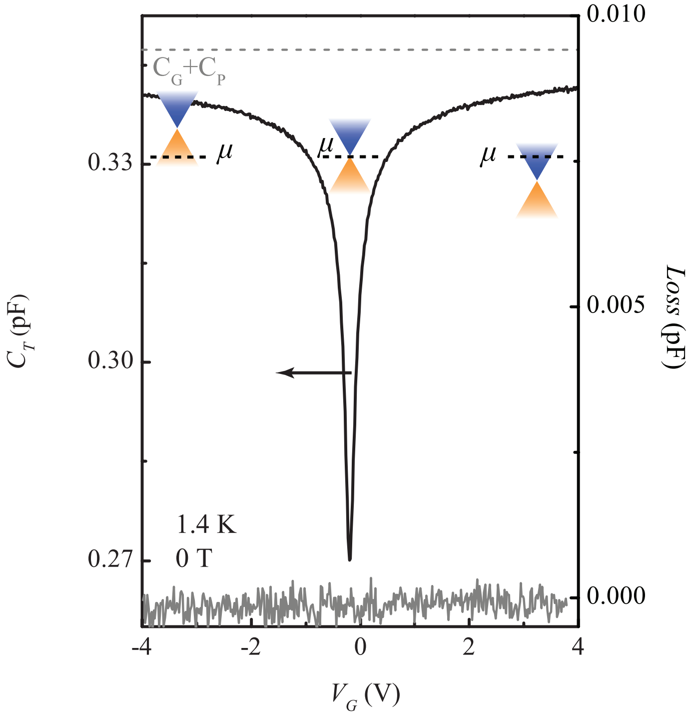

Figure 2.10: *Total capacitance and Loss (right axis) in zero magnetic field as a function of the gate voltage. The total capacitance was measured by the capacitance bridge AH2700 with $V_e = 30\,mV$ at 20 kHz.*

signal is zero within the noise level (i.e. $\omega RC_T << 1$, see equations 2.33 and 2.34) and does not show any dependence on V_G.

In a perpendicular magnetic field, the *DOS* consists of non-equidistant Landau levels, as explained in section 2.3. The quantization of the *DOS* can be probed through the measure of C_T. In Figure 2.11, we plot C_T and *Loss* at 1.4 K for $B = 2.5\,\mathrm{T}$ (left panel) and $B = 5\,\mathrm{T}$ (right panel). We observe several peaks characterized by an increasing depth as V_G approaches the CNP. The CNP, indicated by the vertical dashed line in figure 2.11, separates the four fold degenerate Landau levels for electrons (on right side of the NP) from those for holes (on the left side). From equations 2.36 and 2.37, one can see that minima in the capacitance signal correspond to minima of the DOS and, therefore, each of them can be associated to an integer filling factor ν (see the labelling of the top axis). As the Landau level index increases, the energy separation between two consecutive levels decreases leading to an overlap of the broadened levels.

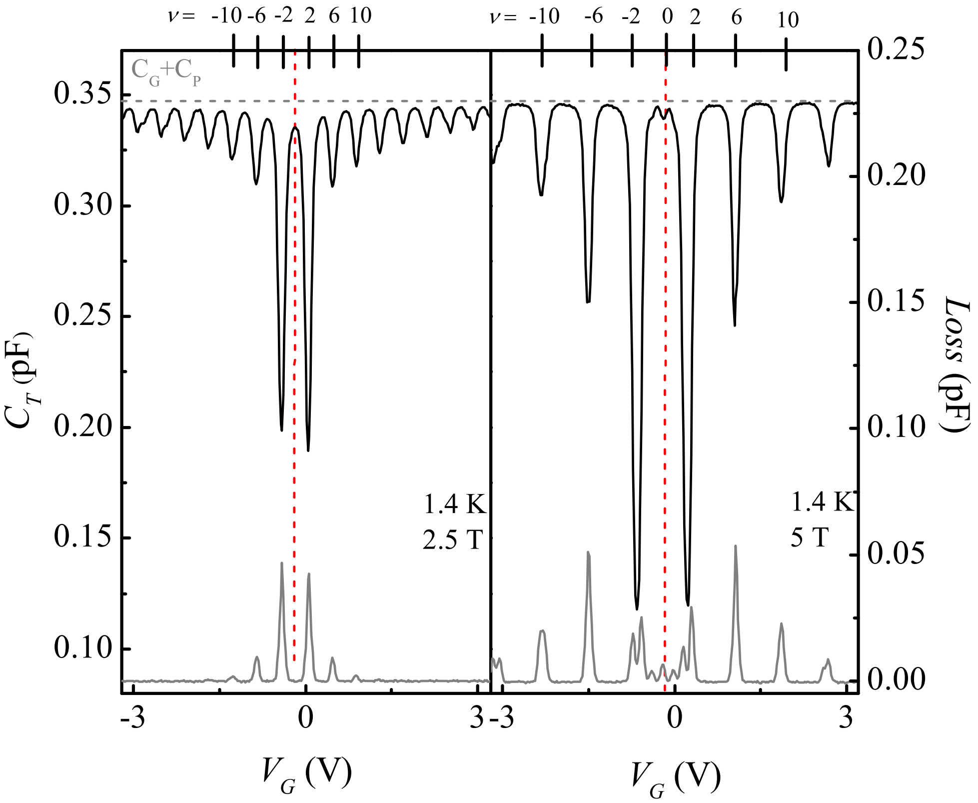

Figure 2.11: *Total capacitance as a function of* V_G *at 1.4 K in a perpendicular magnetic field of* 2.5 *T (left) and* 5 *T (right). The horizontal dashed line represents the value* $C_G + C_P = 0.347$ *pF. At high filling factors it is possible to observe a double peak structure probably due to the presence of a density gradient in the graphene. On the top axis we indicate as an example the filling factors for* $|\nu| =\leq 10$. *It is worth noting that at* 5 *T we observe already the incipient splitting of the lowest energy level with a clear minimum in* C_T *for* $\nu = 0$ *and three distinct peaks in the Loss signal.*

An overlap of different levels leads to an increase of the *DOS* for a certain energy value, which is reflected by a shallower minimum in C_T.

At $B = 2.5\,\mathrm{T}$, the *Loss* signal presents several sharp peaks in correspondence of the deepest minima of C_T ($|\nu| \leq 10$). Equations 2.33 and 2.35 show that an increase in *Loss* is related to an increase in R. As reported in section 2.4, R is given by the resistive components of the experimental setup and by the resistance of the graphene itself. Whereas we do not expect any abrupt change in the resistance of the cables and the contacts of the device due to the external magnetic field, the graphene becomes highly resistive when the chemical potential is within localized states that populate the region in between two LLs (see Figure 2.6). This suggests that the steep rise observed in *Loss* at $\nu = \pm 2, \pm 6$ and ± 10 is due to the highly resistive bulk of the graphene occurring at integer filling factors.

Between consecutive ν, when μ crosses a highly populated Landau level, the capacitance value approaches the value $C_G + C_P$. This can be clearly seen at an higher field of 5 T (right panel of figure 2.11), where in between the sharp minima, C_T flattens around the value $C_G + C_P = 0.347\,\mathrm{pF}$ (for more details on the calculation of this value refer to Chapter 4 and Appendix A). In these regions, the resistance of the graphene is finite and comparable in order of magnitude with the value at $B = 0$ (see Figures 2.3 (c) and 2.7), as a consequence, the *Loss* value is small.

Comparing the two panels of Figure 2.7, we see that the *Loss* signal is also affected by an increased magnetic field. At 5 T, new peaks are visible also for $|\nu| > 10$ and the features at $\nu = \pm 6$ and ± 10 are enhanced with respect to the ones at 2.5 T, compatibly with an increase in the resistance of the graphene due to the higher magnetic field. The *Loss* features associated to the strongest $\nu \pm 2$ evolve into a double peak structure.

The dependence of the *Loss* on the magnetic field is illustrated in Figure 2.12 where we plot, as an example, the *Loss* signal for $\nu = 1$ for several magnetic fields. The peak height strongly increases between 5 and 10 T and subsequently decreases as the field reaches 15 T. Eventually, for higher fields (20 and 25 T), it evolves into a double-peaked structure. Such a behaviour is common to all filling factors and it is associated to the increasingly resistive bulk of graphene.[43]

2.4.3 Insulating bulk in capacitance measurements

Up to this point, we have assumed that $1/(RC_T) >> \omega$ and that, by measuring the out-of-phase component of the current flowing through the device, we access the capacitance of the system and eventually its *DOS* (see eq.2.37). A minimum in the capacitance traces can be interpreted as a minimum in the

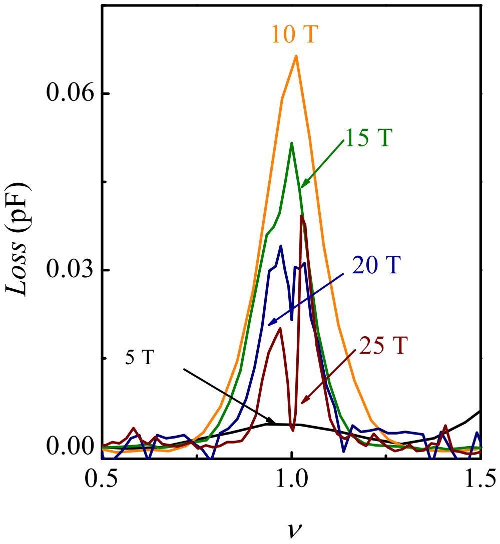

Figure 2.12: *Evolution of the Loss with the external magnetic ($B = 5, 10, 15, 20$ and 25 T) field at filling factor $\nu = 1$ at $1.4\,K$.*

DOS. However, when the chemical potential is within the localized states in the *DOS*, R strongly increases leading to $1/(RC_T) \gtrapprox \omega$. In this case, one has to use eq.2.31 and 2.32 in order to describe the current flowing to through the sample, rather than the approximated formulas 2.34 and 2.33. Indeed, the exact expression of the *Loss* (equations 2.31 and 2.35) can explain the double-peaked structure (see Figure 2.12) observed for all ν at high magnetic fields.

But if the value of R increases with the magnetic field such that the condition $1/(RC_T) < \omega$ is reached, the capacitor is only partially charged by the external excitation. In this case, the values obtained for C_T are not reliable and cannot be used to calculate the *DOS* of the system. The partial charging of the device can be described in terms of a diminution of the effective area of the capacitor plates. This changes the geometrical capacitance of the device C_G which becomes unknown and therefore, eq.2.37 can no longer be used to obtain the *DOS* of the graphene.

Thus, the presence of a non zero *Loss* indicates that the resistance of the graphene becomes significant and that the conversion of the data into *DOS* should be applied carefully (using eq. 2.31 instead of eq.2.34) or it should not be preformed at all.

In Chapter 3 we present capacitance data obtained in a high magnetic field when most of the states at integer ν are strongly insulting. We cannot derive any quantitative information about the *DOS* but we present the data as a qualitative support to the complementary transport traces. In Chapter 4, we address the splitting of the lowest Landau level in a low perpendicular magnetic field. We derive and empirical criterion over the magnitude of the *Loss* in order to decide when the relation 2.37 is applicable in our experiments and we convert the capacitance data into *DOS*.

2.5 Graphene on hexagonal boron nitride

In the previous sections we described the graphene based FETs and capacitors used in our experiments. In both kind of devices, the graphene is sandwiched between two flakes of hBN. In this section we motivate the use of hBN as a high quality substrate which allows us to probe the intrinsic properties of graphene. Since discovery of graphene, many efforts have been devoted to increasing the electronic quality of graphene based devices. The first graphene devices were ambipolar FETs employing a wafer of Si/SiO_2 as a substrate.[1] In such devices mobility values up to $2 \times 10^4\,\mathrm{cm^{-2}V^{-1}s^{-1}}$ were achieved[19] showing a weak dependence on temperature.[17]
It was inferred that, due to the low rate of electron-phonon scattering in graphene, the intrinsic mobility of charge carriers in graphene at room temperature could exceed $2 \times 10^5\,\mathrm{cm^{-2}V^{-1}s^{-1}}$, surpassing the intrinsic mobility of any other semiconductor[50,51] . The cause of the lower mobility value reported experimentally[17] has to be found in extrinsic mechanisms such as the presence of ripples, the scattering of with surface phonons of the substrate or the presence of charge impurities[52] trapped between the graphene and the SiO_2.
Several STM studies revealed that graphene conforms to the underlying substrate[53,54] and that SiO_2 induces very high corrugations[55,56] thus representing a limiting factor for the mobility of charge carriers. In order to overcome these problems, two approaches have been employed.
The first approach consists in completely removing the substrate and fabricate suspended devices.[57] Despite the high electronic quality achieved in such devices, which lead to the observation of, among others, ballistic transport,[58] the fraction quantum Hall effect[27] and the renormalization of the energy spectrum due to interactions,[59] suspended device are intrinsically fragile and impose severe limitations to the geometry of the sample.
In 2010 Dean *et al.*[8] have shown that the wide band insulator boron nitride in the hexagonal crystal structure represents the ideal substrate for graphene. hBN is a layered material isomorph to graphene. Referring to the crystal structure in Figure2.1 (a), the two distinct elements of hBN occupy the two distinct sites

A and B. The mismatch between hBN and graphene lattice constants is 1.8%. hBN can be exfoliated[60] in a similar way to graphene and reduced to few atomic layer thick flakes. The surface of hBN does not present dangling bonds and the flakes resulting from the exfoliation process are atomically flat.

In their work, Dean and collaborators proved that it is possible to fabricate FETs having graphene deposited on top of hBN with improved mobility and carrier homogeneity with respect to SiO_2 supported devices. The fabrication process of such devices involves the exfoliation of the different crystals and the subsequent stacking of the atomic layers. Successive developments in the fabrication technique and in particular the so called try transfer method[61] have lead to the observation of mobility values higher than $1 \times 10^5\,\mathrm{cm^{-2}V^{-1}s^{-1}}$ at room temperature.[48]

A further improvement of the device quality is provided by the encapsulation of graphene between two layers of hBN. Graphene tends to react with the atmosphere and the bonding to other molecules results in undesired doping and degradation of the electronic properties.[62] A capping hBN layer prevents the graphene from being contaminated by the ambient atmosphere therefore enabling the production of more stable devices.

Nowadays, the production of heterostructures based on graphene is routinely achieved in several research laboratories, and graphene is placed side by side not only to hBN but to a big variety of different 2D materials (e.g. chalcogenides, oxides). The electronic properties of this new class of artificial materials, which fall under the name of van der Waals heterostructures, can be tailored depending on the chemical composition and the thickness of the layers.[63] In case of hBN-based heterostuctures, the effect on the electronic properties of graphene is twofold. In addition to the role of high quality substrate already mentioned, the relative orientation of the two lattices might result into the breaking of the sublattice symmetry of the graphene[64] and into the formation of Moiré patterns.[54,65] Depending on the degree of alignment of the two lattices,[66] the spectrum of graphene changes dramatically developing a band gap and Moiré minibands.[67–69]

In our case, we consider encapsulated graphene with a random orientation with respect to the surrounding hBN layers such that no modifications to the dispersion of graphene are expected. Therefore, we are able to access the electronic properties of high quality graphene by means of transport and capacitance measurements.

2.6 Tilted fields experiments

The measurements in a tilted magnetic field are the central core of this work. We performed both transport and capacitance experiments in a tilted magnetic field in order to address the nature of the ground states resulting from the splitting of the Landau levels.

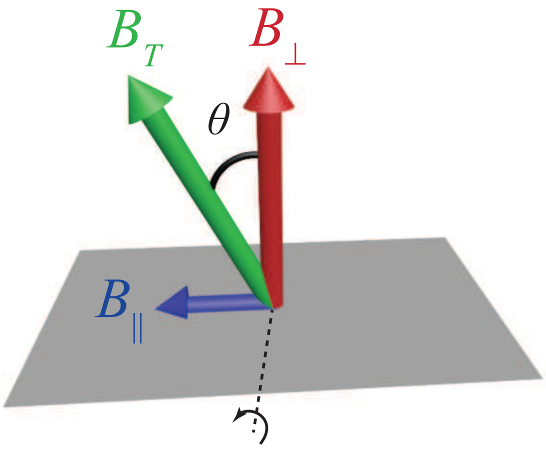

Figure 2.13: *Tilting configuration and definition of the angle θ. The conductive graphene plane is depicted as the gray area. θ is the angle formed by the external magnetic field B_T (green arrow) and the normal to the graphene plane. The red and the blue arrows represents the components perpendicular and parallel to the graphene plane, respectively.*

The tilt angle configuration is depicted in figure 2.13. The gray plane represents the graphene plane and the green arrow labelled as B_T indicates the external magnetic field. The samples are placed on a custom made sample holder that allows rotation around one axis. We define θ as the angle between the direction of the magnetic field and the normal to the graphene plane. The magnetic field can be decomposed into two separate components one perpendicular to the graphene plane

$$B_\perp = B_T \cos\theta \tag{2.40}$$

and one parallel

$$B_\parallel = B_T \sin\theta \ . \tag{2.41}$$

Tilted fields experiments have been vastly employed to study the physics of 2D systems following the seminal work of Fang and Stiles.[70]

The concept exploited in a tilted field experiment is that, for a 2D system, different energy scales depend on the different component of the magnetic field. In particular, considering the energy scales relevant to the LL splitting mentioned in the previous sections, we see that the cyclotron, the Coulomb and the anisotropy energies (eqs. 2.18, 2.25 and 2.26) are sensitive only to $B_\perp$, as they are related to the orbital motion of the carriers. By contrast, the Zeeman effect (eq.2.24) depends on the total magnetic field applied on the system, regardless to its orientation. Table 2.1 summarizes the different energy scales and their dependence of the external magnetic field.

Table 2.1: *Different energy scales for graphene in an external magnetic field. E_N is the cyclotron energy, E_C the Coulomb energy, E_{LS} is the energy related to the lattice scale anisotropies and E_Z is the Zeeman energy.*

Energy	Dependence
E_N	$\propto \sqrt{B_\perp}$
E_C	$\propto \sqrt{B_\perp}$
E_{LS}	$\propto B_\perp$
E_Z	$\propto B_T$

Tilting the sample, corresponds therefore to tuning the different energy scales and change their relative strengths. As an example, in Chapters 3 and 4 we bring to light the spin polarization of the symmetry broken states by tilting the sample while keeping $B_\perp$ constant. By measuring the dependence of the resistance and of the capacitance of the sample as a function of the tilt angle, one can decouple the effects related to the orbital motion of the electrons (therefore dependent on $B_\perp$) from those related to the spin (sensitive to B_T).

However, it has to be stressed that, such a simple picture of decoupling the spin and the orbital effects by tilting the sample with respect to the direction of the external magnetic field, does not apply generally. Indeed, we implicitly made two assumptions that, as we shall see, are justified in the case of graphene but do not hold in general.

First, we assumed that the orbital motion of carriers is affected only by $B_\perp$. This is the case only for a truly 2D system, for which the motion of carriers is strictly confined in a plane. In case the system presents a finite width, the tilted external magnetic field can couple to the out-of-plane motion of the carriers and thus, influence their energy spectrum. The calculation of the energy spectrum for an arbitrary angle between the magnetic field direction and the electron gas plane is a complex problem that depends on the specific shape of the confinement potential. For a conventional 2D system with multiple sub-bands, it can be solved analytically in case of a parabolic confinement potential.[71] The formation of the Landau levels and their degeneracy are determined by $B_\perp$ but the energy spacing in between them depends on B_T. Similarly, B_T affects the strength of the electron-electron interactions.

More rigorously, a truly 2D system is defined as a confined system characterized by a quantized energy spectrum with only one sub-band occupied. Therefore, the energy separation between sub-bands has to be larger than any other energy scale of the system. For graphene, the electrons are confined within the carbon atom plane and the energy separation between π bands and σ bands at the Dirac points is in the order of $10\,\mathrm{eV}$.[6] For realistic experimental conditions, this value is much lager than the spacing between the Landau levels $N = 1$ and $N = 0$ ($E_1 - E_0 \approx 0.20\,\mathrm{eV}$ for $B = 30\,\mathrm{T}$), the Fermi energy ($E_F \approx 0.2\,\mathrm{eV}$ for $n \approx 3 \cdot 10^{12}\,\mathrm{cm}^{-2}$) and the thermal energy ($k_B T \approx 0.0003\,\mathrm{eV}$ at $4.2\,\mathrm{K}$). Therefore, graphene is a truly 2D system and we can assume that the motion of the carriers is only affected by $B_\perp$.

In addition, the tilted fields experiments implicitly assume that the spin and the motion of the carriers can be treated separately and do not influence each other. However, in many systems, they are intricately connected through the spin-orbit coupling. Such a coupling is a relativistic effect that can be understood intuitively as follows: when one electron moves around the nucleus of an atom, it experiences, in its own rest system, not only the electric field generated by the nucleus, but also a magnetic field. This magnetic field affects the spin of the electron via the Zeeman effect. Formally, the spin-orbit coupling is described by the Hamiltonian[72]

$$\hat{H}_{SO} = \frac{\hbar}{4m^2c^2}(\boldsymbol{\nabla} V \times \boldsymbol{q}) \cdot \boldsymbol{\sigma} \sim \boldsymbol{L} \cdot \boldsymbol{\sigma} \tag{2.42}$$

where m is the electron mass, V is the nuclear potential, $\boldsymbol{q}$ is the quasiparticle momentum, $\boldsymbol{\sigma}$ are the Pauli matrices describing the spin of the system and $\boldsymbol{L}$ is the angular momentum operator.

The spin-orbit interaction modifies the band structure of many semiconducting materials lifting the degeneracy of energy bands at high symmetry points of the first Brillouin zone. For example, the energy separation between the split-off band and the degenerate light and heavy hole bands at the Γ point in Si and Ge is $44\,\mathrm{meV}$ and $290\,\mathrm{meV}$, respectively.[10]

Equation 2.42 shows that the spin-orbit coupling depends on the nuclear potential as well as on the symmetry of the bands occupied by the carriers. Because of the small atomic number of the C atoms and the orientation of the π orbitals of graphene, the energy gap due to the spin-orbit coupling at the Dirac point is very small ($10^{-3}\,\mathrm{meV} \approx 10\,\mathrm{mK}$).[72–75] Therefore, the effects of the spin-orbit coupling on the electronic properties of graphene are regarded as negligible.[6]

Thus, since graphene is a truly 2D system with a negligible spin-orbit coupling, the use of tilted fields as a way to decouple spin and orbital effects is fully justified and experiments in tilted fields have already been proven to be a powerful tool in order to address the spin polarization of electronic states in a magnetic field.[18,19,22,76]

The special case $\theta = 90°$ is dissimilar from all the other cases. In this configuration the magnetic field is parallel to the confinement plane ($B_T = B_{\|}$) and $B_{\perp} = 0$. The fundamental difference between the $\theta = 90°$ angle and any other angle configuration is that the Landau levels are not formed. The field affects the 2D electron gas via the Zeeman effect and, in case the system presents a finite width, it modifies the energy of the different sub-bands and the density of state.[71] In Chapter 5, we employ transport experiments in a parallel magnetic field in order to address the effect of the Zeeman splitting of the DOS on the transport properties of graphene.

References

[1] K. Novoselov, A. Geim, S. Morozov, D. Jiang, Y. Zhang, S. Dubonos, I. Grigorieva, and A. Firsov, "Electric Field Effect in Atomically Thin Carbon Films", *Science* **306**, 5696, 666 (2004).

[2] P. R. Wallace, "The band theory of graphite", *Physical Review* **71**, 9, 622–634 (1947).

[3] A. K. Geim and K. Novoselov, "The rise of graphene", *Nature Materials* **6**, 3, 183–191 (2007).

[4] A. H. Castro Neto, F. Guinea, N. M. R. Peres, K. S. Novoselov, and A. K. Geim, "The electronic properties of graphene", *Reviews of Modern Physics* **81**, 1, 109–162 (2009).

[5] M. O. Goerbig, "Electronic properties of graphene in a strong magnetic field", *Reviews of Modern Physics* **83**, 4, 1193–1243 (2011).

[6] M. I. Katsnelson, "Graphene: Carbon in Two-Dimensions", *Cambridge University Press* (2012).

[7] M. I. Katsnelson, K. S. Novoselov, and A. K. Geim, "Chiral tunnelling and the Klein paradox in graphene", *Nature Physics* **2**, 9, 1986 (2006).

[8] C. R. Dean, a. F. Young, I. Meric, C. Lee, L. Wang, S. Sorgenfrei, K. Watanabe, T. Taniguchi, P. Kim, K. L. Shepard, and J. Hone, "Boron nitride substrates for high-quality graphene electronics", *Nature Nanotechnology* **5**, 10, 722–726 (2010).

[9] F. Schedin, A. Geim, S. Morozov, E. Hill, P. Blake, M. Katsnelson, and K. Novoselov, "Detection of individual gas molecules adsorbed on graphene", *Nature Materials* **6**, 9, 652–655 (2007).

[10] T. Ihn, "Semiconductor Nanostructures", *Oxford University Press* (2010).

[11] J. W. McClure, "Diamagnetism of graphite", *Physical Review* **104**, 3, 666 (1956).

[12] K. Von Klitzing, "The quantized Hall effect", *Reviews of Modern Physics* **58**, 3, 519–531 (1986).

[13] G. P. Mikitik and Y. V. Sharlai, "Manifestation of Berry's Phase in Metal Physics", *Physical Review Letters* **82**, 10, 2147–2150 (1999).

[14] V. P. Gusynin and S. G. Sharapov, "Magnetic oscillations in planar systems with the Dirac-like spectrum of quasiparticle excitations. II. Transport properties", *Physical Review B* **71**, 12, 125124 (2005).

[15] Y. Zhang, Y.-W. Tan, H. L. Stormer, and P. Kim, "Experimental observation of the quantum Hall effect and Berry's phase in graphene", *Nature* **438**, 7065, 201–204 (2005).

[16] K. S. Novoselov, A. K. Geim, S. V. Morozov, D. Jiang, M. I. Katsnelson, I. V. Grigorieva, S. V. Dubonos, and A. A. Firsov, "Two-dimensional gas of massless Dirac fermions in graphene", *Nature* **438**, 7065, 197–200 (2005).

[17] K. S. Novoselov, Z. Jiang, Y. Zhang, S. V. Morozov, H. L. Stormer, U. Zeitler, J. C. Maan, G. S. Boebinger, P. Kim, and A. K. Geim, "Room-temperature quantum Hall effect in graphene.", *Science* **315**, 5817, 1379 (2007).

[18] Y. Zhang, Z. Jiang, J. P. Small, M. S. Purewal, Y. W. Tan, M. Fazlollahi, J. D. Chudow, J. A. Jaszczak, H. L. Stormer, and P. Kim, "Landau-level splitting in graphene in high magnetic fields", *Physical Review Letters* **96**, 13, 136806 (2006).

[19] Z. Jiang, Y. Zhang, H. L. Stormer, and P. Kim, "Quantum hall states near the charge-neutral dirac point in graphene", *Physical Review Letters* **99**, 10, 106802 (2007).

[20] A. J. M. Giesbers, L. A. Ponomarenko, K. S. Novoselov, A. K. Geim, M. I. Katsnelson, J. C. Maan, and U. Zeitler, "Gap opening in the zeroth Landau level of graphene", *Physical Review B* **80**, 20, 201403 (2009).

[21] J. G. Checkelsky, L. Li, and N. P. Ong, "Zero-energy state in graphene in a high magnetic field", *Physical Review Letters* **100**, 20, 206801 (2008).

[22] A. F. Young, C. R. Dean, L. Wang, H. Ren, P. Cadden-Zimansky, K. Watanabe, T. Taniguchi, J. Hone, K. L. Shepard, and P. Kim, "Spin and valley quantum Hall ferromagnetism in graphene", *Nature Physics* **8**, 7, 550–556 (2012).

[23] G. L. Yu, R. Jalil, B. Belle, A. S. Mayorov, P. Blake, F. Schedin, S. V. Morozov, L. a. Ponomarenko, F. Chiappini, S. Wiedmann, U. Zeitler, M. I. Katsnelson, a. K. Geim, K. S. Novoselov, and D. C. Elias, "Interaction phenomena in graphene seen through quantum capacitance.", *Proceedings of the National Academy of Sciences of the United States of America* **110**, 9, 3282–6 (2013).

[24] F. Chiappini, S. Wiedmann, K. Novoselov, A. Mishchenko, A. K. Geim, J. C. Maan, and U. Zeitler, “Lifting of the Landau level degeneracy in graphene devices in a tilted magnetic field”, *Physical Review B* **92**, 20, 201412 (2015).

[25] D. A. Abanin, B. E. Feldman, A. Yacoby, and B. I. Halperin, “Fractional and integer quantum Hall effects in the zeroth Landau level in graphene”, *Physical Review B* **88**, 11, 115407 (2013).

[26] F. Amet, J. R. Williams, K. Watanabe, T. Taniguchi, and D. Goldhaber-Gordon, “Selective equilibration of spin-polarized quantum hall edge states in graphene”, *Physical Review Letters* **112**, 19, 196601 (2014).

[27] X. Du, I. Skachko, F. Duerr, A. Luican, and E. Y. Andrei, “Fractional quantum Hall effect and insulating phase of Dirac electrons in graphene”, *Nature* **462**, 7270, 192–5 (2009).

[28] K. Nomura and A. H. MacDonald, “Quantum hall ferromagnetism in graphene”, *Physical Review Letters* **96**, 25, 256602 (2006).

[29] J. Alicea and M. P. A. Fisher, “Graphene integer quantum Hall effect in the ferromagnetic and paramagnetic regimes”, *Physical Review B* **74**, 7, 75422 (2006).

[30] K. Yang, S. Das Sarma, and A. H. MacDonald, “Collective modes and skyrmion excitations in graphene SU (4) quantum Hall ferromagnets”, *Physical Review B* **74**, 7, 75423 (2006).

[31] M. O. Goerbig, R. Moessner, and B. Douçot, “Electron interactions in graphene in a strong magnetic field”, *Physical Review B* **74**, 16, 161407 (2006).

[32] L. Sheng, D. N. Sheng, F. D. M. Haldane, and L. Balents, “Odd-integer quantum hall effect in graphene: Interaction and disorder effects”, *Physical Review Letters* **99**, 19, 196802 (2007).

[33] I. F. Herbut, “Theory of integer quantum Hall effect in graphene”, *Physical Review B* **75**, 16, 165411 (2007).

[34] K. Yang, “Spontaneous symmetry breaking and quantum Hall effect in graphene”, *Solid State Communications* **143**, 1-2, 27–32 (2007).

[35] W. Luo and R. Côté, “Zeeman coupling and screening corrections to skyrmion excitations in graphene”, *Physical Review B* **88**, 11, 115417 (2013).

[36] B. Roy, "Odd integer quantum Hall effect in graphene", *Physical Review B* **84**, 3, 35458 (2011).

[37] S. M. Girvin, "Aspects topologiques de la physique en basse dimension. Topological aspects of low dimensional systems", in *Arxiv preprint arXiv:* (A. Comtet, T. Jolicœur, S. Ouvry, and F. David, eds.)vol. 69 of *Les Houches - Ecole d'Ete de Physique Theorique*, 124Berlin, Heidelberg: Springer Berlin Heidelberg (1999).

[38] J. Alicea and M. P. A. Fisher, "Interplay between lattice-scale physics and the quantum Hall effect in graphene", *Solid State Communications* **143**, 11-12, 504–509 (2007).

[39] M. Kharitonov, "Phase diagram for the ν=0 quantum Hall state in monolayer graphene", *Physical Review B* **85**, 15, 155439 (2012).

[40] J. Jung and A. H. MacDonald, "Theory of the magnetic-field-induced insulator in neutral graphene sheets", *Physical Review B* **80**, 23, 235417 (2009).

[41] M. Kaplit and J. N. Zemel, "Capacitance observations of landau levels in surface quantization", *Physical Review Letters* **21**, 4, 212–215 (1968).

[42] T. Smith and B. Goldberg, "Direct measurement of the density of states of a two-dimensional electron gas", *Physical Review B* **32**, 4, 2696 (1985).

[43] R. K. Goodall, R. J. Higgins, and J. P. Harrang, "Capacitance measurements of a quantized two-dimensional electron gas in the regime of the quantum Hall effect", *Physical Review B* **31**, 10, 6597–6608 (1985).

[44] V. Mosser, D. Weiss, K. v. Klitzing, K. Ploog, and G. Weimann, "Density of states of GaAs-AlGaAs-heterostructures deduced from temperature dependent magnetocapacitance measurements", *Solid State Communications* **58**, 1, 5–7 (1986).

[45] T. P. Smith, W. I. Wang, and P. J. Stiles, "Two-dimensional density of states in the extreme quantum limit", *Physical Review B* **34**, 4, 2995–2998 (1986).

[46] L. A. Ponomarenko, R. Yang, R. V. Gorbachev, P. Blake, A. S. Mayorov, K. S. Novoselov, M. I. Katsnelson, and A. K. Geim, "Density of states and zero Landau level probed through capacitance of graphene", *Physical Review Letters* **105**, 13, 136801 (2010).

[47] S. Luryi, "Quantum capacitance devices", *Applied Physics Letters* **52**, 6, 501–503 (1988).

[48] A. S. Mayorov, R. V. Gorbachev, S. V. Morozov, L. Britnell, R. Jalil, L. A. Ponomarenko, P. Blake, K. S. Novoselov, K. Watanabe, T. Taniguchi, and A. K. Geim, "Micrometer-scale ballistic transport in encapsulated graphene at room temperature", *Nano Letters* **11**, 6, 2396–2399 (2011).

[49] S. J. Haigh, a. Gholinia, R. Jalil, S. Romani, L. Britnell, D. C. Elias, K. S. Novoselov, L. a. Ponomarenko, a. K. Geim, and R. Gorbachev, "Cross-sectional imaging of individual layers and buried interfaces of graphene-based heterostructures and superlattices", *Nature Materials* **11**, 9, 764–767 (2012).

[50] J.-H. Chen, C. Jang, S. Xiao, M. Ishigami, and M. S. Fuhrer, "Intrinsic and extrinsic performance limits of graphene devices on SiO2.", *Nature Nanotechnology* **3**, 4, 206–9 (2008).

[51] S. V. Morozov, K. S. Novoselov, M. I. Katsnelson, F. Schedin, D. C. Elias, J. A. Jaszczak, and A. K. Geim, "Giant intrinsic carrier mobilities in graphene and its bilayer", *Physical Review Letters* **100**, 1, 016602 (2008).

[52] E. H. Hwang, S. Adam, and S. D. Sarma, "Carrier transport in two-dimensional graphene layers", *Physical Review Letters* **98**, 18, 186806 (2007).

[53] C. H. Lui, L. Liu, K. F. Mak, G. W. Flynn, and T. F. Heinz, "Ultraflat graphene.", *Nature* **462**, 7271, 339–341 (2009).

[54] J. M. Xue, J. Sanchez-Yamagishi, D. Bulmash, P. Jacquod, a. Deshpande, K. Watanabe, T. Taniguchi, P. Jarillo-Herrero, and B. J. Leroy, "Scanning tunnelling microscopy and spectroscopy of ultra-flat graphene on hexagonal boron nitride", *Nature Materials* **10**, 4, 282–285 (2011).

[55] E. Stolyarova, K. T. Rim, S. Ryu, J. Maultzsch, P. Kim, L. E. Brus, T. F. Heinz, M. S. Hybertsen, and G. W. Flynn, "High-resolution scanning tunneling microscopy imaging of mesoscopic graphene sheets on an insulating surface.", *Proceedings of the National Academy of Sciences of the United States of America* **104**, 22, 9209–9212 (2007).

[56] M. Ishigami, J. H. Chen, W. G. Cullen, M. S. Fuhrer, and E. D. Williams, "Atomic structure of graphene on SiO 2", *Nano Letters* **7**, 6, 1643–1648 (2007).

[57] K. I. Bolotin, K. J. Sikes, Z. Jiang, M. Klima, G. Fudenberg, J. Hone, P. Kim, and H. L. Stormer, "Ultrahigh electron mobility in suspended graphene", *Solid State Communications* **146**, 9-10, 351–355 (2008).

[58] X. Du, I. Skachko, A. Barker, and E. Y. Andrei, "Approaching ballistic transport in suspended graphene.", *Nature Nanotechnology* **3**, 8, 491–5 (2008).

[59] D. C. Elias, R. V. Gorbachev, a. S. Mayorov, S. V. Morozov, a. a. Zhukov, P. Blake, L. a. Ponomarenko, I. V. Grigorieva, K. S. Novoselov, F. Guinea, and a. K. Geim, "Dirac cones reshaped by interaction effects in suspended graphene", *Nature Physics* **7**, 9, 701–704 (2011).

[60] K. S. Novoselov, D. Jiang, F. Schedin, T. J. Booth, V. V. Khotkevich, S. V. Morozov, and a. K. Geim, "Two-dimensional atomic crystals.", *Proceedings of the National Academy of Sciences of the United States of America* **102**, 30, 10451–10453 (2005).

[61] L. A. Ponomarenko, A. K. Geim, A. A. Zhukov, R. Jalil, S. V. Morozov, K. S. Novoselov, I. V. Grigorieva, E. H. Hill, V. Cheianov, V. Falko, K. Watanabe, T. Taniguchi, and R. V. Gorbachev, "Tunable metal-insulator transition in double-layer graphene heterostructures", *Nature Physics* **7**, 12, 958–961 (2011).

[62] J.-H. Chen, C. Jang, S. Adam, M. S. Fuhrer, E. D. Williams, and M. Ishigami, "Charged-impurity scattering in graphene", *Nature Physics* **4**, 5, 377–381 (2008).

[63] A. K. Geim and I. V. Grigorieva, "Van der Waals heterostructures.", *Nature* **499**, 7459, 419–25 (2013).

[64] G. Giovannetti, P. A. Khomyakov, G. Brocks, P. J. Kelly, and J. Van Den Brink, "Substrate-induced band gap in graphene on hexagonal boron nitride: Ab initio density functional calculations", *Physical Review B* **76**, 7, 073103 (2007).

[65] R. Decker, Y. Wang, V. W. Brar, W. Regan, H. Z. Tsai, Q. Wu, W. Gannett, A. Zettl, and M. F. Crommie, "Local electronic properties of graphene on a BN substrate via scanning tunneling microscopy", *Nano Letters* **11**, 6, 2291–2295 (2011).

[66] M. Yankowitz, J. Xue, D. Cormode, J. D. Sanchez-Yamagishi, K. Watanabe, T. Taniguchi, P. Jarillo-Herrero, P. Jacquod, and B. J. LeRoy, "Emer-

gence of superlattice Dirac points in graphene on hexagonal boron nitride", *Nature Physics* **8**, 5, 382–386 (2012).

[67] B. Hunt, D. Sanchez-Yamagishi, A. F. Young, M. Yankowitz, B. J. LeRoy, K. Watanabe, T. Taniguchi, P. Moon, M. Koshino, P. Jarillo-Herrero, and E. Ashoori, "Massive Dirac fermions and Hofstadter butterfly in a van der Waals heterostructure", *Science* **340**, 6139, 1427–1430 (2013).

[68] G. L. Yu, R. V. Gorbachev, J. S. Tu, a. V. Kretinin, Y. Cao, R. Jalil, F. Withers, L. a. Ponomarenko, B. a. Piot, M. Potemski, D. C. Elias, X. Chen, K. Watanabe, T. Taniguchi, I. V. Grigorieva, K. S. Novoselov, V. I. Fal'ko, a. K. Geim, and a. Mishchenko, "Hierarchy of Hofstadter states and replica quantum Hall ferromagnetism in graphene superlattices", *Nature Physics* **10**, 7, 525–529 (2014).

[69] C. R. Woods, L. Britnell, A. Eckmann, R. S. Ma, J. C. Lu, H. M. Guo, X. Lin, G. L. Yu, Y. Cao, R. V. Gorbachev, a. V. Kretinin, J. Park, L. a. Ponomarenko, M. I. Katsnelson, Y. N. Gornostyrev, K. Watanabe, T. Taniguchi, C. Casiraghi, H. J. Gao, A. K. Geim, and K. S. Novoselov, "Commensurate-incommensurate transition in graphene on hexagonal boron nitride", *Nature Physics* **10**, April, 1–6 (2014).

[70] F. F. Fang and P. J. Stiles, "Effects of a tilted magnetic field on a two-dimensional electron gas", *Physical Review* **174**, 3, 823–828 (1968).

[71] J. C. Maan, "Combined Electric and Magnetic Field Effects in Semiconductor Heterostructures", in *Two-Dimensional Systems, Heterostructures, and Superlattices*, 183–191,Springer Berlin Heidelberg (1984).

[72] Y. Yao, F. Ye, X.-L. Qi, S.-C. Zhang, and Z. Fang, "Spin-orbit gap of graphene: First-principles calculations", *Physical Review B* **75**, 4, 041401 (2007).

[73] D. Huertas-Hernando, F. Guinea, and A. Brataas, "Spin-orbit coupling in curved graphene, fullerenes, nanotubes, and nanotube caps", *Physical Review B* **74**, 15, 155426 (2006).

[74] A. H. Castro Neto and F. Guinea, "Impurity-induced spin-orbit coupling in graphene", *Physical Review Letters* **103**, 2, 026804 (2009).

[75] H. Min, J. E. Hill, N. A. Sinitsyn, B. R. Sahu, L. Kleinman, and A. H. MacDonald, "Intrinsic and Rashba spin-orbit interactions in graphene sheets", *Physical Review B* **74**, 16, 165310 (2006).

[76] E. V. Kurganova, H. J. Van Elferen, A. McCollam, L. A. Ponomarenko, K. S. Novoselov, A. Veligura, B. J. Van Wees, J. C. Maan, and U. Zeitler, “Spin splitting in graphene studied by means of tilted magnetic-field experiments”, *Physical Review B* **84**, 12, 121407 (2011).

CHAPTER 3

Splitting of the Landau levels of graphene in a tilted magnetic field

Abstract

In this Chapter we report on transport and capacitance experiments performed on graphene devices in magnetic fields up to 30 *T. In both techniques, we observe the full splitting of Landau levels and we employ tilted field experiments to address the origin of the observed broken symmetry states. In the lowest energy level, the spin degeneracy is removed at filling factors* $\nu = \pm 1$ *and we observe an enhanced energy gap. In the higher levels, the valley degeneracy is removed at odd filling factors while spin polarized states are formed at even* ν*. Although the observation of odd filling factors in the higher levels points towards the spontaneous origin of the splitting, we find that the main contribution to the gap at* $\nu = -4, -8$ *and* -12 *is due to the Zeeman energy.*

Part of this work has been published in: F. Chiappini, S. Wiedmann *et al.*, "Lifting of the Landau level degeneracy in graphene devices in a tilted magnetic field", Physical Review B **92**,201412 (R), (2015).

3.1 Introduction

One of the prominent consequences of the Dirac-like nature of charge carriers in graphene is the half-integer quantum Hall effect (see Section 2.3.2). The Hall conductance is quantized to half-integer multiples of $4e^2/h$, reflecting the spin and valley degeneracy of the Landau levels (LLs) at filling factors given by $\nu = 4(N + 1/2)$, where the index N has the values $0, \pm1, \pm2, \ldots$. Thus, the half-integer quantum Hall effect occurs at $\nu = \pm2, \pm6, \pm10$,...[1,2]

However, as described in section 2.3.3, electron-electron interactions and explicit symmetry breaking fields, such as the Zeeman splitting, can lift the LL degeneracy, leading to the observation of the quantum Hall effect at intermediate integer values of ν. The origin and the possible spin and/or valley polarization of the broken symmetry states has been the subject of considerable theoretical interest[3,4,4–9] and experimental investigations.[10–17]

Earlier experimental works on graphene on SiO_2 reported the partial splitting of $N = \pm1$ at $\nu = \pm4$[10,11,16] as a single particle effect due to the Zeeman energy, and the full splitting in the lowest LL driven by electron-electron interactions.[11] Experiments on cleaner devices deposited on hexagonal boron nitride (hBN) showed the full sequence of integer filling factors and addressed the role of electron-electron interactions in the LLs splitting,[15,18] revealing enhanced gaps in the higher LLs.[15] In the cases of $\nu = -4$ and $\nu = -8$, the gaps separate two states with opposite spin and the excitations of these states are found to be skyrmions.[15] Skyrmions are spatially ordered electron distributions that can be seen as charged quasiparticles characterized by a smoothly varying spin texture. Skyrmions can be formed in a quantum Hall system in presence of a strong exchange interaction[19–21] and, in graphene, they are predicted to be energetically favourable in the $|N| \leq 3$ LLs.[22] The observations of large energy gaps and skyrmion mediated transport reported by Young and collaborators[15] have been attributed to the quantum Hall ferromagnetism (QHF) in graphene[23] (see section 2.3.4).

In this Chapter we report on the LL splitting in graphene encapsulated between two layers of hBN and we investigate the nature of the states occurring at integer ν due to the lifting of the LL degeneracy. Thermally activated transport in both perpendicular and tilted magnetic fields up to 30 T, supported qualitatively by capacitance spectroscopy,[24] enables us to probe the origin of the states at $\nu = -1, -3, -4, -7, -8, -12$. We show that in the lowest LL, a spin unpolarized state is formed at $\nu = 0$ and the spin degeneracy is removed at $\nu = \pm1$. In the higher levels, the even ν separate two fully spin polarized states while the odd ν originate from the lifting of the valley degeneracy, supporting the findings of Ref. 15. We find that, for $|N| \geq 1$, the gap at half filling is set by the

Zeeman energy and we demonstrate that the interactions, although relevant in determining the splitting of the higher levels, are not the dominant energy scale for $|N| > 0$ in our devices.

3.2 Experimental details and sample characterization

We focus on two single layer graphene devices. In both devices the graphene flake is sandwiched between two hBN flakes. Device A is a Hall bar ($W \approx 1.3$ μm, $L/W = 2$) for standard magneto-transport measurements, as the one described in section 2.2. The longitudinal (R_{xx}) and Hall (R_{xy}) resistances are measured as a function of the back gate voltage (V_G) using a low noise lock-in technique with a 10 nA excitation current at 13 Hz. Measurements at the charge neutrality point (CNP) in a magnetic field are performed in a constant voltage configuration with a 100 μV excitation.

Device B is a graphene-hBN-Au capacitor, similar to the ones described in section 2.4, with a 45 nm thick hBN flake between the graphene and the Au electrode. The capacitance C_T is measured as a function of the DC voltage (V_G) applied between the top gate and the graphene sheet using a capacitance bridge (AH2700) with 30 mV AC excitation at 20 kHz. As described in section 2.4.1, C_T embodies three major contributions: the geometrical capacitance C_G, the quantum capacitance C_Q ,which is directly proportional to the density of states (DOS)[25] of graphene and the parasitic capacitance C_P. Both devices were placed in a variable temperature ^{4}He cryostat.

The transport and capacitance traces at 1.4 K and zero magnetic field are shown in Figures 2.3 (c) and 2.10 in the previous Chapter. As illustrated in Figures 2.3 (c) and 2.10, both samples are n-doped and the CNP is situated at $V_G^{CNP} \approx -10$ V for device A and $V_G^{CNP} \approx -0.2$ V for device B, corresponding to a residual electron concentration $n_A \approx 6 \times 10^{11}$ cm^{-2} and $n_B \approx 1 \times 10^{11}$ cm^{-2}, respectively. The field effect mobility of device A is $\mu_n = 4 \cdot 10^4$ cm^{2}V^{-1}s^{-1}. This value has been obtained performing a linear fit to the electrical conductivity as a function of the charge carrier density (see section 2.2 and Figure 2.4).

3.2.1 Perpendicular magnetic field

In a perpendicular magnetic field, both samples show the full lifting of the Landau level degeneracy. In Fig. 3.1(a), we show R_{xx} of device A at 25 T and 1.4 K for the hole side ($V_G < V_G^{CNP}$). Minima in R_{xx} and quantized Hall plateaus in R_{xy} at $\nu = -1, -3, -4$, and -5 are well developed and more pronounced compared to those observed in the electron side. We will therefore focus our further analysis on the LLs for the holes. For device B, Fig. 3.1(b),

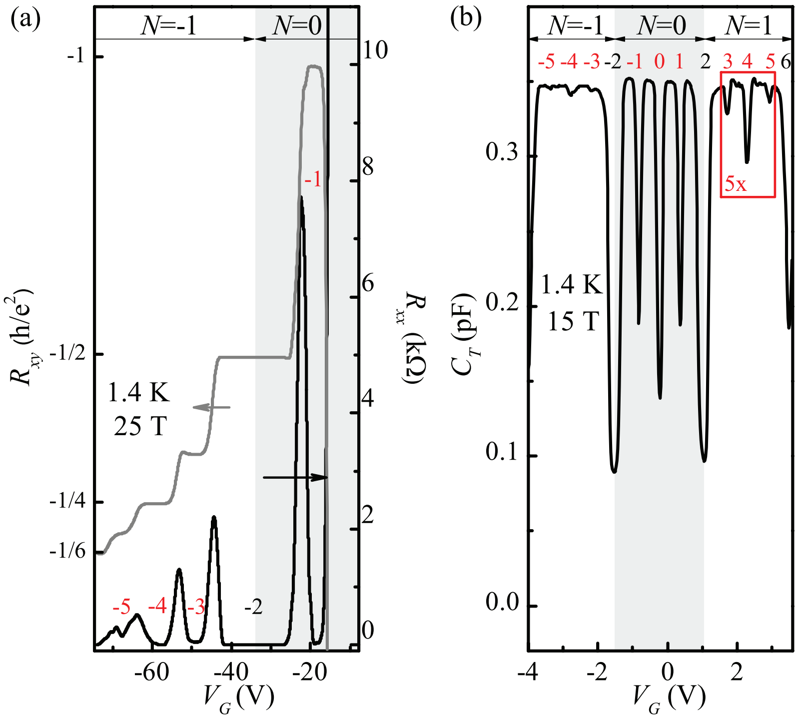

Figure 3.1: *Transport and capacitance measurements at 1.4 K. (a): R_{xx} (black line) and R_{xy} (gray line) as a function of the back gate voltage V_G at 25 T. (b): C_T as a function of the top gate voltage V_G at 15 T. The curve inside the red box is expanded five times and shifted in order to match the constant background of the original curve. The numbers close to the minima of R_{xx} and C indicate the filling factors.*

clear minima in the capacitance measurements are detected at each integer value of ν in $N = 0$ and $N = \pm 1$ at 15 T and 1.4 K. It is worth noting that the lifting of the LL degeneracy evolves progressively with the magnetic field, first in the lowest LL and then in the higher levels and, within each level, first at half filling and then at quarter filling. Hence, the first filling factor observed is $\nu = 0$, appearing as a clear minimum in C_T for $B \geq 5$ T and as a diverging R_{xx} for $B > 2$ T (see Fig.3.7(a), points connected by the grey line). Filling factors $\nu = \pm 1$ are well developed already at 10 T for both samples. For $B \geq 10$ T the full splitting of $N = \pm 1$ starts to be resolved in the capacitance spectroscopy. In transport measurements, plateaus in R_{xy} appear in the $N = -1$ LL, first at $\nu = -4$ (10 T), then at $\nu = -3$ (12.5 T, and finally at $\nu = -5$ (17.5 T).

3.2.2 Energy gaps in a perpendicular field

Let us now address the sizes of the energy gaps Δ_ν that are associated with the broken symmetry states in a purely perpendicular magnetic field (Fig. 3.2). As explained in section 2.3.5, we extract Δ_ν from temperature-activated transport experiments on device A between 1.4 and 18 K, fitting the experimental data according to the Fermi-Dirac distribution $R_{xx} \propto 1/(e^{\Delta_\nu/2k_BT}+1)$, since the size of the gap is comparable to k_BT in the temperature range under study.[26]

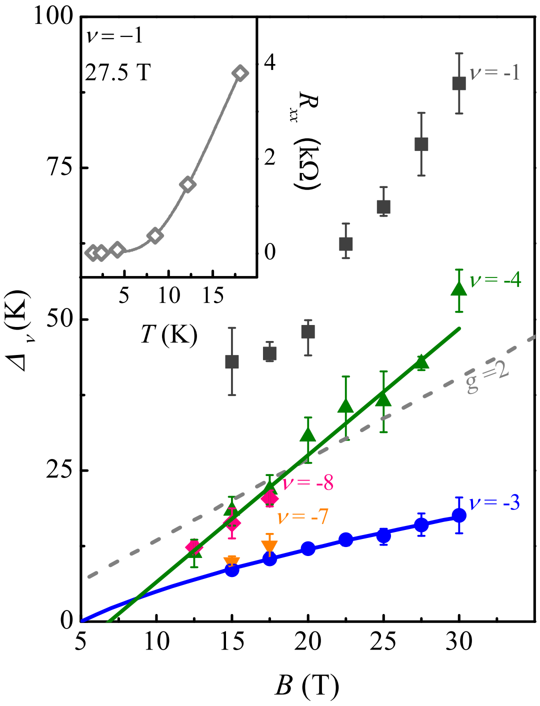

Figure 3.2: *Activation gaps Δ_ν as a function of B for $\nu = -1, -3, -4, -7$ and -8. The gray dashed line indicates E_Z calculated with $g = 2$, and the solid lines are the linear (green) and square root (blue) fit to the data. Inset: R_{xx} minima of $\nu = -1$ as a function of temperature at 27.5 T (symbols), and the solid line is a fit to the experimental data according to the Fermi-Dirac distribution. The relatively large error bars for gaps exceeding 20 K are due to the fact that the temperature range used ($1.4 - 18$ K) was not large enough to access them more accurately.*

The inset of Fig. 3.2 shows the minima of R_{xx} as a function of temperature for $\nu = -1$ at 27.5 T (symbols) and the fits (solid lines) as an example of typical fitting traces. Since there is some uncertainty in the range of applicability of the activated transport assumption, at some magnetic field values we had to perform different fits considering each time a different temperature range. The values of Δ_ν plotted in Figure 3.2 are an average over the values obtained fitting in the different temperature ranges, and the error bars represent the spread of all the values obtained due to the different fits.

As can be seen in Figure 3.2, the size of the energy gaps increases with the magnetic field for each filling factor. In the higher LLs ($N = -1$ and -2) we can distinguish between two different energy scales, one for the gaps at even ν and one for the gaps at odd ν. The size of Δ_{-4} and Δ_{-8} increases linearly with the magnetic field and the gaps for both filling factors fall on the same line. The gap size can be described by $\Delta = g\mu_B B - \Gamma$; the first term is the Zeeman energy (E_Z) and Γ is the Landau level broadening. A fit to the experimental data yields $g = 3.1 \pm 0.1$ and $\Gamma = 14.4 \pm 1.5$ K. The enhancement of g compared to its bare value 2 is probably due to exchange interaction.[27]

The gaps at odd filling factors within the $N = -1$ and $N = -2$ LLs, Δ_{-3} and Δ_{-7}, are comparable within the error bars. They are considerably smaller than E_Z and their field dependence can be fitted by a square root function with a finite offset representing a Landau level broadening of 12 ± 1 K (blue solid line for of Δ_{-3}). A linear function, which would also reasonably fit the data, leads to a meaningless negative value for Γ.

Though a shallow minimum develops in R_{xx} at $\nu = -5$ for $B > 17.5$ T, we are not able to extract the activated gap in the considered temperature range since the R_{xx} minimum is visible only at the lowest temperatures. Thus, we conclude that the state at $\nu = -5$ is weaker than the state at $\nu = -3$, as also suggested by the capacitance signal where dips at $\nu = \pm 5$ are not as pronounced as the ones at $\nu = \pm 3$ (see the curve inside the red box in Figure3.1(b)).

In addition, Figure 3.2 highlights already the different behaviour of the states within the lowest LL compared to the ones in the higher levels. Indeed we notice that $\nu = -1$ has the largest energy gap and, in particular, it is much larger than the size of the gaps of the other odd filling factor $\nu = -3$ and $\nu = -7$.

3.3 Tilted magnetic fields

In order to further investigate the origin of the broken symmetry states we perform magnetotransport and capacitance experiments in a tilted magnetic field. We tilt the sample with respect to the direction of the magnetic field by an angle θ, while keeping the component of the magnetic field perpendicular to the graphene plane ($B_\perp$) constant, thus increasing the total magnetic field

(B_T) applied to the sample. In a material like graphene, the effects related to the spin can be decoupled from those dependent on $B_\perp$ alone. For a complete description of the tilted fields experiments, see section 2.6 and Figure 2.13.
For device A, the experiments were performed in two different cooldowns, indicated by solid symbols (first cooldown) and open symbols (second cooldown) in Figures 3.5 and 3.6.

3.3.1 Higher Landau levels ($|N| > 0$)

We first describe the lifting of the Landau level degeneracy for the $N \neq 0$ levels. In Figure 3.3 (a), we illustrate the splitting of the higher LLs ($|N| > 0$) showing R_{xx} for different tilt angles. The minima in R_{xx} associated with even ν become more pronounced upon tilting the sample and increasing B_T, while those associated with the odd filling factors do not change. In particular, for $B_\perp = 8.4$ T and $\theta = 0°$, we observe only the standard sequence for the half-integer quantum Hall effect in graphene (Figure 3.3(a) black line) while at $\theta = 73.7°$ clear minima appear in R_{xx} at the filling factors $\nu = -4, -8$, and -12 (red line). At the higher value of $B_\perp = 14.1\,\mathrm{T}$ (black line in Figure 3.3 (b)), we

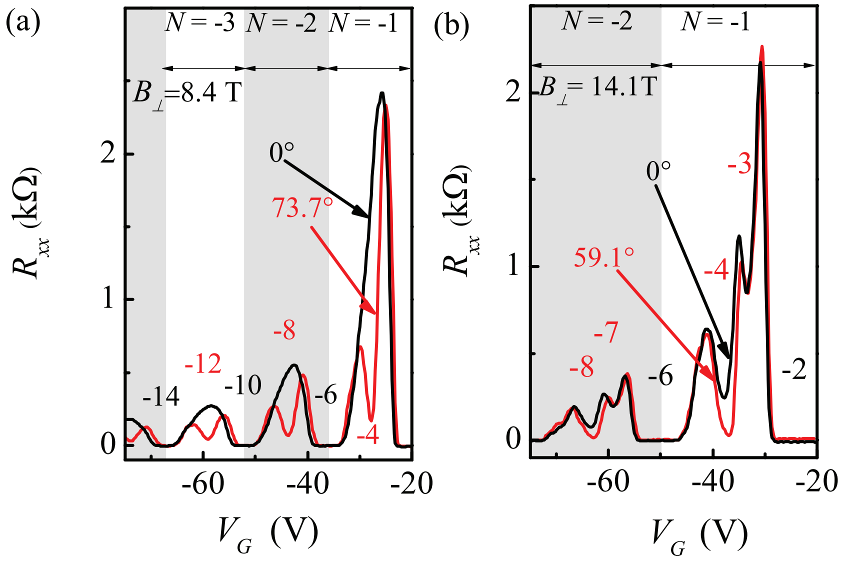

Figure 3.3: *Splitting of the higher Landau levels in a tilted magnetic field at 1.4 K. (a): R_{xx} as a function of the back gate voltage at $B_\perp = 8.4$ T and $\theta = 0°$ (black line) and at $\theta = 73.7°$ (red line). (b): R_{xx} for $N = -1$ and -2 at $B_\perp = 14.1$ T and $\theta = 0°$ (black line) and $\theta = 59.1°$ (red line).*

observe also the odd filling factors $\nu = -3$ and -7 which do not change upon an increase in B_T as the sample is tilted by 59.1° (red line).

In the capacitance signal shown in Figure 3.4, the minimum at $\nu = 4$ becomes progressively deeper as the sample is tilted from 0° to 63.2°, indicating that the state at $\nu = 4$ gets stronger upon an increase of B_T. In contrast, the minima at $\nu = 3$ and 5 in C (Fig.3.4(c)) do not show any significant change as the sample is tilted.

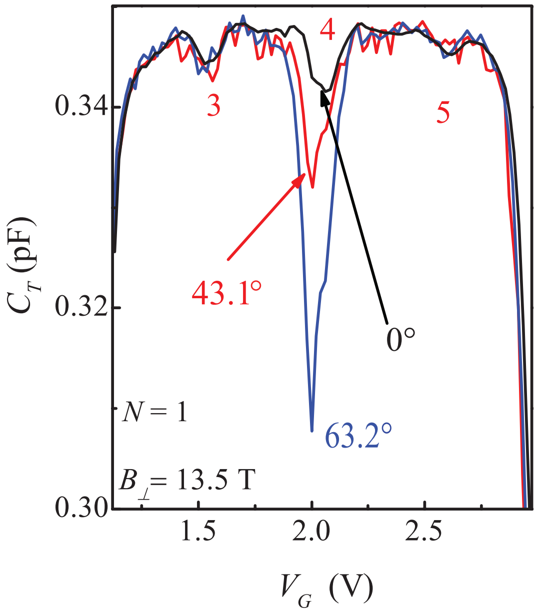

Figure 3.4: *Splitting of the $N = 1$ level observed in capacitance measurements at $B_\perp = 13.5$ T and 1.4 K for different tilt angles $\theta = 0°$ (black line), $\theta = 43.1°$ (red line) and $\theta = 63.2°$ (blue line).*

We address quantitatively the splitting mechanism for the higher energy LLs extracting the activation gaps in a tilted magnetic field. As Figure 3.5(a) shows, Δ_{-4}, Δ_{-8}, and Δ_{-12} increase linearly with B_T at a fixed $B_\perp = 10.4$ T and the gap size is smaller than the Zeeman energy (gray dashed line). The linear dependence of Δ_{-4} and Δ_{-8} on B_T is found at several $B_\perp$ (10.4, 11.3, 20, and 25 T, the last two only for Δ_{-4}).

At even ν, the gap size can be described as a result of two separate contributions reduced by the Landau level broadening, $\Delta_\nu = E(B_\perp) + E_Z(B_T) - \Gamma$. The first term, $E(B_\perp)$, incorporates all the effects which depend only on $B_\perp$, (e.g., electron-electron interactions) and therefore does not change upon an increase

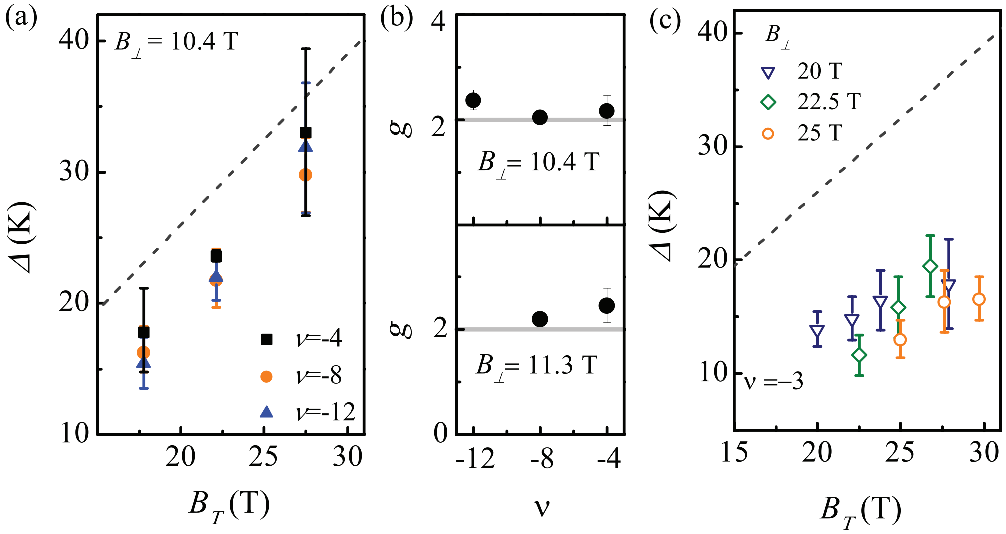

Figure 3.5: *(a): Activation gaps for $\nu = -4$ (black squares), $\nu = -8$ (orange circles) and $\nu = -12$ (blue triangles) as a function of B_T at $B_\perp = 10.4$ T. They gray dashed line represents E_Z for $g = 2$. (b): g as a function of ν at $B_\perp = 10.4$ T (top panel) and 11.3 T (bottom panel). (c): Δ_{-3} as a function of B_T at $B_\perp = 20$ T (blue triangles), 22.5 T (green squares) and 25 T (orange circles).*

of B_T. The value of g in a titled field can be calculated by the derivative of Δ_ν with respect to B_T, and it provides information about the spin of the excitation involved in the transport process.[21] The enhancement of g due to exchange interactions depends solely upon $B_\perp$ and therefore does not influence the calculation. A linear fit to the data leads to $g \approx 2$ for the three filling factors at each $B_\perp$ meaning that transport takes place via thermally excited electron-hole pairs with reversed spin with no collective effects, such as Skyrmions,[15,22] involved. To illustrate the behavior of g, we plot g as a function of ν at $B_\perp =$ 10.4 and 11.3 T as representative results in Figure 3.5 (b).

In contrast to the even filling factors, the value of Δ_{-3} (Figure3.5(c)) does not depend on B_T and is much smaller than the Zeeman energy. Therefore, we can assume that $\nu = -3$ originates from the lifting of the valley degeneracy in the $N = -1$ level.

3.3.2 The lowest Landau level (N=0)

We now turn our attention to the $N = 0$ LL, which, in a tilted magnetic field, behaves substantially different compared to the higher LLs. We first consider device A. Figure 3.6(a) shows that at $\nu = -1$ the minimum in R_{xx} becomes deeper, tilting the sample from $\theta = 0°$ (black solid line) to $\theta = 59.1°$ (red solid line) at $B_\perp = 14.1$ T. Accordingly, the gap associated with $\nu = -1$ increases with B_T (Figure 3.6(b)). The size of Δ_{-1} is larger than the Zeeman energy for $B_\perp \geq 20$ T, while it is compatible with E_Z within the error bars at smaller $B_\perp$. Furthermore, as in the case of the even ν in $|N| > 0$, we do not find any significant enhancement of g from the dependence of Δ_{-1} on B_T (see the dotted line in Figure 3.6(b)). This indicates that $\nu = -1$ separates two states with reversed spin and the enhancement of the gap size, with respect to E_Z, is governed by the exchange interaction due to $B_\perp$.

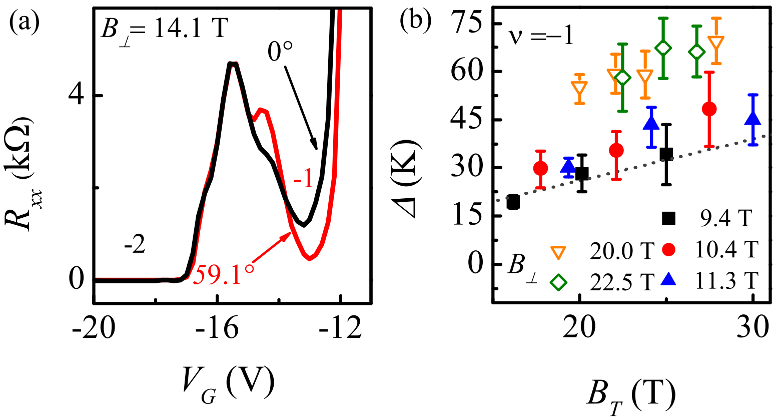

Figure 3.6: *$\nu = -1$ in a tilted magnetic field. (a): R_{xx} at $\nu = -1$ in $B_\perp = 14.1$ T and $\theta = 0°$ (black line) and $\theta = 59.1°$ (red line). (b) Activation gap for $\nu = -1$ as a function of B_T at different $B_\perp$; the gray dotted line is E_Z calculated with $g = 2$.*

At half filling of $N = 0$, the resistance maximum at $\nu = 0$ decreases with the in-plane magnetic field (see Fig.3.7(a)) having $B_\perp \geq 2$ T, confirming earlier observations on suspended[16] and hBN supported samples.[15] This observation suggests that Δ_0 is reduced upon increasing B_T, ruling out the scenario of a fully spin polarized state at half filled $N = 0$.

The capacitance measurements on device B in tilted magnetic fields support the picture emerging from the transport experiments. Figure 3.7(b) shows that all three ν resulting from the splitting of the zero energy Landau level react to a

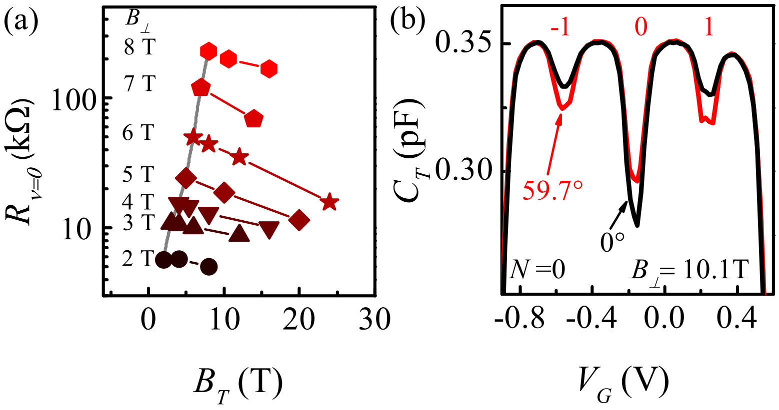

Figure 3.7: *Splitting of the $N = 0$ LL in a tilted magnetic field. (a): Value of the resistance maximum at $\nu = 0$ in a tilted magnetic field as a function of B_T at different $2 \leq B_\perp \leq 8$ T and 4.2 K. (b) C_T at $B_\perp = 10.1$ T and $\theta = 0°$ (black line) and $\theta = 59.7°$ (red line).*

change in θ at a fixed $B_\perp = 10.1$ T. We also notice that the odd filling factors ± 1 are enhanced by an increase in B_T, while the minimum at $\nu = 0$ becomes shallower as the sample is tilted from $\theta = 0°$ (black solid line) and $\theta = 59.7°$ (red solid line).

3.4 Discussion

The observation of the full splitting of the LLs in a perpendicular field and in particular, the presence of odd filling factors in $|N| \neq 0$, indicates that both samples enter the regime of the quantum Hall ferromagnetism for a high enough $B_\perp$[3,23] (see Section 2.3.4). In agreement with the QHF picture, we observe enhanced energy gaps in perpendicular field for both $\nu = -1$ and $\nu = -4$. In addition, the square root dependence of Δ_{-3} on $B_\perp$ suggests that its origin is due to electron-electron interactions.

The titled field experiments enable us to compose a splitting scenario which is different for the $N = 0$ level and the higher energy levels. In Figure 3.8, we draw schematically the splitting of the $N = 0$ and $N = -1$ LLs. Both levels are spin and valley degenerate for low $B_\perp$. The different spin states are indicated by ↑ and ↓, while the two valleys are depicted as the green and red lines. In the lowest level (left panel), the valley degeneracy is removed at $\nu = 0$, whereas the spin degeneracy is lifted at $\nu = \pm 1$.

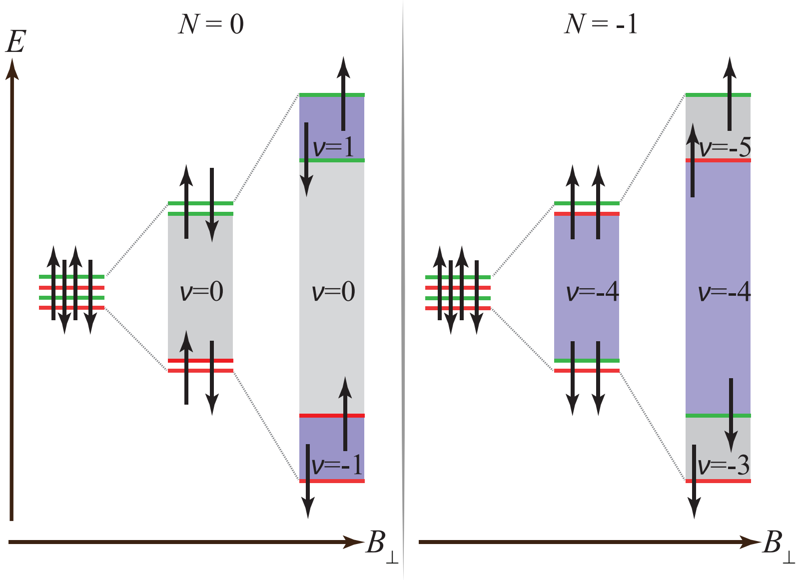

Figure 3.8: *Splitting scenario for the $N = 0$ (left panel) and the $N = -1$ (right panel) LLs. The two valleys are schematically indicated by the green and red lines, the spin of the carriers by* ↑ *and* ↓*. The energy gaps for the different ν are indicated by the grey (blue) shaded areas for the valley (spin) polarized states.*

Conversely, we find that for $N \neq 0$ the spin degeneracy is lifted at half filling (even ν) while the valley degeneracy is lifted at quarter filling (odd ν). As an example of the splitting of a higher energy LL, we show the schematic representation for the $N = -1$ LL in the right panel of Figure 3.8.
It is worth pointing out the difference between $\nu = -1$ and the filling factors originating from the spin splitting in the higher levels: the size of Δ_{-1} cannot be explained solely by the Zeeman energy, but it must find an origin in the electron-electron interactions, whereas the gaps at $\nu = -4, -8$ and -12 appear to be Zeeman dominated (see the size of the gaps reported in Figures 3.5 and 3.6).

3.5 Conclusions

In this Chapter we have addressed the lifting of the LL degeneracy by means of two different measurement techniques. In a purely perpendicular magnetic field, we have extracted the energy gaps by means of thermally activated transport.

The filling factors resulting from the splitting of the higher ($|N| > 0$) LL have comparable gap sizes, while the energy gap at $\nu = -1$ is considerably bigger than all the others. For the higher LLs, the states at even ν are stronger than the ones at odd ν.

Our experiments in tilted fields highlight the differences between the splitting of the $N = 0$ LL and the higher energy levels. The even filling factors in the $|N| > 0$ LLs separate two spin polarized states, while in the lowest LL, a spin polarized state is found at $\nu = -1$. Moreover Δ_{-1} is larger than the Zeeman energy, indicating that electron-electron interactions are the most relevant effect for the splitting of the $N = 0$ level. In contrast, the gaps of spin polarized states in the higher levels ($\nu = -4, -8$ and -12), are compatible with a the Zeeman splitting.

The splitting scenario obtained in the tilted field experiments and depicted in Figure 3.8 confirms the finding of Ref. 15, although we do not find any indication of the presence of skyrmion in our transport system at $\nu = -4$. We attribute this difference to the disorder that in our system is higher than in the devices studied by Young and collaborators,[15] as indicated by the lower carrier mobility of our sample.

References

[1] K. S. Novoselov, A. K. Geim, S. V. Morozov, D. Jiang, M. I. Katsnelson, I. V. Grigorieva, S. V. Dubonos, and A. A. Firsov, “Two-dimensional gas of massless Dirac fermions in graphene”, *Nature* **438**, 7065, 197–200 (2005).

[2] Y. Zhang, Y.-W. Tan, H. L. Stormer, and P. Kim, “Experimental observation of the quantum Hall effect and Berry’s phase in graphene”, *Nature* **438**, 7065, 201–204 (2005).

[3] J. Alicea and M. P. A. Fisher, “Graphene integer quantum Hall effect in the ferromagnetic and paramagnetic regimes”, *Physical Review B* **74**, 7, 75422 (2006).

[4] L. Sheng, D. N. Sheng, F. D. M. Haldane, and L. Balents, “Odd-integer quantum hall effect in graphene: Interaction and disorder effects”, *Physical Review Letters* **99**, 19, 196802 (2007).

[5] M. O. Goerbig, “Electronic properties of graphene in a strong magnetic field”, *Reviews of Modern Physics* **83**, 4, 1193–1243 (2011).

[6] I. F. Herbut, “Theory of integer quantum Hall effect in graphene”, *Physical Review B* **75**, 16, 165411 (2007).

[7] V. Gusynin, V. Miransky, S. Sharapov, and I. Shovkovy, “Excitonic gap, phase transition, and quantum Hall effect in graphene”, *Physical Review B* **74**, 19, 195429 (2006).

[8] W. Luo and R. Côté, “Zeeman coupling and screening corrections to skyrmion excitations in graphene”, *Physical Review B* **88**, 11, 115417 (2013).

[9] B. Roy, “Odd integer quantum Hall effect in graphene”, *Physical Review B* **84**, 3, 35458 (2011).

[10] Y. Zhang, Z. Jiang, J. P. Small, M. S. Purewal, Y. W. Tan, M. Fazlollahi, J. D. Chudow, J. A. Jaszczak, H. L. Stormer, and P. Kim, “Landau-level splitting in graphene in high magnetic fields”, *Physical Review Letters* **96**, 13, 136806 (2006).

[11] Z. Jiang, Y. Zhang, H. L. Stormer, and P. Kim, “Quantum hall states near the charge-neutral dirac point in graphene”, *Physical Review Letters* **99**, 10, 106802 (2007).

[12] L. Zhang, J. Camacho, H. Cao, Y. Chen, M. Khodas, and De, "Breakdown of the N= 0 quantum Hall state in graphene: Two insulating regimes", *Physical Review B* **82**, c, 1–4 (2009).

[13] A. J. M. Giesbers, L. A. Ponomarenko, K. S. Novoselov, A. K. Geim, M. I. Katsnelson, J. C. Maan, and U. Zeitler, "Gap opening in the zeroth Landau level of graphene", *Physical Review B* **80**, 20, 201403 (2009).

[14] J. G. Checkelsky, L. Li, and N. P. Ong, "Zero-energy state in graphene in a high magnetic field", *Physical Review Letters* **100**, 20, 206801 (2008).

[15] A. F. Young, C. R. Dean, L. Wang, H. Ren, P. Cadden-Zimansky, K. Watanabe, T. Taniguchi, J. Hone, K. L. Shepard, and P. Kim, "Spin and valley quantum Hall ferromagnetism in graphene", *Nature Physics* **8**, 7, 550–556 (2012).

[16] Y. Zhao, P. Cadden-Zimansky, F. Ghahari, and P. Kim, "Magnetoresistance measurements of graphene at the charge neutrality point", *Physical Review Letters* **108**, 10, 106804 (2012).

[17] F. Amet, J. R. Williams, K. Watanabe, T. Taniguchi, and D. Goldhaber-Gordon, "Selective equilibration of spin-polarized quantum hall edge states in graphene", *Physical Review Letters* **112**, 19, 196601 (2014).

[18] G. L. Yu, R. Jalil, B. Belle, A. S. Mayorov, P. Blake, F. Schedin, S. V. Morozov, L. a. Ponomarenko, F. Chiappini, S. Wiedmann, U. Zeitler, M. I. Katsnelson, a. K. Geim, K. S. Novoselov, and D. C. Elias, "Interaction phenomena in graphene seen through quantum capacitance.", *Proceedings of the National Academy of Sciences of the United States of America* **110**, 9, 3282–6 (2013).

[19] S. L. Sondhi, A. Karlhede, S. A. Kivelson, and E. H. Rezayi, "Skyrmions and the crossover from the integer to fractional quantum Hall effect at small Zeeman energies", *Physical Review B* **47**, 24, 16419–16426 (1993).

[20] H. A. Fertig, L. Brey, R. Côté, and A. H. MacDonald, "Charged spin-texture excitations and the Hartree-Fock approximation in the quantum Hall effect", *Physical Review B* **50**, 15, 11018–11021 (1994).

[21] A. Schmeller, J. P. Eisenstein, L. N. Pfeiffer, and K. W. West, "Evidence for skyrmions and single spin flips in the integer quantized hall effect", *Physical Review Letters* **75**, 23, 4290–4293 (1995).

[22] K. Yang, S. Das Sarma, and A. H. MacDonald, "Collective modes and skyrmion excitations in graphene SU (4) quantum Hall ferromagnets", *Physical Review B* **74**, 7, 75423 (2006).

[23] K. Nomura and A. H. MacDonald, "Quantum hall ferromagnetism in graphene", *Physical Review Letters* **96**, 25, 256602 (2006).

[24] a. F. Young, J. D. Sanchez-Yamagishi, B. Hunt, S. H. Choi, K. Watanabe, T. Taniguchi, R. C. Ashoori, and P. Jarillo-Herrero, "Tunable symmetry breaking and helical edge transport in a graphene quantum spin Hall state.", *Nature* **505**, 7484, 528–32 (2014).

[25] S. Luryi, "Quantum capacitance devices", *Applied Physics Letters* **52**, 6, 501–503 (1988).

[26] E. V. Kurganova, A. J. M. Giesbers, R. V. Gorbachev, A. K. Geim, K. S. Novoselov, J. C. Maan, and U. Zeitler, "Quantum Hall activation gaps in bilayer graphene", *Solid State Communications* **150**, 45-46, 2209–2211 (2010).

[27] E. V. Kurganova, H. J. Van Elferen, A. McCollam, L. A. Ponomarenko, K. S. Novoselov, A. Veligura, B. J. Van Wees, J. C. Maan, and U. Zeitler, "Spin splitting in graphene studied by means of tilted magnetic-field experiments", *Physical Review B* **84**, 12, 121407 (2011).

CHAPTER 4

Capacitance spectroscopy in the $N = 0$ Landau level

Abstract

In this Chapter, we address the splitting of the lowest Landau level of graphene by means of capacitance measurements in a tilted magnetic field. In our experiment, we have tilted the sample up to 81.4° *and observed a non-monotonic behaviour of the minima associated to* $\nu = 0$ *and* $\nu \pm 1$ *as* B_T *is increased. From the analysis of the energy gaps associated to the filling factors, we show that the state at* $\nu = 0$ *is first suppressed by an increase in* B_T *but it gets strongly enhanced again at the highest angles, when the ratio* $B_T/B_\perp$ *is maximized. Such a behaviour is compatible with the formation of a valley polarized state in a purely perpendicular magnetic field which evolves into a spin polarized state owing to the enhancement of the Zeeman energy.*

Part of this work is in preparation for publication.

4.1 Introduction

One of the consequences of the Dirac nature of charge carriers in graphene is the formation of a zero energy Landau level in an external magnetic field. As described in section 2.3.3, the presence of the $N = 0$ Landau level is typical of Dirac fermions and represents the main difference between graphene and the traditional semiconductor-based 2D systems. This level is four times degenerate, similarly to the other Landau levels, and it separates the filling factors $+2$ and -2.

More interestingly, the lowest energy level differs from all the other levels in graphene as it is equally shared by electrons and holes and the wavefunctions in the different valley K and K' reside on the different sublattice sites A and B (see Figure 2.1 (a)). Therefore, only for this specific level, valley and sublattice polarization coincide.

It was observed experimentally that the $N = 0$ LL under the condition of high magnetic fields and low temperature, can split into 4 levels leading to the observation of the additional filling factors 0 and ± 1.[1–8] The latter emerged as clear quantum Hall states ($R_{xx} = 0$ and $R_{xy} = h/e^2$) already in the early stage of the graphene research,[1,2] while the state at $\nu = 0$ manifested as divergent R_{xx} and R_{xy}.[1,3–8] The insulating state at $\nu = 0$, detected in all kind of graphene devices (SiO_2, suspendend and hBN supported), seems to become stronger with the increasing quality of the devices.[1,8]

The nature of the ground state occurring at $\nu = 0$ has been stimulating an intense theoretical debate aimed at describing what kind of microscopic ordering could explain the observed insulating state. Within the framework of the quantum Hall ferromagnetism of graphene[9](see section 2.3.4), several ground states have been proposed: the spin ferromagnetic phase (F),[10–12] the canted antiferromagnetic (CAF) order,[10,13] the charge density wave (CWD)[10,11] and the Kekulé distortion (KD).[14,15] The selection of a specific ground state depends on the competition of different energies (Zeeman energy, electron-electron interactions and electron-phonon interaction at the lattice scale) and theoretically, it is hard to predict which ordering will prevail because the different ground states have very similar energies. Therefore, the specificities of each sample like disorder or the interaction of the graphene with the surrounding media, might be determinant in driving the system into a specific ground state at $\nu = 0$.

Indeed, experimental works have reported different ground states at $\nu = 0$. A recent work[16] employing optical spectroscopy sensitive to the valley polarization have proved a CDW ordering, while Young *et al.* using a combination of transport and capacitance have reported a CAF state occurring at $\nu = 0$.[17] Several other works excluded a spin polarized state at $\nu = 0$ by means of transport measurements in a tilted magnetic field.[7,8,18]

In this Chapter, we investigate the splitting of the lowest Landau levels by means of capacitance measurements in tilted magnetic field. In this study we employ a graphene based capacitor, where the graphene flake is sandwiched between two layers of hBN. Since we use a low perpendicular component of the magnetic field, the bulk of the graphene does not become strongly insulating (see section 2.4.3) and therefore we are able to extract quantitative information from the capacitance data and describe the ground state occurring at $\nu = 0$ and ± 1 in terms of energy gaps.

We study the behaviour of $\nu = 0$ and ± 1 as a function of the tilt angle θ. We observe the complete suppression of filling factor 0 and its successive enhancement, as the sample is tilted at the highest angles. In contrast, $\nu = \pm 1$ are enhanced as the sample is tilted up to $\theta \sim 60°$, while, for $\theta > 60°$, they are not affected by the increment of B_T .

In the final part of this Chapter, we interpret the experimental findings in terms of a phase transition between two of the proposed states for $\nu = 0$, namely the CD or KD as initial state, to the F or CAF ordering as the final state.

4.2 Sample characterization

The sample used in this study is a graphene-based capacitor similar to the ones described in section 2.4. An optical picture of the sample is shown as inset of figure 4.1. An heterostructure formed by the stack of hBN-graphene-hBN is deposited on a quartz substrate. The large Au contacts (marked by the red dashed lines) are connected to the graphene sheet (invisible in the picture) while the three Au plates are deposited on top of the hBN layer (brown area in the figure). The irregular shape of the plates is specifically designed in order to avoid the bubbles that are formed during the stacking process[19] and that are visible at the hBN surface. The thickness of the hBN layer between the graphene and the gold plate is $d = 45\,\text{nm}$ (obtained by AFM measurements).

The capacitance of the device highlighted by the blue area was measured using a current amplifier (Keithley 428) sending an ac voltage excitation of $20\,\text{mV}$ at $f = 23.7\,\text{kHz}$.

As shown in Figure 2.9 (b) and described in section 2.4, the system can be modelled as a resistor R and a capacitor C_T connected in series. R includes all the resistive part of the experimental set up and the resistance of the graphene sheet, while C_T includes the capacitance of the device and the parasitic capacitance due to the wiring and the cables.

The impedance of the device highlighted by the blue area was measured sending an ac voltage excitation of 20 mV at 23.7 kHz and reading the current I flowing through the capacitor using the current amplifier. If $1/(RC_T) >> 2\pi f$, the component of the current at a 90° with respect to the excitation voltage ($\mathrm{Im}(I)$) is directly proportional to the capacitance of the system C_T (see eq.2.34). The component of the current in phase with the external excitation ($\mathrm{Re}(I)$) is proportional to R and is related to the dissipation in the system (see eq.2.33). We define the loss angle $\delta = \arctan \frac{\mathrm{Re}(I)}{\mathrm{Im}(I)}$. When the signal is purely capacitive ($R = 0$) or $1/(RC_T) >> 2\pi f$, $|\delta| = 0$. At the beginning of the measurements, the signal is rotated such that $\delta = 0$ for high gate voltage values (when the resistivity of the sample is expected to be the smallest, see for example Figure 2.3 (c)) in order to compensate for the artificial phase shift (usually below 10°) introduced by the experimental set-up (such as internal phase shifts due to the amplifier and cables).

Figure 4.1 shows the total capacitance C_T and the loss angle $|\delta|$ of the device as a function of the gate voltage V_G at 1.4 K and $B = 0$. C_T shows the V-shape typical of graphene capacitors[20–22] around the charge neutrality point ($V_G \approx -0.16\,\mathrm{V}$). Away from the neutrality point on both the electron and the hole side, C_T smoothly increases till reaching the value $C_T \approx 0.135$. The loss angle δ is non zero only in the vicinity of the charge neutrality point, where the resistivity of the graphene is the largest (see for example the resistance of a graphene field effect transistor shown in Figure 2.3(c)).

The qualitative understanding of the capacitance measurements was provided in section 2.4.2. More quantitative information on the electronic properties of the devices can be obtained by converting the experimental curves C_T as function of V_G into density of states as a function of the chemical potential of the system. As described by equation 2.36, 2.37 and 2.38, the total capacitance of the device consists of three contributions $C_T = (C_Q^{-1} + C_G^{-1})^{-1} + C_P$ and the quantum capacitance C_Q is directly proportional to the DOS of the system. Thus, the DOS can be extracted from the measured signal knowing C_G and C_P. Furthermore, we can obtain the chemical potential μ of the system as

$$\mu = \frac{1}{Se^2} \int \frac{1}{C_Q} dn \tag{4.1}$$

where S is the surface of the device, n is the charge carrier concentration and $\mu = 0$ at the CNP.

In general, the value of C_G can be calculated knowing the geometrical parameters of the devices and the dielectric constant of hBN. In practice, the area of the device is not known precisely since we do not know the actual position of the graphene sheet under the dielectric layer. The graphene layer may extend over an area larger than the Au plate causing the thinner contact paths to contribute

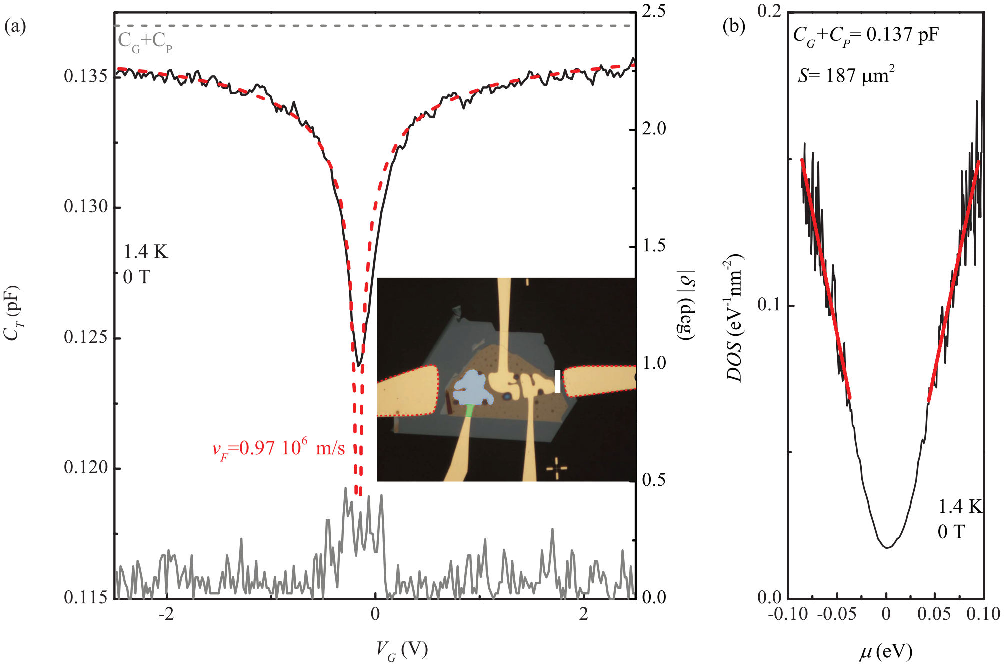

Figure 4.1: *C_T (black line) and $|\delta|$ (gray line) as a function of the gate voltage at 1.4 K. The red dashed line is the calculation of the total capacitance using the parameters C_P and C_G obtained following the procedure described in the appendix A and the Fermi velocity $v_F = 0.97 \times 10^6$ m/s. Inset: optical picture of the sample. The white bar defines 10 μm. The left device is considered in the experiment, while the other two are not connected. The blue area defines S_{min} while S_{max} is given by the the blue and the green areas together. (b): DOS obtained from the data of panel (a) as a function of the chemical potential for $C_G + C_P = 0.137$ pF and S_{min}. The red solid lines are linear fits according to eq.2.5.*

to the effective area of the device. For the device under consideration, we can therefore define a minimum area $S = 187\,\mu\text{m}^2$ (the blue area in the optical picture in figure 4.1) and a maximum one $S = 203\,\mu\text{m}^2$ (the blue and the green areas). These values are obtained from AFM pictures.

In addition, there is some uncertainty on the value of the dielectric constant of hBN. In literature, we find values of ϵ_{BN} ranging from 2 to 4.5.[21,23,24]

Another source of uncertainty is given by the parasitic capacitance C_P, which depends on the specific wiring of the stick, the measurement set up and the frequency of the external excitation. A correct value of C_P is crucial to the calculation of the charge induced in the system, and thus, to the chemical potential.

It is now obvious that any calculation of C_Q starting from non accurate values of C_G and C_P will provide a poor, if not unphysical, estimate of the actual DOS and the chemical potential of our system. Our approach is therefore to derive ϵ_{BN}, C_G and C_P directly from the experimental curves. The dielectric constant of hBN is now obtained from the periodicity of the oscillations of the capacitance in a perpendicular magnetic field. The other two parameters are calculated comparing the experimental DOS with the expected value according to the theoretical expression 2.5. The complete procedure is reported in detail in Appendix A.

For the device under investigation, we obtain $\epsilon_{BN} = 2.42$. At the end of the procedure described in Appendix A, we usually determine a unique values of S (and therefore C_G). However, only for this specific device, the high noise present in the data does not allow us to discriminate between S_{min} and S_{max} when comparing the slope of the DOS with the theoretical traces (see Appendix A). We obtain, therefore, two values for the geometrical capacitance $C_G = 0.089\,\text{pF}$ and $C_G = 0.096\,\text{pF}$. In the following part, when presenting C, μ and the DOS we will show only the curves obtained for S_{min}. This means that the shown traces represent and upper bound for μ and the DOS.

Figure 4.1 (b) displays the DOS calculated from C_T reported in panel (a). At low energies ($\mu \approx 0$), we observe a saturation of the DOS to a finite value. This deviation from the ideal behaviour reported in Figure 2.2 is most probably due to the presence of puddles in the graphene, which smear the DOS at low energies.[22,25,26] Away from the CNP, the DOS is linear as a function of μ. A linear fit (red solid lines) to the DOS according to eq.2.5 leads to a value for $v_F = 0.97 \times 10^6 \pm 0.05\,\text{m/s}$. This value is in agreement with theoretical expectations (see Section 2.1.1) and previous experimental reports.[21,27–29]

In order to check the validity these results, we can calculate C_T starting from the the values obtained of $C_G = 0.089\,\text{pF}$, $C_P = 0.048\,\text{pF}$ and v_F and compare it with the measured trace. As you can see in Figure 4.1 (a), the calculated curve (red dashed lines) reproduce nicely the experimental data except in the vicinity of the CNP.

Since the value of C_P is known, we can subtract it from the measured capacitance C_T and obtain the capacitance value due only to the the device $C = C_T - C_P$. In the following parts while presenting the experimental results, we will refer only to C.

4.2.1 Perpendicular magnetic field

When a magnetic field is applied to the sample, we observe oscillations in C, the capacitance of the device, as a consequence of the formation of the four-fold degenerate Landau levels. Figure 4.2(a) shows C (note that C_P was subtracted from the original data) and $|\delta|$ as a function of V_G at 1 T and 1.4 K. Already at such a low magnetic field, we observe clearly defined oscillations corresponding to the fourfold degenerate Landau levels (see section 2.3). The minima for $\nu = \pm 2$ are significantly deeper than the ones for the other filling factors and they are accompanied by peaks in the loss angle. This implies that the quantum Hall state at $\nu = \pm 2$ is strongly insulating already for $B = 1\,\mathrm{T}$.

Using the parameters obtained in Appendix A and equation 4.1, we can calculate the chemical potential and the DOS in the external magnetic field of 1 T. The chemical potential, shows a series of steps corresponding to the energy gaps associated to a specific filling factor (see figure 4.2(b)). The DOS, displayed in panel (c) as a function of the chemical potential, consists of several non-equidistant peaks that represents the different Landau levels.

However, the conversion of the data into DOS and μ should be applied carefully for the C traces obtained in the presence of an external magnetic field. As explained in section 2.4.3, when the bulk of graphene is insulating and $1/(RC_T) < 2\pi f$, the measured capacitance is smaller than the actual capacitance of the devices, because the device is only partially charged by the external excitation. Under this condition, it is not possible to relate C and the DOS. As a consequence, the energy gaps extracted from the steps in the chemical potential (figure 4.2(b)) are overestimated. This is certainly the case for $\nu = \pm 2$ already at $B = 1\,\mathrm{T}$. Indeed, if we extract the energy gaps from μ and compare their values with the ones expected for the cyclotron gaps for single layer graphene (eq.2.18), we see that $\Delta_{\pm 2}$ at 1 T exceeds the theoretical value (figure 4.3(a)). For this reason, the low energy part of the DOS is not shown in Figure 4.2 (c). The insulating state for the other filling factors in not yet strongly developed, as we do not detect any shift in the phase of the signal for $\nu \neq |2|$ (figure 4.2(a)) and the values for the gaps for $\nu = \pm 6$ and ± 10 are compatible with the their expected value (taking into account a finite broadening of the Landau levels).

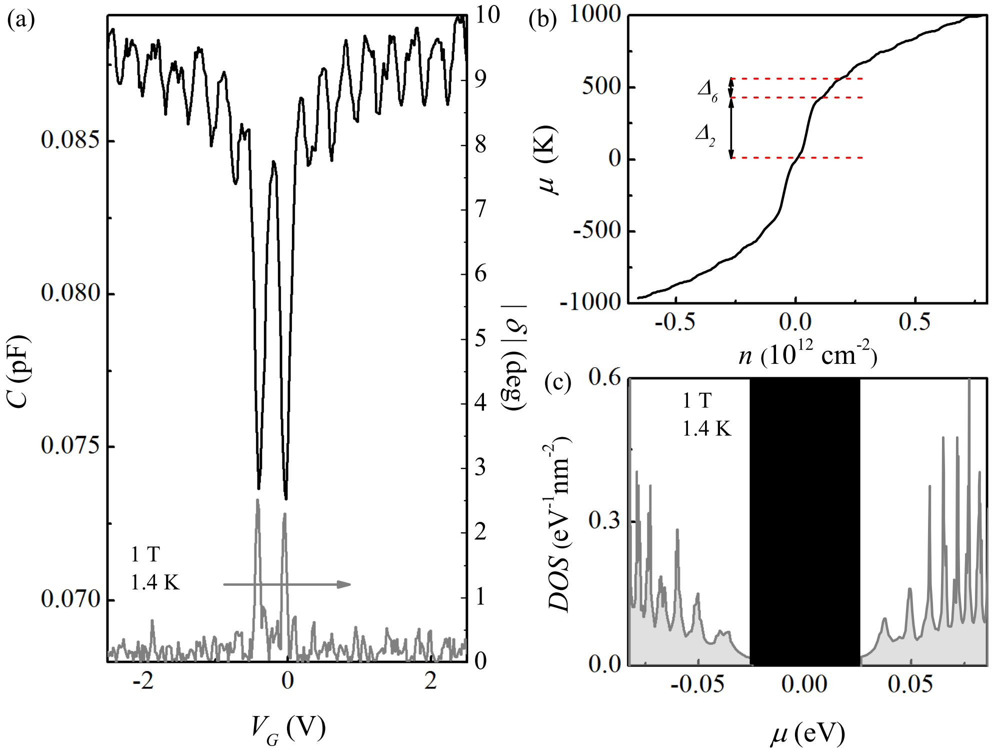

Figure 4.2: *(a): C and $|\delta|$ as a function of V_G at 1 T and 1.4 K. (b): Chemical potential as a function of n obtained from the experimental trace reported in panel (a). As an example, the steps corresponding to $\nu = 2$ and 6 have been highlighted and the height of the steps can be regarded as the energy gap associated to the integer ν. (c) DOS as a function of μ. Due to the highly insulating state at $\nu = \pm 2$, the conversion to DOS is not reliable in the low energy region and therefore it is not displayed.*

The comparison between the measured value for the gaps and their expected value provides us with a useful criterion to decide if the experimental data can be converted reliably to DOS and μ. Figure 4.3(a) shows $\Delta_{\pm 6}$ and $\Delta_{\pm 10}$ as a function of B at low magnetic field. Panel (b) displays the dependence of $|\delta|$ on the magnetic field for the same filling factors. We notice that as long as $|\delta| < 5°$, the size of the gap is well described by the expected value. On the other hand for $|\delta| > 5°$, Δ exceeds the cyclotron gaps, meaning that the capacitance signal is affected by the partial charging of the device. We therefore consider $|\delta| = 5°$ as the limit to perform a reliable conversion into DOS and the extraction of Δ_ν.

In section 2.4.2, we illustrate that the height of the *Loss* peaks has a non-monotonic behaviour as a function of the external magnetic field. As shown in figure 2.12, the height of the peaks crosses a maximum as a function of the magnetic field. Subsequently the height decreases and eventually each peak evolves into a multi-peak structure. The 5° limit is considered to hold only when the *Loss* experiences the initial increase as a function of the magnetic field.

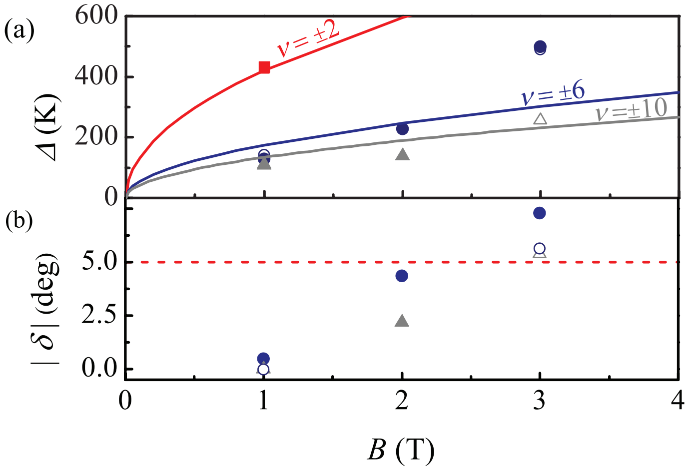

Figure 4.3: *Energy gaps and $|\delta|$ as a function of the external magnetic field at 1.4 K. (a): Comparison between the measured gaps (symbol) and their expected value (solid lines) for $\nu = \pm 2$ (red squares and red line), $\nu = \pm 6$ (blue circles and blue line), and $\nu = \pm 10$ (gray triangles and gray line). Solid (open) symbols indicate the negative (positive) filling factor. (b): $|\delta|$ for low magnetic fields. The horizontal red line marks $|\delta| = 5°$ which we take as limiting value for a reliable conversion of the capacitance data into DOS.*

Although a large $|\delta|$ effectively means that no quantitative information can be obtained from the capacitance data, it is worth noting that a large $|\delta|$ signal and the reduced C are the consequences of the presence of an insulating bulk which is related to the strength of the associated quantum Hall state. Indeed, a deeper minimum in C points to a smaller effective area of the capacitor which is a consequence of a more insulating bulk and, therefore, of a stronger quantum Hall state. The capacitance data in a high magnetic field provide thus a source of qualitative information to understand the evolution of the different ν even in the presence of a highly insulating bulk of sample.

4.3 Splitting of the $N = 0$ Landau level

We focus now on the lowest Landau level and on the filling factors resulting from the splitting of it into four distinct levels in a purely perpendicular magnetic field. Figures 4.4 (a), (b) and (c) show C as a function of the gate voltage for three different values of perpendicular magnetic field $B = 0\,\mathrm{T}$, $B = 3\,\mathrm{T}$ and $B = 7.5\,\mathrm{T}$, respectively. The minimum corresponding to the CNP at 0 T (panel (a)) evolves into a local maximum when an external magnetic field is applied to the system (panel (b)), indicating the formation of the $N = 0$ LL. At $B = 7.5\,\mathrm{T}$,

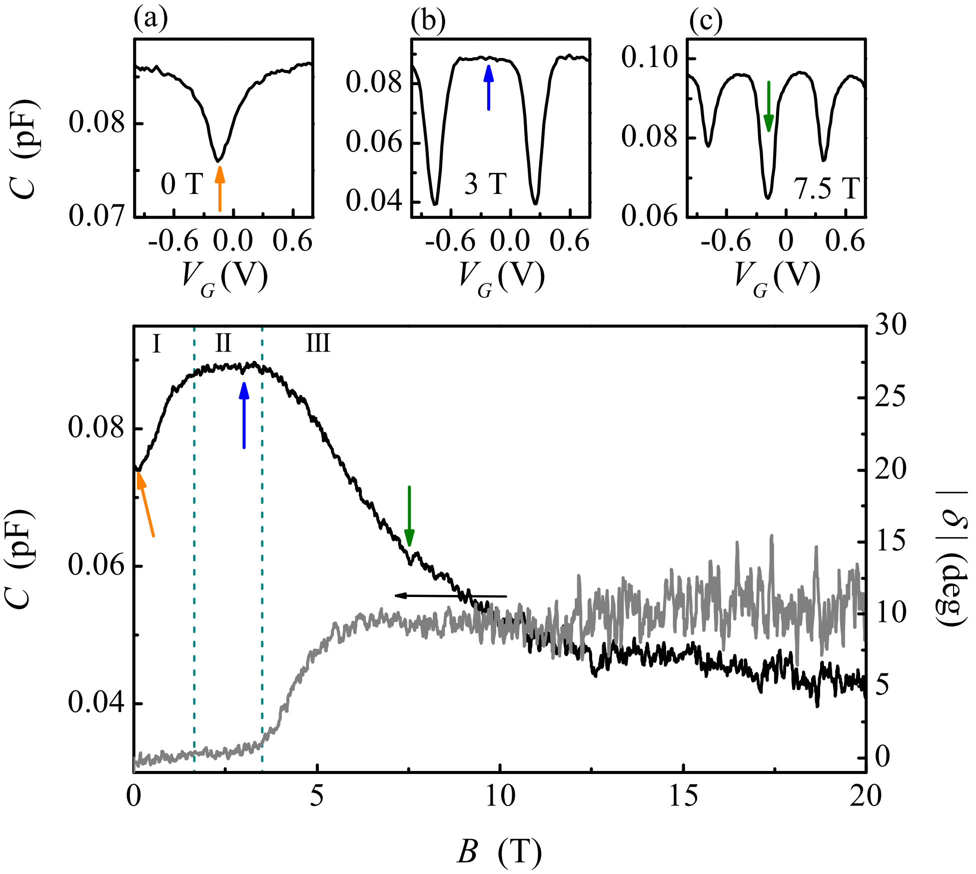

Figure 4.4: *Main panel: Capacitance and $|\delta|$ (right axis) as a function of the external perpendicular magnetic field at $1.4\,K$ and $V_G = V_{CNP} = -0.23\,V$. Top panels: C as a function of V_G at (a) $0\,T$, (b) $3\,T$ and (c) $7.5\,T$. The arrows indicate the position of the CNP or $\nu = 0$*

the splitting of the $N = 0$ is observed with three minima corresponding to $\nu = 0$ (the central minimum, indicated by the green arrow in panel (c)) and $\nu = \pm 1$ (the side minima in panel (c)).

The complete evolution of C at the CNP with the external magnetic field is shown in the main panel of Figure 4.4. The orange, blue and green arrows indicate the values of C at the CNP reported in the three top panels. In region I, C increases while the $N = 0$ level is formed. In region II, the lowest Landau level is fully developed and not yet split, C is field-independent. In region III ($B > 3.5\,\mathrm{T}$), C decreases because of the formation of $\nu = 0$.

The loss angle $|\delta|$ remains close to zero in regions I and II, due to the finite value of resistance of the graphene bulk. When $\nu = 0$ is developed (region III), $|\delta|$ presents a steep rise and crosses the 5° value for $B \simeq 5\,\mathrm{T}$, in agreement with the formation of an insulating state. Because of this, the capacitance data cannot be used to calculated the DOS for $B > 5\,\mathrm{T}$.

Figure 4.4 shows that we observe the lifting of the degeneracy of $N = 0$ at half filling for $B \approx 3.5\,\mathrm{T}$ while a weak minimum for $\nu = +1$ appears only above $4\,\mathrm{T}$ (see figure 4.5 (a)). As in the case of the devices described in Chapter 3, the splitting of the lowest Landau level occurs first at half filling ($\nu = 0$) and subsequently at $\nu \pm 1$, already indicating that $\nu = 0$ is stronger than $\nu = \pm 1$.

4.3.1 Tilted magnetic fields

In order to characterize the ground state occurring at $\nu = 0$ and ± 1 and study their possible spin polarization, we measure the capacitance of the device in a tilted magnetic field. During these experiments the perpendicular component of the field $B_\perp$ is kept constant while tilting the sample in the external magnetic field B_T by an angle θ. For a detailed explanation of the tilted field experiments and a sketch of the titling configuration, we refer to section 2.6.

In Figure 4.5, we show the capacitance of the sample in a tilted magnetic field for $B_\perp = 4\,\mathrm{T}$ (panel (a)), $B_\perp = 4.5\,\mathrm{T}$ (panel (b)) and $B_\perp = 5\,\mathrm{T}$ (panel (c)). These low values of $B_\perp$, although high enough to observe the splitting of the Landau level, allow us to tilt the device up to an angle $\theta = 81.4^\circ$. Furthermore, the small perpendicular component assures that $|\delta| \leq 5^\circ$ for most of the traces, enabling us to extract the chemical potential for $\nu = 0$ and ± 1 as a function of the tilt angle θ.

In a tilted magnetic field, for $\theta \leq 78.6^\circ$, the behaviour of the three filling factors is similar to the one reported in Chapter 3. When the sample is tilted and B_T increases, the minimum of C associated to $\nu = 0$ becomes more shallow while the minima at $\nu = \pm 1$ become more pronounced. This effect is clearly displayed in Figure 4.5 (a), (b) and (c). The black traces correspond to the case

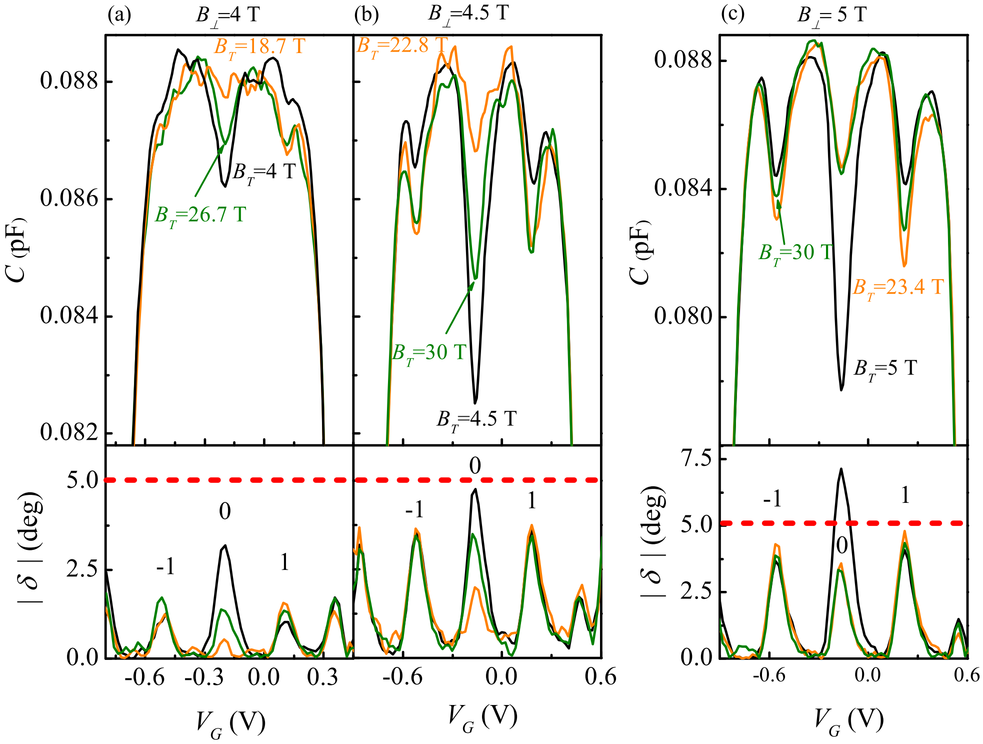

Figure 4.5: *Capacitance measurements of $N = 0$ Landau level in a tilted magnetic field. (a) Top panel: C as a function of the gate voltage at 1.4 K and $B_\perp = 4$ T. The three curves have $B_T = 4$ (black line), 18.7 (orange line) and 26.7 T (green line). Bottom panel: $|\delta|$ as a function of V_G for the same B_T as in the top panel. The numbers close to the maxima of the traces indicate the filling factor, the red dashed line corresponds to $|\delta| = 5°$. (b): Same as in panel (a) but for $B_T = 4.5$ (black line), 22.8 (orange line) and 30 T (green line). (c) same as in panel (a) but for $B_\perp = 5$ T (black line) and $B_T = 23.4$ (orange line) and 30 T (green line). $|\delta|$ for $B_\perp = B_T = 5$ T exceeds the 5° limit (black line in the bottom panel).*

$B_\perp = B_T$, while the orange ones have $B_\perp = 4$ T and $B_T = 18.7$ T (panel (a)), $B_\perp = 4.5$ T and $B_T = 22.8$ T (panel (b)), and $B_\perp = 5$ T and $B_T = 23.4$ T (panel (c)). Whereas in a purely perpendicular magnetic field the state at $\nu = 0$ is stronger than $\nu \pm 1$, an increase in B_T leads to a strong enhancement of $\nu = \pm 1$ which show the deepest minima. Interestingly, $B_T = 18.7$ T suppresses $\nu = 0$ completely for $B_\perp = 4$ T.

An opposite trend is observed if the sample is further tilted and, therefore, B_T

is also increased (green solid lines in panels (a) and (b)). Panel (a) shows that the C minimum at ν appears again for $B_T = 26.7\,\mathrm{T}$, and panel (b) shows that the minimum at $\nu = 0$ becomes significantly deeper than the one obtained for $B_T = 22.8\,\mathrm{T}$. The filling factors ± 1 are not affected by the increased B_T.

For $B_\perp = 5\,\mathrm{T}$, the minimum at $\nu = 0$ does not change if the sample is tilted at $\theta = 80.4^\circ$ and B_T is set to $30\,\mathrm{T}$ while $\nu = \pm 1$ are reduced compared to the trace obtained at a smaller angle (green line, panel (c)).

The loss angle δ shows a trend consistent with the one of the capacitive component of the signal. Indeed, for $\nu = 0$ at $B_\perp = 4\,\mathrm{T}$ and $B_\perp = 4.5\,\mathrm{T}$, we observe a decrease in the height of the peak of $|\delta|$ when the external field is increased to $B_T = 18.7$ and $B_T = 22.8\,\mathrm{T}$ respectively, indicating a reduction in the bulk resistivity. At the higher tilt angle, the increase of B_T reinforces the state resulting in an increase of $|\delta|$ (Figure 4.5 (a) and (b), bottom panels). A similar behaviour is observed also for $B_T = 5\,\mathrm{T}$ (Figure 4.5 (c), bottom panel) although, at the maximum field of $30\,\mathrm{T}$ we do not detect any increase in $|\delta|$.

The depth of the minima of C depends strongly on the perpendicular component of the magnetic field. Indeed, as shown in panels (a) and (b) which have the same axis scale, the minimum at $\nu = 0$ for $B_\perp = 4.5\,\mathrm{T}$ is approximately 3 times deeper than the one for $B_\perp = 4\,\mathrm{T}$.

The experiment in tilted magnetic fields shows that B_T can either suppress or strengthen the states at $\nu = 0$ and ± 1 depending on the tilt angle, meaning that we observe a transition between states with different spin polarization. In particular, the initial weakening of $\nu = 0$ with the external field indicates that, for low angles, the state is not spin-polarized. However, at higher angles, the state is strengthened by the external field B_T, compatibly with the presence of a net spin polarization of the state at $\nu = 0$.

However, the experimental data reported in Figure 4.5 show that the crossover between suppression and enhancement of $\nu = 0$, is not determined solely by B_T, but rather by a combined effect of $B_\perp$ and B_T. Indeed, for $B_\perp = 4\,\mathrm{T}$, $\nu = 0$ is re-enhanced already at $B_T = 26.7\,\mathrm{T}$, while for $B_\perp = 5\,\mathrm{T}$ an external field of $30\,\mathrm{T}$ is not enough to cause the strengthening of $\nu = 0$.

4.3.2 Energy gaps

So far, we have provided a qualitative description of the behaviour of $\nu = 0$ and ± 1 in a tilted magnetic field. More quantitative insights can be obtained from the extraction of the energy gaps Δ_ν at the three filling factors. As already illustrated in the case of $\nu = 2$ and $\nu = 6$ in Figure 4.2 (b), Δ_ν can be extracted from the jumps of the chemical potential at a specific filling factor ν. μ is calculated according to equation 4.1 only for the data showing $|\delta| < 5^\circ$. In addition, given the uncertainty on the surface of the device S, we calculate μ for both S_{min} and S_{max}. The value of the gaps reported in Figure 4.6 is an average of the values obtained using the two surface values and the error bars indicate the difference between the two calculated values.

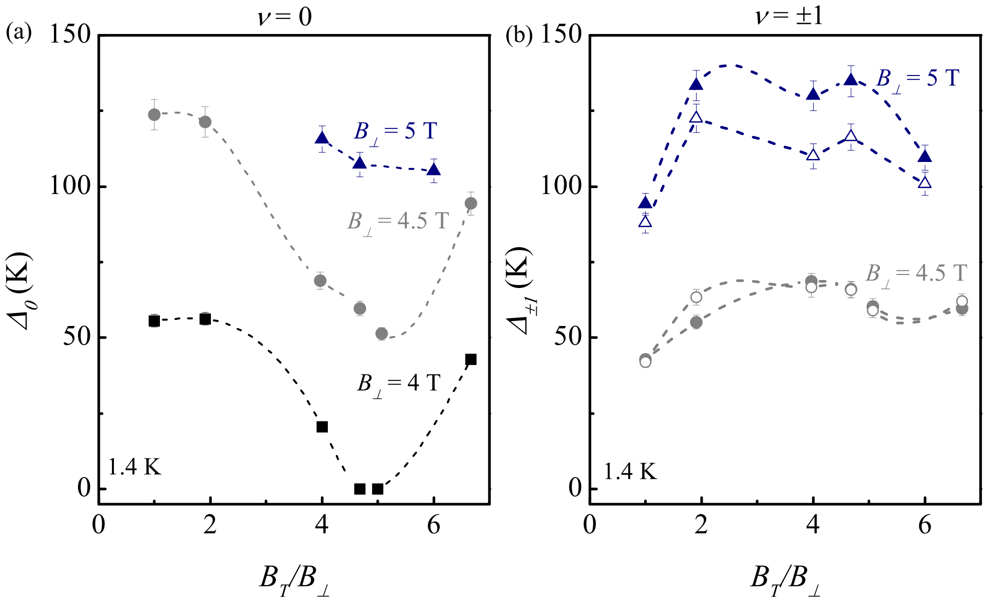

Figure 4.6: *Energy gaps for the states within $N = 0$ at 1.4 K as a function of the ratio $B_T/B_\perp$. (a): Energy gap for $\nu = 0$ at $B_\perp = 4$ T (black squares), $B_\perp = 4.5$ T (gray circles), and $B_\perp = 5$ T (blue triangles). (b): Energy gaps for $\nu = 1$ (solid symbols) and $\nu = -1$ (open symbols) at $B_\perp = 4.5$ T (gray circles), and $B_\perp = 5$ T (blue triangles). The dashed lines are a guide to the eye.*

In Figure 4.6 (a) we plot the value of Δ_0 as a function of the ratio $B_T/B_\perp$ for three different values of $B_\perp$. The reduction of the energy gap due to the total magnetic field can be clearly seen for $B_\perp = 4$ T and $B_\perp = 4.5$ T (black squares and gray circles). When $B_T/B_\perp > 2$ the size of Δ_0 strongly decreases reaching a minimum for $B_T/B_\perp \approx 5$. For $B_\perp = 4$ T the gap is completely suppressed. As B_T is further increased exceeding $6 \times B_\perp$, Δ_0 is strongly enhanced again.

Considering $\nu = \pm 1$, we notice that, after an initial increase observed up to $B_T/B_\perp = 2$, $\Delta_{\pm 1}$ does remains constant if B_T is further enhanced. This happens in the same field range where we observed the suppression of Δ_0. For $B_\perp = 5$ T, $\Delta_{\pm 1}$ decreases again as B_T reaches 30 T. Notice that tilting the sample, the loss angle for $\nu = 0$ diminishes (see figure 4.5 (c)) and its value falls below $|\delta| \leq 5°$. Therefore, the gaps values obtained for $B_T/B_\perp \geq 4$ and displayed in Figure 4.6 are reliable.

Figure 4.6 suggests that the interplay between B_T and $B_\perp$ is relevant for the development of the gaps, corroborating our previous statement. The size of the gaps scales with the ratio $B_T/B_\perp$ and is found to depend strongly on the perpendicular component of the field. Indeed, an increase of 0.5 T in a purely perpendicular field, leads to a doubled value of both Δ_0 and $\Delta_{\pm 1}$. In addition, even in the presence of the same $B_T = 30\,\mathrm{T}$, the gaps with the higher $B_\perp = 5\,\mathrm{T}$ are bigger than the ones for $B_\perp = 4.5\,\mathrm{T}$ (the points for the highest $B_T/B_\perp$ in both panels (a) and (b)).

The energy gaps presented in Figure 4.6 are measured at 1.4 K. An increase in temperature causes a strong decrease of the gap size. In Figure 4.7 we plot Δ_0 as a function of the temperature for $B_\perp = 4.5\,\mathrm{T}$. The different symbols indicate different B_T.

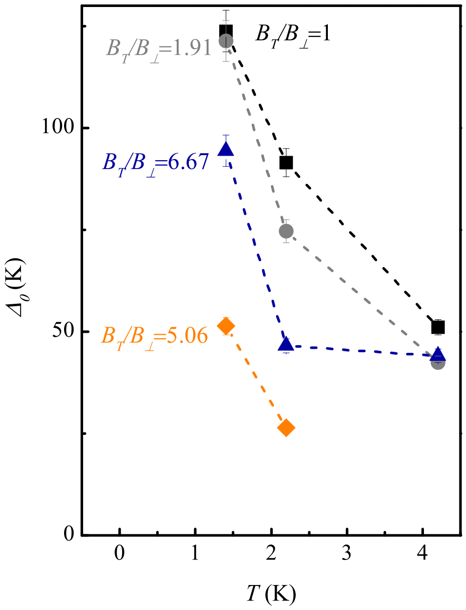

Figure 4.7: *Energy gap for $\nu = 0$ as a function of temperature for $B_\perp = 4.5\,T$. The different symbols indicate the different ratios $B_T/B_\perp = 1$ (black squares), $B_T/B_\perp = 1.91$ (gray circles), $B_T/B_\perp = 5.06$ (orange diamonds), and $B_T/B_\perp = 6.67$ (blue triangles). The dashed lines are a guide to the eye.*

The temperature affects dramatically the gap size for all different $B_T/B_\perp$ ratios.

The size of Δ_0 is strongly reduced by an increase in temperature between 1.4 and 4.2 T and the decrease occurs for every different B_T.
In a purely perpendicular field ($B_T/B_\perp = 1$, black symbols), the reduction of $\Delta = 0$ due to the temperature increment is comparable with the suppression of the state caused by the external magnetic field for $B_T = 5 \times B_\perp$. Such a strong influence of the temperature on Δ_0 indicates that electron-electron interactions play an important role in the origin of filling factor $\nu = 0$.

4.4 Discussion

The non-monotonic dependence of the Δ_0 on the external magnetic field indicates that the properties of the state at $\nu = 0$ change as the Zeeman energy is increased. In particular, the ground state observed in a purely perpendicular magnetic field is not spin-polarized, while the sudden increase of Δ_0 for high $B_T/B_\perp$ suggests the the final state retains spin polarization induced by the increased Zeeman energy.
In Figure 4.8 (a) we draw schematically a simple scenario for the splitting of the $N = 0$ Landau level indicating the two valley states by the different colours (red and green) and the two spin states by $\uparrow$ and $\downarrow$. In a purely perpendicular magnetic field ($B_T/B_\perp = 1$), the degeneracy of the $N = 0$ LL is lifted and we observe three states associated to the energy gaps Δ_0, Δ_1 and Δ_{-1}. At $\nu = 0$, two levels are occupied by electrons in the same valley (green lines) with opposite spin. The state at $\nu = 0$ is thus valley polarized and spin unpolarized. The filling factors ± 1 separate two states with opposite spins within the same valley.
As the sample is tilted (keeping $B_\perp$ constant), the ratio $B_T/B_\perp$ is increased and the energy of the states with opposite spins increases or decreases due to the Zeeman effect. For a specific value of $B_T/B_\perp$ marked by a $*$ in the figure, there is a crossing between two states having opposite spin and residing in different valleys. The crossing changes the spin and valley polarization of the states at $\nu = 0$ and $\nu = \pm 1$. Eventually, for high tilt angles and high values of $B_T/B_\perp$, $\nu = 0$ shows spin polarization while $\nu = \pm 1$ separate the states with the same spin within different valleys.
Such a simple model, which assumes a strict spin or valley polarization in a purely perpendicular field and a single particle Zeeman effect, can already describe qualitatively the behaviour of the gaps reported in Figure 4.6 and illustrated schematically in Figure 4.8 (b). Indeed, it depicts the decrease of the size of Δ_0 and the its successive enhancement. Moreover, it illustrates the initial increase of $\Delta_{\pm 1}$ and their successive weak dependence on B_T.

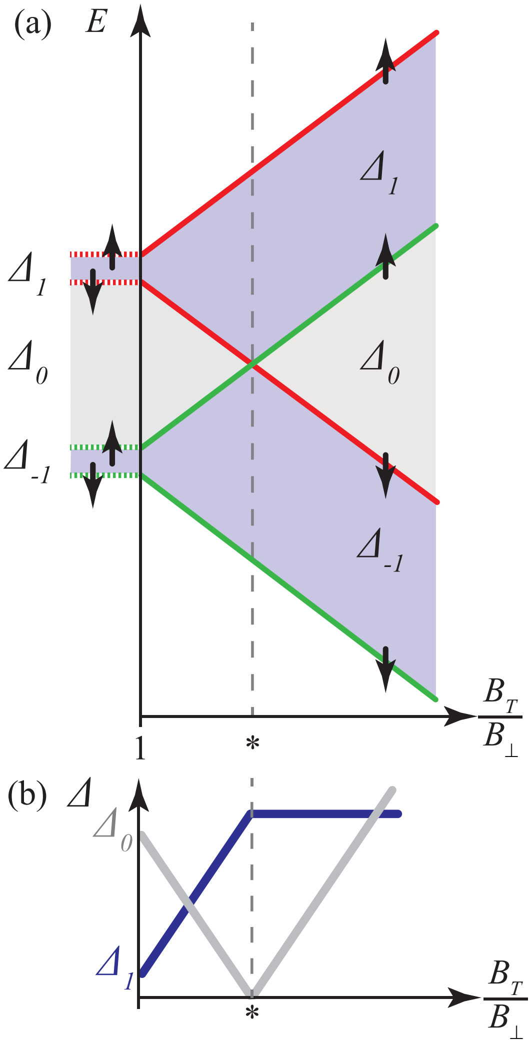

Figure 4.8: *(a) Splitting scenario for the $N = 0$ LL. Energy levels as a function of the ratio $B_T/B_\perp$. Each level is defined by a the valley state (red or green lines) and by a spin state (↑ or ↓). (b) Schematic representation of the behaviour of Δ_0 (gray line) and Δ_1 (blue line) as a function of $B_T/B_\perp$, as obtained from the model drawn in panel (a).*

We notice, however, that such a simple description involves always a complete suppression of Δ_0 for a certain value of $B_T/B_\perp$, due to the crossing of two levels. Our data for $B_\perp = 4.5\,\mathrm{T}$ and $B_\perp = 5\,\mathrm{T}$ (gray circles and blue triangles in Figure 4.8 (a)) clearly show that this is not the case. Δ_0 has a minimum for $B_T/B_\perp \approx 5$ but does not close completely. This observation suggests that the level crossing depicted in Figure 4.8 should be replaced by an anti-crossing, possibly due to electron-electron interactions leading to a hybridization of the two approaching levels. Such an anti-crossing could describe the finite value of Δ_0 observed experimentally.

Comparison with microscopic models

We now compare our experimental results with the proposed theoretical models which have addressed the splitting of the $N = 0$ and, in particular, the different ground states occurring at $\nu = 0$. From a microscopic point of view, four distinct orderings (the charge density wave, the Kekulé distortion, the ferromagnetic order and the canted antiferromagnetic phase) have been proposed for the $\nu = 0$ ground state, as mentioned in the introduction section of this Chapter. Figure 4.9 shows a schematic representation of these phases.

The CDW phase corresponds to the lifting of the valley degeneracy for $N = 0$. The electrons reside in one valley (and therefore on one sub-lattice) and have opposite spins.[10,11] In the KD type of ordering, the two valleys hybridize and can host both spin orientations.[14,15] Neither of these phases shows spin polarization, therefore they are possible candidates for the state at $\nu = 0$ in a purely perpendicular field.

The F phase is characterized by a spin polarized state at $\nu = 0$, having electrons with the same spin orientation occupying both valleys. In the CAF phase the states in different valleys have non-collinear spins with the same component along the direction of the external magnetic field and opposite in the direction perpendicular to it. The F and the CAF phases possess a net spin polarization and thus they both could explain the enhancement of the energy gap at high tilt angles.[12]

From the analysis of the size of Δ, we cannot distinguish between the the CDW and the KD ordering. Indeed, the gap size for both phases is set by the energy associated to the anisotropies due to electron-electron interactions and electron-phonon interactions at the lattice scale. As mentioned previously in section 2.3.4, they are predicted[11,30] to scale as

$$E_C \times (a/\ell_B) \approx B_\perp\,[\mathrm{T}]\mathrm{K}. \tag{4.2}$$

However, it was pointed out[12] that such anisotropies are renormalized by the Coulomb interactions, which leads to an enhancement of over an order of magnitude compared to the value reported in eq.4.2 for the range of B_T and $B_\perp$

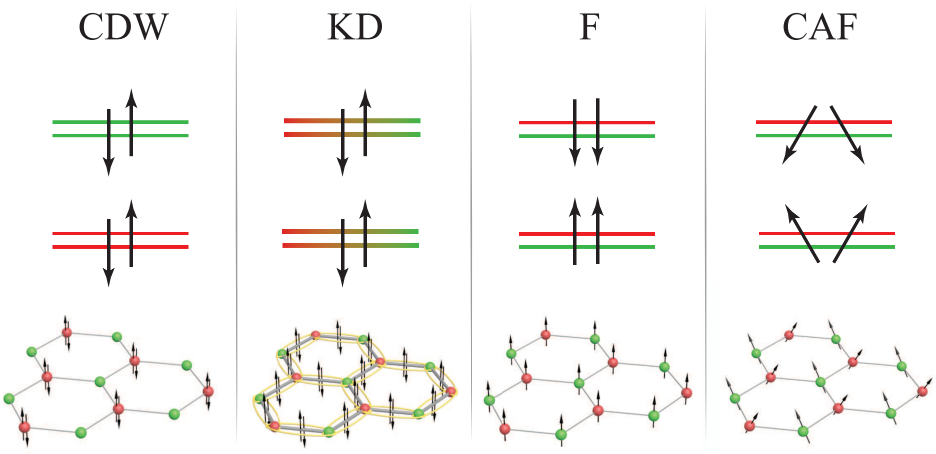

Figure 4.9: *The proposed ground states at* $\nu = 0$. *The two different valleys are depicted as green and red lines, the different spin states are depicted as up and down pointing arrows. In the* $N = 0$ *LL, the electrons residing in one valley can occupy only the lattice sites belonging to one sublattice. From left to right : The CDW ground state, defined by the occupation of one valley by the two spin orientations. The KD state, where the two spin orientations occupy a linear combination of the two valleys. The spin ferromagnet ground state, characterized by one spin orientation in both valleys. The CAF ordering, identified by the occupation of both valleys, each of them by a couple of spin canted with respect to the direction of the external field.*

considered in the experiment. This estimate is compatible with the value of Δ_0 obtained in a purely perpendicular field and reported in Figure 4.6.

Considering the proposed final states (F and CAF), they are both characterized by a gapped bulk but present different properties at the edge. The F phase shows metallic edges, while the edges in the CAF phase are gapped. Our capacitance measurements, sensitive to the bulk density of states, cannot distinguish between the two states.[10,12,17]

It is predicted that enhancing the Zeeman energy will eventually force the system into the F phase and therefore, a phase transition is expected to occur between the original state for $B_T = B_\perp$ (CDW or KD) to the final ferromagnetic one.[10,12] Referring to the phase diagram elaborated by Kharitonov,[12] only two phase transitions are expected as a function of the Zeeman energy. If the system is in the CDW ordering, the Zeeman energy enhancement induce a first order phase transition to the F phase. In case the system is in the KD phase, it undergoes a first order transition to the CAF phase and, if the external field if further increased, it will end up in the F phase after a second order transition. Therefore, probing the nature of the final state can help one to assess the properties of the original ground state. To this end, a combination of different experimental techniques is required. The bulk sensitive capacitance should be complemented by transport measurements, which are sensitive to the edge states and allow one to distinguish between the CAF and the F phase.[17] In addition, information about the valley polarization of the specific states can be obtained by optical spectroscopy,[16] which can integrate the information about the spin polarization obtained in the tilted field measurements.

4.5 Conclusions

We measured the capacitance of a graphene based capacitor in a tilted magnetic field up to high tilt angles ($\theta = 81.4°$). We characterized the sample at low temperature and calculated the DOS of the system in zero field and at 1 T. We introduced an empirical criterion over the magnitude of $|\delta|$ in order to discriminate when a conversion of the data into DOS and chemical potential is reliable.

We observed the splitting of the $N = 0$ Landau level induced by the external perpendicular magnetic field. In a tilted magnetic field, we reported a re-entrant behaviour of the minimum corresponding to $\nu = 0$, which is suppressed by the initial increase of B_T and it gets successively enhanced for the hight tilt angles. The gap Δ_0 is found to scale with $B_T/B_\perp$ having a minimum for $B_T/B_\perp \approx 5$ and a steep increase for $B_T/B_\perp > 6$. The size of the energy gap is bigger than the Zeeman energy and it is strongly affected by the temperature. The gaps at $\nu = \pm 1$ show an initial increase as a function of B_T followed by a stabilization of the value.

The behaviour of the gaps at the three filling factors resulting from the splitting of the $N = 0$ LL can be qualitatively explained assuming a valley polarized and spin unpolarized state at $\nu = 0$ which evolves, owing to the enhancement of the Zeeman effect, into a spin polarized one. However, in order to have a conclusive evidence about the microscopic ordering occurring at $\nu = 0$, our capacitance traces, sensitive to changes in the bulk states, should be complemented by transport data, sensitive to the edge states, in a tilted magnetic field or by optical spectroscopy sensitive to the valley polarization.

As a concluding remark, we notice that the initial state for $\nu = 0$ in a purely perpendicular magnetic field (either CWD or KD) is different from the one (CAF) reported in Ref. 17. The electrostatic environment around the graphene might have an influence on the ground state selection at $\nu = 0$ and favour energetically one of the mentioned phases over the others.[10] Indeed, in our experiment, we employed encapsulated graphene while Young and collaborators used devices presenting hBN only as a substrate.[17]

References

[1] Y. Zhang, Z. Jiang, J. P. Small, M. S. Purewal, Y. W. Tan, M. Fazlollahi, J. D. Chudow, J. A. Jaszczak, H. L. Stormer, and P. Kim, "Landau-level splitting in graphene in high magnetic fields", *Physical Review Letters* **96**, 13, 136806 (2006).

[2] Z. Jiang, Y. Zhang, H. L. Stormer, and P. Kim, "Quantum hall states near the charge-neutral dirac point in graphene", *Physical Review Letters* **99**, 10, 106802 (2007).

[3] J. G. Checkelsky, L. Li, and N. P. Ong, "Divergent resistance at the Dirac point in graphene: Evidence for a transition in a high magnetic field", *Physical Review B* **79**, 11, 115434 (2009).

[4] X. Du, I. Skachko, F. Duerr, A. Luican, and E. Y. Andrei, "Fractional quantum Hall effect and insulating phase of Dirac electrons in graphene", *Nature* **462**, 7270, 192–5 (2009).

[5] L. Zhang, Y. Zhang, M. Khodas, T. Valla, and I. A. Zaliznyak, "Metal to Insulator Transition on the N Âij 0 Landau Level in Graphene", *Physical Review Letters* **046804**, JULY, 1–4 (2010).

[6] F. Amet, J. R. Williams, K. Watanabe, T. Taniguchi, and D. Goldhaber-Gordon, "Insulating behavior at the neutrality point in single-layer graphene", *Physical Review Letters* **110**, 21, 216601 (2013).

[7] Y. Zhao, P. Cadden-Zimansky, F. Ghahari, and P. Kim, "Magnetoresistance measurements of graphene at the charge neutrality point", *Physical Review Letters* **108**, 10, 106804 (2012).

[8] A. F. Young, C. R. Dean, L. Wang, H. Ren, P. Cadden-Zimansky, K. Watanabe, T. Taniguchi, J. Hone, K. L. Shepard, and P. Kim, "Spin and valley quantum Hall ferromagnetism in graphene", *Nature Physics* **8**, 7, 550–556 (2012).

[9] K. Nomura and A. H. MacDonald, "Quantum hall ferromagnetism in graphene", *Physical Review Letters* **96**, 25, 256602 (2006).

[10] J. Jung and A. H. MacDonald, "Theory of the magnetic-field-induced insulator in neutral graphene sheets", *Physical Review B* **80**, 23, 235417 (2009).

[11] J. Alicea and M. P. A. Fisher, "Graphene integer quantum Hall effect in the ferromagnetic and paramagnetic regimes", *Physical Review B* **74**, 7, 75422 (2006).

[12] M. Kharitonov, “Phase diagram for the ν=0 quantum Hall state in monolayer graphene”, *Physical Review B* **85**, 15, 155439 (2012).

[13] M. Kharitonov, “Edge excitations of the canted antiferromagnetic phase of the $\nu = 0$ quantum Hall state in graphene: A simplified analysis”, *Physical Review B* **86**, 7, 075450 (2012).

[14] K. Nomura, S. Ryu, and D. H. Lee, “Field-Induced kosterlitz-Thouless transition in the N=0 landau level of graphene”, *Physical Review Letters* **103**, 21, 216801 (2009).

[15] M. O. Goerbig, “Electronic properties of graphene in a strong magnetic field”, *Reviews of Modern Physics* **83**, 4, 1193–1243 (2011).

[16] L. Z. Tan, M. Orlita, M. Potemski, J. Palmer, C. Berger, W. A. de Heer, S. G. Louie, and G. Martinez, “SU(4) symmetry breaking revealed by magneto-optical spectroscopy in epitaxial graphene”, *Physical Review B* **91**, 23, 235122 (2015).

[17] A. F. Young, J. D. Sanchez-Yamagishi, B. Hunt, S. H. Choi, K. Watanabe, T. Taniguchi, R. C. Ashoori, and P. Jarillo-Herrero, “Tunable symmetry breaking and helical edge transport in a graphene quantum spin Hall state.”, *Nature* **505**, 7484, 528–32 (2014).

[18] F. Chiappini, S. Wiedmann, K. Novoselov, A. Mishchenko, A. K. Geim, J. C. Maan, and U. Zeitler, “Lifting of the Landau level degeneracy in graphene devices in a tilted magnetic field”, *Physical Review B* **92**, 20, 201412 (2015).

[19] S. J. Haigh, A. Gholinia, R. Jalil, S. Romani, L. Britnell, D. C. Elias, K. S. Novoselov, L. A. Ponomarenko, A. K. Geim, and R. Gorbachev, “Cross-sectional imaging of individual layers and buried interfaces of graphene-based heterostructures and superlattices”, *Nature Materials* **11**, 9, 764–767 (2012).

[20] L. A. Ponomarenko, R. Yang, T. M. Mohiuddin, M. I. Katsnelson, K. S. Novoselov, S. V. Morozov, A. A. Zhukov, F. Schedin, E. W. Hill, and A. K. Geim, “Effect of a high-κ environment on charge carrier mobility in graphene”, *Physical Review Letters* **102**, 20, 206603 (2009).

[21] G. L. Yu, R. Jalil, B. Belle, A. S. Mayorov, P. Blake, F. Schedin, S. V. Morozov, L. a. Ponomarenko, F. Chiappini, S. Wiedmann, U. Zeitler, M. I. Katsnelson, A. K. Geim, K. S. Novoselov, and D. C. Elias, “Interaction

phenomena in graphene seen through quantum capacitance.", *Proceedings of the National Academy of Sciences of the United States of America* **110**, 9, 3282–6 (2013).

[22] J. Xia, F. Chen, J. Li, and N. Tao, "Measurement of the quantum capacitance of graphene.", *Nature Nanotechnology* **4**, 8, 505–9 (2009).

[23] A. F. Young, C. R. Dean, I. Meric, S. Sorgenfrei, H. Ren, K. Watanabe, T. Taniguchi, J. Hone, K. L. Shepard, and P. Kim, "Electronic compressibility of layer-polarized bilayer graphene", *Physical Review B* **85**, 23, 235458 (2012).

[24] K. K. Kim, A. Hsu, X. Jia, S. M. Kim, Y. Shi, M. Dresselhaus, T. Palacios, and J. Kong, "Synthesis and characterization of hexagonal boron nitride film as a dielectric layer for graphene devices", *ACS Nano* **6**, 10, 8583–8590 (2012).

[25] S. Adam, E. H. Hwang, V. M. Galitski, and S. Das Sarma, "A self-consistent theory for graphene transport.", *Proceedings of the National Academy of Sciences of the United States of America* **104**, 47, 18392–7 (2007).

[26] E. V. Kurganova, S. Wiedmann, A. J. M. Giesbers, R. V. Gorbachev, K. S. Novoselov, M. I. Katsnelson, T. Tudorovskiy, J. C. Maan, and U. Zeitler, "Quantized coexisting electrons and holes in graphene measured using temperature-dependent magnetotransport", *Physical Review B* **87**, 8, 085447 (2013).

[27] K. S. Novoselov, A. K. Geim, S. V. Morozov, D. Jiang, M. I. Katsnelson, I. V. Grigorieva, S. V. Dubonos, and A. A. Firsov, "Two-dimensional gas of massless Dirac fermions in graphene", *Nature* **438**, 7065, 197–200 (2005).

[28] Y. Zhang, Y.-W. Tan, H. L. Stormer, and P. Kim, "Experimental observation of the quantum Hall effect and Berry's phase in graphene", *Nature* **438**, 7065, 201–204 (2005).

[29] G. Li, A. Luican, and E. Y. Andrei, "Scanning tunneling spectroscopy of graphene on graphite", *Physical Review Letters* **102**, 17, 176804 (2009).

[30] M. O. Goerbig, R. Moessner, and B. Douçot, "Electron interactions in graphene in a strong magnetic field", *Physical Review B* **74**, 16, 161407 (2006).

CHAPTER 5

Magnetotransport in single layer graphene in a high parallel magnetic field

---

Abstract

Graphene on hexagonal boron nitride is an atomically flat conducting system that is ideally suited for probing the effect of Zeeman splitting on electron transport. In this Chapter, we demonstrate by magneto-transport measurements that a parallel magnetic field up to 30 Tesla does not affect the transport properties of graphene on hBN even at charge neutrality where such an effect is expected to be maximal. The only magnetoresistance detected at low carrier concentrations is shown to be associated with a small perpendicular component of the field which cannot be fully eliminated in the experiment. Despite the high mobility of charge carries at low temperatures, we argue that the effects of Zeeman splitting are fully masked by electrostatic potential fluctuations at charge neutrality.

Part of this work has been adapted from: F. Chiappini, S. Wiedmann *et al.*,"Magnetotransport in single-layer graphene in a large parallel magnetic field", Phys. Rev. B **94**, 085302 (2016).

5.1 Introduction

A magnetic field applied in the plane of an ideally flat two-dimensional (2D) conductor couples to the spin degree of freedom of charge carriers rather than to their orbital motion. Therefore, in case of absent spin-orbit coupling, the in-plane magnetic field does not influence the motion of the carriers. In such a setup, the orbital related effects caused by the Lorentz force, such as the Hall effect, are suppressed and the spin-polarization effects become the leading phenomenon. This idea has been exploited in semiconductor heterostructures to study the influence of electron-electron interactions on the spin polarisation and on the spin-resolved density of states in two-dimensional electron gases (2DEGs).[1,2]

For some 2DEGs, the characteristic width of the confinement potential is, however, comparable to the magnetic length $\ell_B = \sqrt{\hbar/eB}$ even for fields of the order of a few Tesla. For these quasi-2D systems, the parallel magnetic field affects the motion of the carriers, as specified in section 2.6. Therefore, the energy bands and, consequently, the effective mass and the g-factor of electrons become sensitive to the value of the in-plane magnetic field $B_{\|}$[3,4] and the interplay between spin and orbital effects influences the transport properties of the system.[5,6]

A complete decoupling of the orbital and spin effects can be achieved in graphene. As already described in section 2.6, the spin orbit-coupling for graphene is negligible and, since graphene is only one atom thick, the orbital motion of the electrons is not affected by $B_{\|}$ up to the fields of the order of 10^3 T. In actual devices, however, graphene adapts to the conformation of the underlying substrate.[7] Common substrates such as SiO_2 induce corrugations (ripples) to graphene plane that convert a nominal in-plane field into a randomly oriented one, depending on the curvature of the surface. Experimental works on SiO_2 supported graphene showed that the external $B_{\|}$ couples to the orbital motion of carriers via the high corrugations leading to a magnetoresistance which depends on the topography of the device.[8,9]

Nevertheless, an atomically flat conducting system can be achieved by placing graphene on hexagonal boron-nitride (hBN).[10,11] As described in Chapter 2, graphene sandwiched between two atomically flat hBN surfaces gives rise to an ultimately sharp potential well with a characteristic width of one atom,[12] representing an ideal playground to probe the effects of an in-plane magnetic field on the electron transport of a truly 2D system.

An in-plane magnetic field modifies the density of states of flat graphene only due to the Zeeman splitting $E_Z = g\mu_B B$, where $g = 2$ is the electron g-factor and μ_B is the Bohr magneton, leading to a value $E_Z \approx 3.5\,\text{meV}$ at $B = 30\,\text{T}$.

One can calculate the charge carrier density n of graphene in the presence of finite Zeeman splitting as

$$n = n_+^h + n_-^h - n_+^e - n_-^e. \tag{5.1}$$

Here, n_σ^e and n_σ^h are the electron and hole densities for different spin species $\sigma = \pm$ given by

$$n_\sigma^{e,h} = \int_0^\infty DOS(E) f_\sigma^{e,h}(E)\, dE \tag{5.2}$$

where $f_\sigma^e(E) = [1 + \exp[(E - \sigma E_Z/2 - \mu)/(k_B T)]]^{-1}$ is the electron Fermi distribution function, $f_\sigma^h(E) = 1 - f_\sigma^e(-E)$, μ is the chemical potential, k_B is the Boltzmann constant, and $DOS(E) = DOS(-E)$ is density of states per spin which is taken to be symmetric with respect to the Dirac point. For ideally clean graphene in zero field $DOS(E) = |E|/\pi\hbar^2 v_F^2$ (see section 2.1.1). At the charge neutrality point (CNP) $n = 0$.

The splitting of the spin sub-bands due to the Zeeman effect makes the DOS of graphene finite even at the CNP leading to a non-zero quasiparticle density n_Q defined as

$$n_\mathrm{Q} = n_+^e + n_-^e + n_+^h + n_-^h. \tag{5.3}$$

Therefore, a strong in-plane magnetic field is expected to affect magneto-transport properties of graphene only in the limit of low charge carrier density, $n < n_\mathrm{Q}$, and low temperature, $T < E_Z$.[13]

In this Chapter, we investigate the resistivity of high-quality hBN supported graphene in the presence of a large in plane magnetic field. We do not observe any change of resistivity induced by $B_\parallel$ neither at charge neutrality nor for large doping at 1.4 K and for $B_\parallel$ as large as 30 T. Despite the high mobility of charge carriers in the sample $\mu_n \approx 50000\,\mathrm{cm^2V^{-1}s^{-1}}$, the electrostatic potential fluctuations around the charge neutrality point (CNP) are sufficiently strong to average out possible effects of Zeeman splitting.

5.2 Experimental details

Our sample is a Hall-bar shaped graphene device with an aspect ratio $L/W = 2$ (the distance between contacts $L \approx 3\,\mu$m and the width $W \approx 1.5\,\mu$m), similar to the one described in section 2.2 and depicted in Figure 2.3. The graphene flake, sandwiched between two thin layers of hBN, is connected to Ti/Au contacts. The system is placed on top of a doped Si/SiO$_2$ wafer, which acts as a back gate. Low temperature ($T = 1.4$ K) transport measurements were performed using a low frequency lock-in technique with a 10 nA excitation. The longitudinal ρ_{xx}

and Hall ρ_{xy} resistivities were measured as a function of the back gate voltage V_G and the external magnetic field B that varies up to 30 T.

The charge neutrality point is associated with the maximum of ρ_{xx} at $V_\mathrm{G} = -10.5\,\mathrm{V}$, irrespective of the value of magnetic field (see Figure 5.1(a)). The charge carrier concentration n is assumed to be proportional to the gate voltage $n = \alpha\,(V_\mathrm{G} - V_\mathrm{CNP})$, where the proportionality coefficient is set by $\alpha = 4.7 \times 10^{14}\,\mathrm{m}^{-2}\mathrm{V}^{-1}$. The value of α is obtained experimentally from the dependence of Shubnikov-de-Haas oscillations on V_G for a given perpendicular component of the field $B_\perp$.

As described in Section 2.2, a linear fit of the conductivity at large n, $\sigma_{xx} = e\mu_n|n|$, gives rise to an estimate of mobility of carriers. In our case we obtain for the mobility of the holes in our system $\mu_n \approx 50000\,\mathrm{cm}^2\mathrm{V}^{-1}\mathrm{s}^{-1}$. In what follows we focus mostly on the hole-doped region $V_\mathrm{G} < V_\mathrm{CNP}$ since the hole mobility in the sample appears to be higher than the electron one. The high quality of our sample is testified by the observation of the fully developed integer quantum Hall effect at $B_\perp = 2.5\,\mathrm{T}$ and the observation of the lifting of the spin degeneracy of the Landau levels at $B_\perp = 10\,\mathrm{T}$, as described in Chapter 3.

The sample is mounted on a platform that allows us to rotate the sample with respect to direction of the external magnetic field B_T. We define θ as the angle between the direction of external magnetic field and the normal to the graphene plane as shown in Figure 2.13. For $\theta = 90^\circ$ the field is entirely in plane, $B_\perp = B_T \cos\theta = 0$.

The angle θ is estimated from the measurement of Hall resistivity by using the expression $\rho_{xy} = B_T \cos\theta (en)^{-1}$ which holds for sufficiently large n in the single-component classical Hall regime. With our experimental setup we achieve $\theta = 90^\circ$ within less than 0.1°, which corresponds to $B_\parallel \approx B_T$ and $B_\perp \lesssim 50\,\mathrm{mT}$ at the maximal applied field $B_T = 30\,\mathrm{T}$.

5.3 Magnetotransport in a parallel magnetic field

Figure 5.1 (a) shows the resistivity ρ_{xx} as a function of the gate voltage V_G for the best parallel-field configuration with $\theta = 89.91^\circ$. The grey curve represents the signal in the absence of the field while the black curve corresponds to the external field $B_T = 30\,\mathrm{T}$. Away from the CNP the two traces are indistinguishable. A small increase in resistivity is observed in the region around the CNP (see inset of Figure 5.1(a)) at maximum field.

To illustrate the response of ρ_{xx} to B_T better, we plot in Figure 5.1(b) the magnetoresistance (defined as $\rho_{xx}(B_T) - \rho_{xx}(0)$) as a function of the magnetic field in the best parallel-field configuration for specific gate voltage values indi-

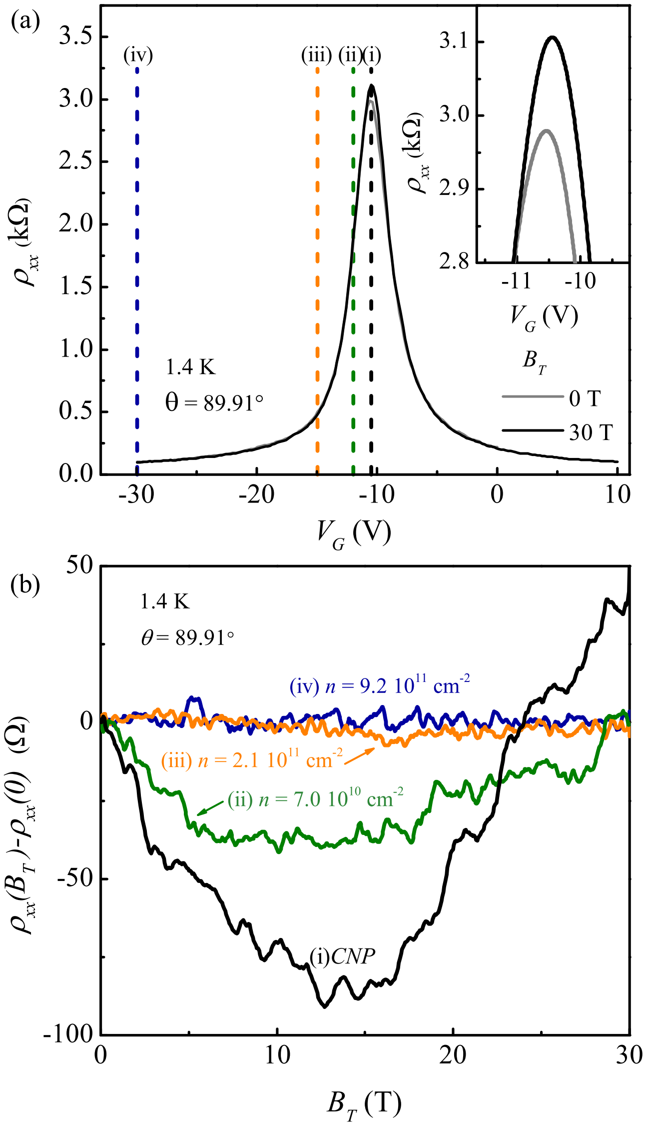

Figure 5.1: *Panel (a): Resistivity ρ_{xx} versus gate voltage V_G for $B_T = 0$ (grey solid line) and $B_T = 30$ T (black line). Inset: Resistivity ρ_{xx} versus V_G in the vicinity of the CNP. Panel (b): Magnetoresistance as a function of B_T in the best parallel-field configuration, $\theta = 89.91° \pm 0.01°$. Different lines are for different concentrations of charge carriers: corresponding gate voltages are indicated with the dashed lines in panel (a).*

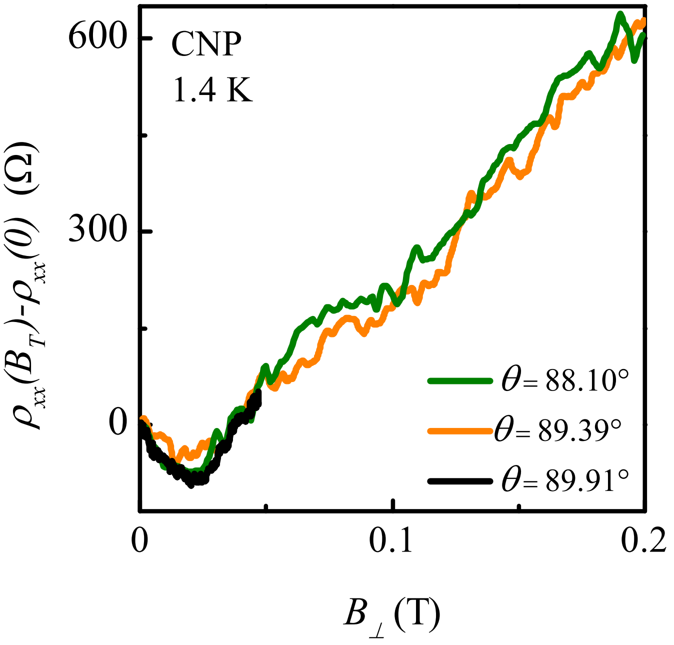

Figure 5.2: *Magnetoresistance at the CNP as a function of $B_\perp$ at 1.4 K for three different angles θ.*

cated by the dashed lines in Fig. 5.1a, corresponding to the CNP $n = 0$ (black line), $n = 7 \times 10^{10}\,\mathrm{cm}^{-2}$ (green line), $n = 2.1 \times 10^{11}\,\mathrm{cm}^{-2}$ (orange line) and $n = 9.2 \times 10^{11}\,\mathrm{cm}^{-2}$ (blue line).

At high n (blue and orange curves) the resistivity is not sensitive to $B_T \approx B_\parallel$ while a dependence $\rho_{xx}(B_T)$ is seen in a vicinity of the CNP (green and black lines).

One can clearly see that the observed magnetoresistance is maximized at the CNP. It reaches a maximal negative value for $B_T \approx 15\,\mathrm{T}$ and it increases for larger fields. Eventually it changes sign at $B_T \approx 25\,\mathrm{T}$. A similar non-monotonic behaviour can also be seen for $n = 7 \times 10^{10}\ \mathrm{cm}^{-2}$ (green line), though ρ_{xx} reaches its zero field value at $B_T \approx 30\,\mathrm{T}$.

However, this seemingly non-trivial magnetoresistance is induced entirely by the remaining perpendicular component of the field $B_\perp$, which cannot be ignored in the vicinity of the CNP.

In order to prove that the observed changes of ρ_{xx} are indeed related to $B_\perp$, we measure the magnetoresistance for slightly different tilt angles around $\theta = 90°$. In Fig. 5.2 we plot the data for three different angles: $\theta = 83.39°$, $\theta = 88.1°$ and $\theta = 89.91°$. The curves fall on top of each other when plotted with respect to

$B_\perp = B_T \cos\theta$. These experimental results suggest that the magnetoresistance observed in the vicinity of the CNP for $\theta \approx 90°$ is entirely due to the perpendicular component of the field and that $B_\parallel$ does not produce any sizeable effect in the resistivity of our device.

5.4 Discussion

The observed dependence $\rho_{xx}(B_\perp)$ at the CNP can be explained as follows. The initial decrease in resistance is compatible with the suppression of weak localization[14] due to external magnetic field. This phenomenon can be expected at such a low temperature and small $B_\perp$.[15]

The increase of ρ_{xx} for larger values of $B_\perp$ can be associated with a purely classical effect of two-liquid transport (see e. g. Refs. 16, 17 and references therein). This would also explain why such an effect quickly disappears away from the CNP.

Let us now discuss the experimental results from the point of view of a simple Drude theory which does not take into account localisation phenomena.[18] Assuming equal mobilities of electron- and hole-like quasiparticles, one obtains the resistivity tensor

$$\rho_{xx} = \frac{n_\mathrm{Q}}{e\mu_n} \frac{1 + \mu_n^2 B_\perp^2}{n_\mathrm{Q}^2 + n^2 \mu_n^2 B_\perp^2}, \quad \rho_{xy} = \frac{n}{n_\mathrm{Q}} \mu_n B_\perp \rho_{xx}, \tag{5.4}$$

where the quasiparticle density n_Q and the charge carrier density n are defined in equations 5.3 and 5.1, respectively.

At large doping ($n = \pm n_\mathrm{Q}$), one finds $\rho_{xx} = 1/e\mu_n|n|$, which lacks an explicit dependence on $B_\perp$. At the CNP ($n = 0$), one finds $\rho_{xx} = (e\mu_n n_\mathrm{Q})^{-1}(1+\mu_n^2 B_\perp^2)$ which manifestly increases with $B_\perp$. The quadratic dependence on $B_\perp$ in the homogeneous Drude model is transformed into a linear one (which is clearly seen in Fig. 5.2) due to the boundary effects or large-scale electrostatic potentials variations.[17,19] The detailed analysis of this phenomenon is, however, beyond the scope of the present work.

The transport properties at the CNP are governed by the quasi-particle density n_Q, which, in the case of pristine graphene without the Zeeman splitting, is $n_\mathrm{Q} = n = 0$. In an actual device, however, when the gate voltage is swept across the charge neutrality region, the quasiparticle density saturates around a finite value n_Q^* which is the minimum quasiparticle density that can be achieved experimentally. The most obvious reason for a finite value of the density of states in the vicinity of the Dirac point is the electrostatic potential variation induced e. g. by charged (or Coulomb) impurities.[20,21]

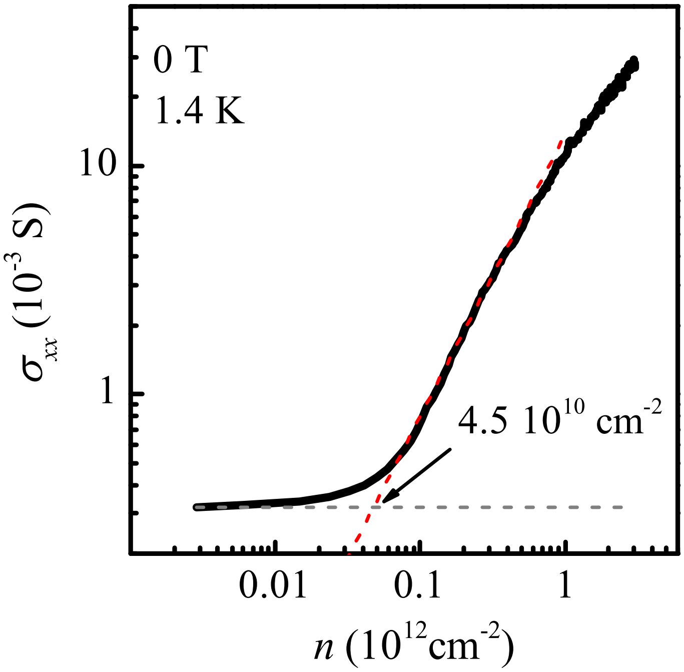

Figure 5.3: *Longitudinal conductivity $\sigma_{xx} = 1/\rho_{xx}$ as a function of charge carrier density n for $T = 1.4\,K$ and $B_T = 0$ for hole doping. The red dashed line represents a linear fit to $\log(\sigma_{xx})$. The intercept of the linear fit with the value of the residual conductivity (horizontal gray dashed line) indicate the residual quasiparticle density n^*_{Q} due to electrostatic potential fluctuations.*

An estimate of n^*_{Q} can be obtained from the measurement of the conductivity σ_{xx} of the device in zero magnetic field.[22] In Figure 5.3 we show σ_{xx} as a function of the charge carried density n at 0 T and 1.4 K. Around the CNP the conductivity saturates at the value $\sigma_{xx} = 3.2 \times 10^{-4}$ S, which is indicated by the horizontal dashed line. The intersection of this dashed lines with the linear fit to $\log(\sigma_{xx})$ provides us with an estimate for the minimal quasiparticle density $n^*_{\mathrm{Q}} = 4.5 \times 10^{10}\,\mathrm{cm}^{-2}$ at the CNP.

We find this value to be much larger than what is expected in the case of thermally excited quasiparticles in clean graphene. If we consider the density of state $DOS(E)$, from equation 5.2 at finite temperature and zero magnetic field we obtain $n_{\mathrm{Q}}(n = 0) = \pi T^2/3\hbar^2 v_F^2$. For $T = 1.4\,\mathrm{K}$ this amounts to $n_{\mathrm{Q}}(n = 0) = 3.5 \times 10^6\,\mathrm{cm}^{-2}$. This value is four orders of magnitude smaller than n^*_{Q}, meaning that the realistic density of states $DOS(E)$ at the CNP is much larger than the one for ideal graphene and that the origin of the large quasiparticle density is intrinsic of the device.

The Zeeman effect provides a competing mechanism which induces a finite density of states at the CNP. For ideal graphene at zero temperature one finds from equation 5.2 that $n_{\mathrm{Q}}(n = 0) = E_Z^2/4\pi\hbar^2 v_F^2$. For a field of 30 T this estimate gives the figure $n_{\mathrm{Q}}(n{=}0) = 2.2 \times 10^8\,\mathrm{cm}^{-2}$ which is, however, still two orders of magnitude smaller than n_{Q}^*. Despite the low temperature and the large $B_{\|}$ employed in the experiment such that $T \ll E_Z$, the Zeeman splitting is most likely masked by the potential fluctuations around the CNP and therefore cannot be detected in our experiment.

Owing to the development in the device fabrication technique, it is nowadays possible to achieve the quasiparticle density in graphene to be as low as $10^8\,\mathrm{cm}^{-2}$.[23] We may, therefore, expect that new experiments will soon be able to address the spin physics of graphene in a parallel magnetic field.

5.5 Conclusions

In conclusion, we measured the resistivity of graphene on hBN in a parallel magnetic field. At high charge carrier concentrations we do not observe any dependence of ρ_{xx} on the external magnetic field and we demonstrated that all the changes observed at low n and at the CNP can be ascribed to $B_{\perp}$. This indicates that the large parallel magnetic field up to 30 T and, consequently, Zeeman splitting up to 3.5 meV do not have any effect on the transport properties despite the rather high mobility $\mu_n \approx 50000\,\mathrm{cm}^2\mathrm{V}^{-1}\mathrm{s}^{-1}$ in the sample. This observation is compatible with the leading role of Coulomb impurities in graphene that induce sizeable smooth variations of electrostatic potential at charge neutrality without reducing the mobility of charge carriers.[24] We conclude that the presence of a smooth electrostatic potential variation in the sample fully masks the effects of Zeeman splitting in our samples.

References

[1] E. Tutuc, S. Melinte, and M. Shayegan, “Spin Polarization and g Factor of a Dilute GaAs Two-Dimensional Electron System”, *Physical Review Letters* **88**, 3, 36805 (2002).

[2] T. Okamoto, K. Hosoya, S. Kawaji, and A. Yagi, “Spin Degree of Freedom in a Two-Dimensional Electron Liquid”, *Physical Review Letters* **82**, 19, 3875–3878 (1999).

[3] S. Das Sarma and E. H. Hwang, “Parallel magnetic field induced giant magnetoresistance in low density quasi-two-dimensional layers”, *Physical Review Letters* **84**, 24, 5596–5599 (2000).

[4] X. Zhou, B. A. Piot, M. Bonin, L. W. Engel, S. Das Sarma, G. Gervais, L. N. Pfeiffer, and K. W. West, “Colossal magnetoresistance in an ultra-clean weakly interacting 2D fermi liquid”, *Physical Review Letters* **104**, 21, 216801 (2010).

[5] B. A. Piot, D. K. Maude, U. Gennser, A. Cavanna, and D. Mailly, “Interplay among spin, orbital effects, and localization in a GaAs two-dimensional electron gas in a strong in-plane magnetic field”, *Physical Review B* **80**, 11, 115337 (2009).

[6] E. Tutuc, S. Melinte, E. De Poortere, M. Shayegan, and R. Winkler, “Role of finite layer thickness in spin polarization of GaAs two-dimensional electrons in strong parallel magnetic fields”, *Physical Review B* **67**, 24, 241309 (2003).

[7] C. H. Lui, L. Liu, K. F. Mak, G. W. Flynn, and T. F. Heinz, “Ultraflat graphene.”, *Nature* **462**, 7271, 339–341 (2009).

[8] M. B. Lundeberg and J. A. Folk, “Rippled graphene in an in-plane magnetic field: Effects of a random vector potential”, *Physical Review Letters* **105**, 14, 146804 (2010).

[9] J. Wakabayashi and T. Sano, “Magnetoresistance of Rippled Graphene in a Parallel Magnetic Field”, *Journal of Physics: Conference Series* **334**, 1, 012039 (2011).

[10] C. R. Dean, a. F. Young, I. Meric, C. Lee, L. Wang, S. Sorgenfrei, K. Watanabe, T. Taniguchi, P. Kim, K. L. Shepard, and J. Hone, “Boron nitride substrates for high-quality graphene electronics”, *Nature Nanotechnology* **5**, 10, 722–726 (2010).

[11] J. M. Xue, J. Sanchez-Yamagishi, D. Bulmash, P. Jacquod, a. Deshpande, K. Watanabe, T. Taniguchi, P. Jarillo-Herrero, and B. J. Leroy, “Scanning tunnelling microscopy and spectroscopy of ultra-flat graphene on hexagonal boron nitride”, *Nature Materials* **10**, 4, 282–285 (2011).

[12] S. J. Haigh, A. Gholinia, R. Jalil, S. Romani, L. Britnell, D. C. Elias, K. S. Novoselov, L. A. Ponomarenko, A. K. Geim, and R. Gorbachev, “Cross-sectional imaging of individual layers and buried interfaces of graphene-based heterostructures and superlattices”, *Nature Materials* **11**, 9, 764–767 (2012).

[13] E. H. Hwang and S. Das Sarma, “Graphene magnetoresistance in a parallel magnetic field: Spin polarization effect”, *Physical Review B* **80**, 7, 75417 (2009).

[14] P. M. Ostrovsky, I. V. Gornyi, and A. D. Mirlin, “Electron transport in disordered graphene”, *Physical Review B* **74**, 23, 235443 (2006).

[15] F. V. Tikhonenko, D. W. Horsell, R. V. Gorbachev, and A. K. Savchenko, “Weak localization in graphene flakes”, *Physical Review Letters* **100**, 5, 056802 (2008).

[16] S. Wiedmann, H. J. van Elferen, E. V. Kurganova, M. I. Katsnelson, A. J. M. Giesbers, A. Veligura, B. J. van Wees, R. V. Gorbachev, K. S. Novoselov, J. C. Maan, and U. Zeitler, “Coexistence of electron and hole transport in graphene”, *Physical Review B* **84**, 11, 115314 (2011).

[17] P. S. Alekseev, A. P. Dmitriev, I. V. Gornyi, V. Y. Kachorovskii, B. N. Narozhny, M. Schütt, and M. Titov, “Magnetoresistance in Two-Component Systems”, *Physical Review Letters* **114**, 15, 156601 (2015).

[18] H. Weiss and H. Welker, “Zur transversalen magnetischen Widerstandsänderung von InSb”, *Zeitschrift fur Physik* **138**, 3-4, 322–329 (1954).

[19] G. Y. Vasileva, D. Smirnov, Y. L. Ivanov, Y. B. Vasilyev, P. S. Alekseev, A. P. Dmitriev, I. V. Gornyi, V. Y. Kachorovskii, M. Titov, B. N. Narozhny, and R. J. Haug, “Linear magnetoresistance in compensated graphene bilayer”, *Physical Review B* **93**, 19, 195430 (2016).

[20] S. Adam, E. H. Hwang, V. M. Galitski, and S. Das Sarma, “A self-consistent theory for graphene transport.”, *Proceedings of the National Academy of Sciences of the United States of America* **104**, 47, 18392–7 (2007).

[21] E. V. Kurganova, S. Wiedmann, A. J. M. Giesbers, R. V. Gorbachev, K. S. Novoselov, M. I. Katsnelson, T. Tudorovskiy, J. C. Maan, and U. Zeitler, "Quantized coexisting electrons and holes in graphene measured using temperature-dependent magnetotransport", *Physical Review B* **87**, 8, 085447 (2013).

[22] X. Du, I. Skachko, A. Barker, and E. Y. Andrei, "Approaching ballistic transport in suspended graphene.", *Nature Nanotechnology* **3**, 8, 491–5 (2008).

[23] J. Crossno, J. K. Shi, K. Wang, X. Liu, A. Harzheim, A. Lucas, S. Sachdev, P. Kim, T. Taniguchi, K. Watanabe, T. A. Ohki, and K. C. Fong, "Observation of the Dirac fluid and the breakdown of the Wiedemann-Franz law in graphene.", *Science* **351**, 6277, 1058–61 (2016).

[24] M. I. Katsnelson, K. S. Novoselov, and a. K. Geim, "Chiral tunnelling and the Klein paradox in graphene", *Nature Physics* **2**, 9, 1986 (2006).

APPENDIX A

Conversion of capacitance data into DOS

In Chapter 4 we addressed the nature of the ground state at $\nu = 0$ and $\nu = \pm 1$ by means of capacitance spectroscopy. The analysis is based on the extraction of the chemical potential from the experimental data integrating the inverse of the quantum capacitance C_Q over the charge carrier density, as described by eq.4.1. This can be done easily provided that the values of C_G and C_P are known accurately. As described in section 2.4, C_G and C_P are the geometrical capacitance of the device and the parasitic capacitance (due to the experimental set up), which act in series and in parallel with C_Q, respectively. For a schematic representation of the circuit equivalent to the system, see Figure 2.9 (b).

As mentioned in Chapter 4 there is some uncertainty on the values of S (the area of the device), the dielectric constant of the thin layer of hBN and the parasitic capacitance C_P.

In this Appendix we report the procedure we use in order to extract the mentioned parameters from the experimental traces. We first describe how to calculate an effective dielectric constant of hBN for our devices and then how to obtain the values of C_G and C_P converting the capacitance traces into DOS.

We consider two different samples called A and B. The electronic properties of Sample A are described in Chapter 4, while the capacitance traces for Sample B are shown in Chapters 2 and 3.

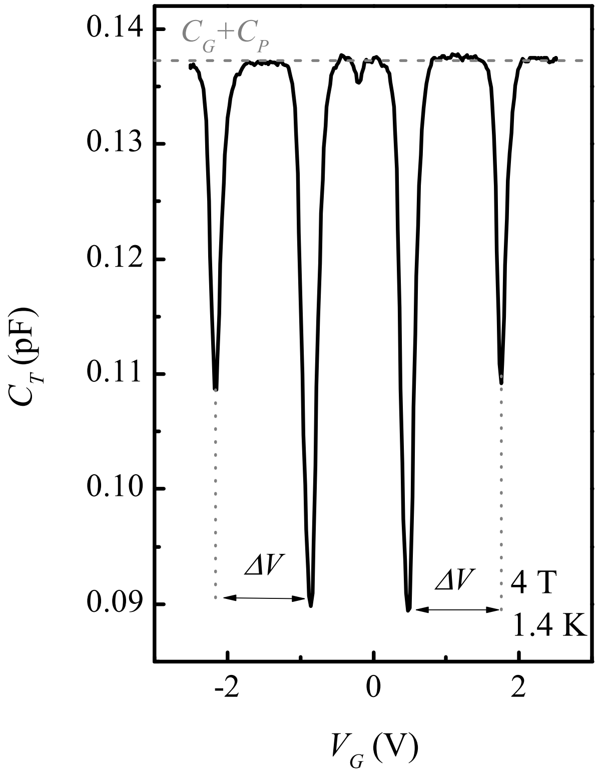

Figure A.1: *C_T as a function of the gate voltage for Sample A at 4 T and 1.4 K.*

A.1 Dielectric constant of hBN

The dielectric constant of the thin layer of hexagonal BN placed between the graphene and the Au electrode can be directly obtained from the periodicity in V_G of the quantum oscillations in a fixed perpendicular magnetic field $B_\perp$. At each integer ν, the carrier density n is known and given by

$$n = \frac{eB_\perp \nu}{h}. \tag{A.1}$$

If we consider two consecutive filling factor appearing as sharp minima in C_T, then the amount of charge necessary to fill a Landau level and change the filling factor by $\Delta\nu$ can be approximated by

$$\Delta n = \frac{C_G}{Se}\Delta V_G \tag{A.2}$$

where ΔV_G is the distance in gate voltage between two consecutive ν (see Figure A.1) and $C_G = \epsilon_0 \epsilon_{BN} S/d$ is the geometrical capacitance of the device modelled as a parallel plate capacitor. Combining the two equations we get that

$$\frac{V_G}{B_\perp} = \frac{e^2 d}{h \epsilon_0 \epsilon_{BN}} \nu. \tag{A.3}$$

Figure A.2(a) shows the gate voltage values normalized by the magnetic field for each filling factor. The solid lines are linear fits according to eq.A.3. The slope of those lines depends on the ratio d/ϵ_{BN}. Since the thickness of the hBN layer is known from AFM measurements, we can calculate the effective dielectric constant ϵ_{BN} for each magnetic field. The obtained values for Sample A are displayed in Figure A.2(b). ϵ_{BN} does not depend on the magnetic field and the value it is constant within the error bars. Performing an average over the different values obtained at different magnetic fields, we get $\epsilon_{BN} = 2.42$ for the considered sample. For sample B we obtain $\epsilon_{BN} = 2.58$.

Note that with this approach, we consider the position of the minima and not their absolute value, therefore, it is not affected by the uncertainty of C_P and C_G.

A.2 Determining C_G and C_P

Now the uncertainty is restricted to the value of S and C_P. In order to determine them, we follow a two step approach, illustrated in Figure A.3. In the first one, we obtain the value $C_G + C_P$. To this end, we fix C_G and we convert the data into density of states. We accept only the values of $C_G + C_P$ which lead to a linear shape of the DOS. The second step consists of varying S, and thus C_G, until the calculated DOS approaches the one of clean graphene (see Figure 2.2) and described by

$$DOS = \frac{8\pi|\mu|}{h^2 v_F^2}. \tag{A.4}$$

At the end of the procedure we have an unique set of values of C_P and C_G which allow us to preform a reliable calculation of the DOS and the chemical potential of our system. In what follows, we will describe in details the complete procedure.

The first step is to determine the value $C_G + C_P$. In an external magnetic field, the total capacitance of the devices approaches this value when the chemical potential crosses one highly populated Landau level (see the horizontal dashed line in Figure A.1). We choose an arbitrary a value of S such that $S_{min} \leq S \leq S_{max}$ (see the area difference in Figure 2.9) and we calculate $C_G = (S\epsilon_0\epsilon_{BN})/d$.

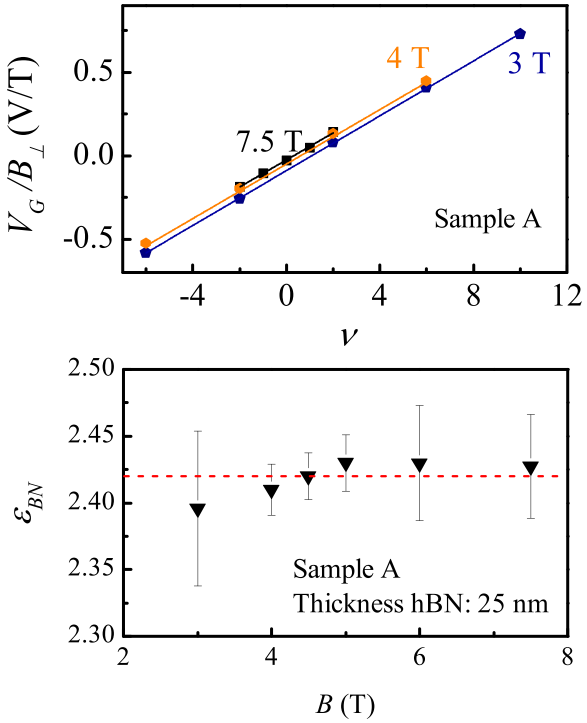

Figure A.2: *Calculation of the dielectric constant of hBN from the periodicity of the oscillations of C_T. (a): $V_G/B_\perp$ as a function of the filling factor for three different magnetic fields $B = 3$ T (blue symbols), $B = 4$ T (orange circles), and $B = 7.5$ T (black squares). The solid lines are liner fits to the experimental points. (b): value of the dielectric constant of hBN calculated for the different values of the external magnetic field $B_\perp$. The error bars are the one given by the linear fits. The red dashed line is the average value 2.42.*

While keeping C_G constant, we calculated the DOS for different values of C_P such that the sum $C_G + C_P$ is compatible with the background of the C_T traces in a quantizing magnetic field within the experimental uncertainty.

The result of these calculations are shown in Figure A.3 (a) and (c), for the two samples A and B, respectively. Each panel shows three different calculations of the DOS obtained using the same value of C_G but three different ones for C_P. The shape of the DOS changes considerably for small variations of C_P and we accept the value that leads to a linear DOS. In case of Sample A the linear DOS (black line in panel (a)) is obtained for $C_G + C_P = 0.137\,\text{pF}$, for sample B (black line in panel (c)) we get $C_G + C_P = 0.347\,\text{pF}$. The other values of $C_G + C_P$ are disregarded as they provide unphysical results (the orange and the green curves in both panels). As a result of this procedure, we obtain a DOS which is linear on the chemical potential away from the CNP ($\mu = 0$).

Once the sum $C_G + C_P$ is determined, we proceed with the second step. The slope of the linear part of the density of states depends on C_G, and thus on S. We calculate the DOS keeping $C_G + C_P$ constant and changing the area of the device S, and we compare it with the expected value according to eq.A.4. Figure A.3 (b) and (d) shows the outcome of this process. The red dashed lines represent the ideal DOS for graphene. For sample A the value $S = 187\,\mu\text{m}^2$ provides a good resemblance between the calculated DOS (black line in panel (b)) and its expected value. However, given the high noise present in the experimental data, a good agreement is provided also by other S values up to $S_{max} = 203\,\mu\text{m}^2$. As mentioned in section 4.2, we use both values when calculating the chemical potential and the energy gaps.

In case of Sample B, we get the experimental data follow the theoretical trace of the *DOS* for $S = 340\ \ \mu\text{m}^2$. The choice of a bigger (smaller) value leads to an increase (decrease) of the slope of the curves. Since the slope of the curves is related to the Fermi velocity, considering a different value of S leads, once again, to an unphysical result (orange and green curves in both panels (b) and (d)).

In this way we obtain reliably the parameters C_G (from S and ϵ_{BN}) and C_P that are necessary to calculate the chemical potential and the DOS reported in Chapter 4.

The described procedure relies on the assumption of resemblance between the experimental data and the theoretical calculation of the DOS. We also assume a constant value for the Fermi velocity $v_F = 1 \times 10^6\,\text{m/s}$. These assumptions are justified by several experimental works[1–4] confirming the linear relationship between DOS and chemical potential and the value for $v_F \approx 10^6\,\text{m/s}$.

Our approach, however, cannot take into account the re-normalization of the Fermi velocity due to electron-electron interactions which takes place a low charge carrier density[5,6] in high quality samples. Such effects produce a deviation from the linear behaviour in the DOS at low densities and an enhancement of v_F around the CNP. However, away from the CNP where we assume the linear dependence of the *DOS* over μ, these effects play a minor role and the value of v_F approaches a constant values determined by the slope of the linear part of the DOS.[6] Therefore, our procedure provides us with all the necessary parameters to perform a reliable conversion of the capacitance data into DOS.

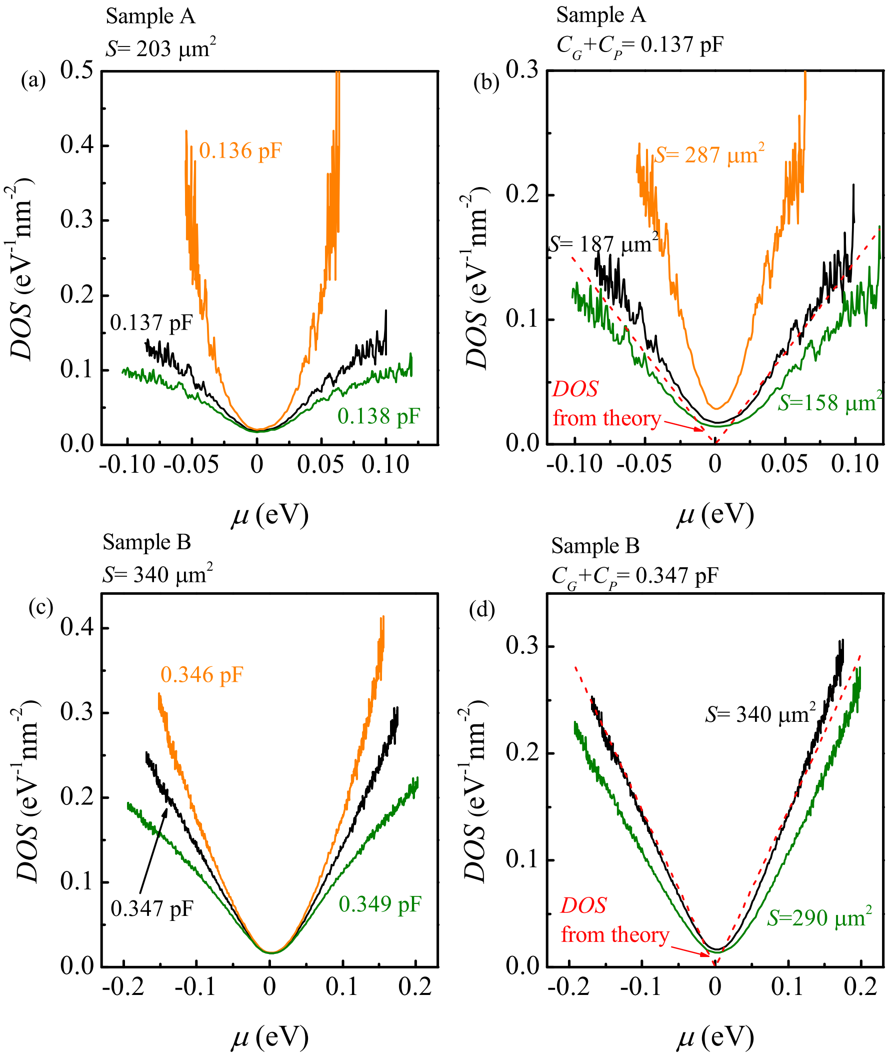

Figure A.3: *Procedure to extract C_G and C_P from the experimental data. Panels (a) and (c) depicts the first step of the procedure for sample A and B, panel (b) and (d) illustrate the second step. Density of states as a function of the chemical potential at zero magnetic field and 1.4 K. (a): the three traces are calculated having the same value of $S = 203\,\mu m^2$, and thus the same C_G, and changing C_P. The numbers close to each trace indicates $C_G + C_P$. (b): The traces are calculated keeping $C_G + C_P = 0.137\,pF$ constant and changing the value of S, which is reported close to each trace. The experimental DOS is compared with the red dashed line representing the expected DOS for clean graphene for $v_F = 1 \times 10^6$ m/s. (c) and (d) same as in panel (a) and (b), respectively but in the case of Sample B.*

References

[1] L. A. Ponomarenko, R. Yang, R. V. Gorbachev, P. Blake, A. S. Mayorov, K. S. Novoselov, M. I. Katsnelson, and A. K. Geim, "Density of states and zero Landau level probed through capacitance of graphene", *Physical Review Letters* **105**, 13, 136801 (2010).

[2] J. M. Xue, J. Sanchez-Yamagishi, D. Bulmash, P. Jacquod, a. Deshpande, K. Watanabe, T. Taniguchi, P. Jarillo-Herrero, and B. J. Leroy, "Scanning tunnelling microscopy and spectroscopy of ultra-flat graphene on hexagonal boron nitride", *Nature Materials* **10**, 4, 282–285 (2011).

[3] G. L. Yu, R. V. Gorbachev, J. S. Tu, a. V. Kretinin, Y. Cao, R. Jalil, F. Withers, L. a. Ponomarenko, B. a. Piot, M. Potemski, D. C. Elias, X. Chen, K. Watanabe, T. Taniguchi, I. V. Grigorieva, K. S. Novoselov, V. I. Fal'ko, a. K. Geim, and a. Mishchenko, "Hierarchy of Hofstadter states and replica quantum Hall ferromagnetism in graphene superlattices", *Nature Physics* **10**, 7, 525–529 (2014).

[4] G. Li, A. Luican, and E. Y. Andrei, "Scanning tunneling spectroscopy of graphene on graphite", *Physical Review Letters* **102**, 17, 176804 (2009).

[5] D. C. Elias, R. V. Gorbachev, a. S. Mayorov, S. V. Morozov, a. a. Zhukov, P. Blake, L. a. Ponomarenko, I. V. Grigorieva, K. S. Novoselov, F. Guinea, and a. K. Geim, "Dirac cones reshaped by interaction effects in suspended graphene", *Nature Physics* **7**, 9, 701–704 (2011).

[6] G. L. Yu, R. Jalil, B. Belle, A. S. Mayorov, P. Blake, F. Schedin, S. V. Morozov, L. a. Ponomarenko, F. Chiappini, S. Wiedmann, U. Zeitler, M. I. Katsnelson, a. K. Geim, K. S. Novoselov, and D. C. Elias, "Interaction phenomena in graphene seen through quantum capacitance.", *Proceedings of the National Academy of Sciences of the United States of America* **110**, 9, 3282–6 (2013).

Summary

This thesis presents an experimental study of the electronic properties and the Landau levels of graphene in high magnetic fields. By means of transport and capacitance measurements in high tilted magnetic fields, we address the spin polarization of the electronic states resulting from the splitting of the Landau levels (Chapters 3 and 4) and the effects of the Zeeman splitting on the transport properties of graphene (Chapter 5).

In this work, we consider devices made of graphene sandwiched between two thin layers of hexagonal boron nitride. In particular, we employ graphene based field effect transistors and capacitors. The devices are investigated at low temperatures (down to 1.4 K) and in high (tilted) magnetic fields. In a tilted field experiment, the sample is tilted with respect to the external magnetic field (B_T). The resistance or the capacitance of the devices is measured for different tilt angles θ having the perpendicular component of the magnetic field ($B_\perp = B_T \cos\theta$) fixed. This kind of experiments enables one to decouple the effects of the magnetic field on the orbital motion of the carriers (dependent only on $B_\perp$) from the effects related to the spin of the carriers (dependent on B_T).

The thesis begins with a general introduction (Chapter 1) which frames the research field and highlights the importance of high tilted magnetic field for these investigations.

In Chapter 2, we present the electronic properties of graphene and the devices used in the experiments. In particular, we describe the density of states of graphene and its Landau levels and we show how these can be addressed experimentally by means of the transport and capacitance measurements. The Landau levels are derived considering non interacting electrons obeying the Dirac Hamiltonian and, in this description, are four fold degenerate, reflecting the spin and valley degeneracy of the spectrum of the carriers in zero magnetic field. In addition, graphene presents a zero energy level equally populated by electrons and

holes. The degeneracy of the Landau levels is lifted by the Zeeman effect and by electron-electron interactions, thus, each level can split into four distinct ones. When the splitting occurs, new electronic states can be revealed by transport and capacitance measurements. In addition, Chapter 2 describes in more detail the devices (graphene based field-effect transistors and capacitors) used in the experiments, and the tilted field configuration.

Chapter 3 deals with the splitting of the Landau levels and the characterization of the electronic states resulting from it. Specifically, we investigate the states at filling factors $\nu = -1, -3, -4, -5, -7, -8$ and -12, which are observed as quantum Hall states in the transport measurements. By performing thermally activated transport, we extract the energy gaps associated to most of the filling factors, both in a purely perpendicular and a tilted magnetic fields. The tilted fields experiments show that the lowest energy Landau level behaves differently from all the other levels: whereas the higher levels have a spin polarized state at half filling ($\nu = -4, -8$ and -12), the spin polarized states in the lowest energy level occur at quarter filling ($\nu = \pm 1$). This result is supported qualitatively by the capacitance experiments performed on a different device. Moreover, the analysis of the size of the gaps shows that electron-electron interactions are the leading splitting mechanism in the lowest energy level, while the gaps at even filling factors in the higher levels ($\nu = -4, -8$ and -12) are compatible with the size of the single particle Zeeman effect.

In Chapter 4, we address the splitting of the lowest energy ($N = 0$) Landau level by means of capacitance spectroscopy. In this chapter, we extract quantitative information from the capacitance data and we calculate the density of states and the chemical potential of the system in zero and in a low perpendicular magnetic field magnetic field. The splitting of the $N = 0$ level occurs at $B_\perp \approx 4\,\mathrm{T}$, thus, the high magnetic fields available at the HFML enable us tilt the sample up to high angles ($\theta \approx 81^\circ$). At the lowest angles, the state at $\nu = 0$ is suppressed by the increase in the B_T, while the states at $\nu = \pm 1$ are enhanced. This indicates, in agreement with the findings of Chapter 3, that the states at $\nu \pm 1$ are spin polarized while the state at $\nu = 0$ is not. By tilting the device further, we observe a change in the spin polarization of the states when $B_T \simeq 5 \times B_\perp$. At the highest θ thus, the state $\nu = 0$ is enhanced by an increase in the external magnetic field, indicating that this state is spin-polarized.

Chapter 5 presents transport measurements in the presence of a large in-plane magnetic field. The device is tilted such that the B_T is almost parallel to the graphene plane. In this configuration, the field does not couple to the motion of the carriers, but induces the splitting of the density of states because of the Zeeman effect. We show that, despite the large size of the Zeeman splitting at $30\,\mathrm{T}$, the transport properties of graphene are not affected by a high magnetic field. The magnetoresistance observed at the charge neutrality point is found to be caused by the small $B_\perp$ resulting from a small ($< 0.1^\circ$) misalignment that cannot be avoided in these experiments. At the charge neutrality point, the device shows a finite quasiparticle density $n_\mathrm{Q} = 4.5 \times 10^{10}\,\mathrm{cm}^{-2}$, probably due to the presence of charge puddles, which is two orders of magnitude larger than the quasiparticle density induced by the Zeeman splitting of the density of states. We argue that the inhomogeneity of the sample resulting in a finite n_Q at the charge neutrality point hides the effects of the Zeeman splitting on the transport properties of the device.

Samenvatting

Dit proefschrift presenteert een experimentele studie van de elektronische eigenschappen en Landau niveaus van grafeen in hoge magneetvelden. Door middel van transport en capaciteit metingen in sterke, gekantelde magneetvelden, behandelen we de spin polarisatie van de elektronische toestanden resulterend uit het splitsen van de Landau niveaus (hoofdstukken 3 en 4) en de effecten van de Zeeman splitsing op de transporteigenschappen van grafeen (hoofdstuk 5).

In dit werk beschouwen we devices gemaakt van grafeen tussen twee dunne lagen hexagonaal boron nitride. In het bijzonder gebruiken we veldeffectransistoren en condensatoren. De devices worden onderzocht bij lage temperaturen (tot 1.4 K) en in hoge (gekantelde) magneetvelden. In een gekanteld veld-experiment wordt het sample gekanteld ten opzichte van het externe magneetveld (B_T). De weerstand of de capaciteit van de devices wordt gemeten bij verschillende kantelhoeken θ, waarbij de loodrechte component van het magneetveld ($B_\perp = B_T \cos\theta$) constant wordt gehouden. Dit soort experimenten stelt men in staat om de effecten van het magneetveld op de baanbeweging van de ladingsdragers (alleen afhankelijk van $B_\perp$) te ontkoppelen van de effecten die gerelateerd zijn aan de spin van de ladingsdragers (alleen afhankelijk van B_T).

Dit proefschrift begint met een algemene introductie (hoofdstuk 1), die het onderzoeksveld in een kader plaatst en de waarde van hoge, gekantelde magneetvelden voor deze onderzoeken belicht.

In hoofdstuk 2 presenteren we de elektronische eigenschappen van grafeen en de devices gebruikt in de experimenten. In het bijzonder beschrijven we de toestandsdichtheid van grafeen en zijn Landau niveaus en we laten zien hoe deze experimenteel kunnen worden behandeld door middel van transport en capaciteit metingen. De Landau niveaus worden afgeleid met niet interagerende elektronen in beschouwing, voldoen aan de Dirac hamiltoniaan en zijn in deze beschrijving viervoudig gedegenereerd, wat de spin en valley degeneratie van het spectrum van ladingsdragers in nul magnetisch veld weerspiegelt. Verder toont grafeen een nulenergie niveau dat in gelijke mate gevuld is met elektronen en met gaten. De degeneratie van de Landau niveaus wordt opgeheven door het Zeeman effect en door elektron-elektron interacties, zodat elk niveau kan opsplitsen in vier afzonderlijke. Wanneer dit opsplitsen plaatsvindt, kunnen de nieuwe elektronische toestanden onthuld worden door transport en capaciteit metingen. Bovendien beschrijft hoofdstuk 2 de devices (veldeffecttransistoren en condensatoren gebaseerd op grafeen) die gebruikt worden in de experimenten in meer detail, evenals de gekanteld veld-configuratie.

Hoofdstuk 3 gaat over het splitsen van de Landau niveaus en de karakterisatie van de elektronische toestanden die hieruit volgen. In het bijzonder onderzoeken we de toestanden bij filling factors $\nu = -1, -4, -5, -7, -8$ en -12, welke geobserveerd worden als quantum Hall toestanden in de transportmetingen. Door thermisch geactiveerd transport uit te voeren, bepalen we de energie gaps geassocieerd met de meeste filling factors, zowel in puur loodrechte velden als in gekantelde. De gekanteld veld-experimenten tonen aan dat het laagste-energie Landau niveau zich anders gedraagt dan al de andere: terwijl de hogere niveaus een spin gepolariseerde toestand hebben bij halve vulling ($\nu = -4, -8$ en -12), vinden de spin gepolariseerde toestanden in het laagste energieniveau plaats bij een kwart vulling ($\nu = \pm 1$). Dit resultaat wordt kwalitatief ondersteund door de capaciteit metingen uitgevoerd met een verschillend device. Bovendien toont de analyse van de grootte van de gaps aan dat elektron-elektron interacties het leidende splitsingsmechanisme zijn in het laagste energieniveau, terwijl de gaps bij even filling factors in de hogere niveaus ($\nu = -4, -8$ en -12) compatibel zijn met de grootte van het één-deeltje Zeeman effect.

In hoofdstuk 4 bespreken we het splitsen van het laagste-energie ($N = 0$) Landau niveau door middel van capaciteit specroscopie. In dit hoofdstuk halen we kwantitative informatie uit de capaciteit data en berekenen we de toestandsdichtheid en the chemische potentiaal van het systeem in nul en in laag loodrecht magnetisch veld. Het splitsen van het $N = 0$ niveau vindt plaats bij $B_{\perp} 4\,\mathrm{T}$, dus de hoge magneetvelden beschikbaar bij het HFML stellen ons in staat om het sample tot grote hoeken te kantelen ($\theta \approx 81°$). Bij de laagste hoeken wordt de toestand bij $\nu = 0$ onderdrukt door de toename in B_T, terwijl de toestanden bij $\nu = \pm 1$ worden versterkt. Dit betekent, in overeenkomst met de vindingen uit hoofdstuk 3, dat de toestanden bij $\nu = \pm 1$ spin gepolariseerd zijn terwijl de toestand bij $\nu = 0$ dat niet is. Wanneer we het device verder te kantelen, observeren we een verandering in de spin polarisatie van de toestanden als $B_T \simeq 5 \times B_{\perp}$. Bij de hoogste θ wordt dus de toestand $\nu = 0$ versterkt door een toename van het externe magnetisch veld, wat aantoont dat deze toestand spin gepolariseerd is.

Hoofdstuk 5 presenteert transport meting in de aanwezigheid van een sterk magneetveld in het vlak. Het device is zodanig gekanteld dat B_T bijna parallel is aan het grafeen vlak. In deze configuratie koppelt het veld niet aan de beweging van de ladingsdragers, maar induceert het splitsing van de toestandsdichtheid door middel van het Zeeman effect. We laten zien dat, ondanks de grote Zeeman splitsing bij 30 T, de transporteigenschappen van grafeen niet worden beinvloed door een hoog magneetveld. Er wordt gevonden dat de magnetoweerstand geobserveerd bij het ladingsneutraliteitspunt veroorzaakt wordt door de kleine $B_\perp$ die het resultaat is van de kleine ($< 0.1^\circ$) uitlijningsfout die niet vermeden kan worden in deze experimenten. Bij het ladingsneutraliteitspunt toont het device een eindige quasideeltjesdichtheid $n_\mathrm{Q} = 4.5 \times 10^{10}\,\mathrm{cm}^{-2}$, waarschijnlijk door de aanwezigheid van zogenaamde “charge puddles”. Dit is twee ordes van grootte meer dan de quasideeltjesdichtheid geïnduceerd door de Zeeman splitsing van de toestandsdichtheid. We beargumenteren dat de inhomogeniteit van het sample, die resulteert in een eindige n_Q bij het ladingsneutraliteitspunt, de effecten van Zeeman splitsing op de transporteigenschappen van het device verbergt.

Curriculum Vitae

Francesca Chiappini

1987	Born on 22 November in Genoa, Italy
2001-2006	Student at Liceo Classico C. Colombo
2006-2009	Bachelor's Degree in Physics at Università degli Studi di Genova, Genoa, Italy
2009-2012	Master's Degree in Physiscs at Università degli Studi di Genova, Genoa, Italy
2012-2016	PhD student at High Field Magnet Laboratory, Radboud University, Nijmegen, The Netherlands
2016-present	Trainee at TNO, Delft, The Netherlands

List of publications

- F.Chiappini, S. Wiedmann, M. Titov, A. K. Geim, R. V. Gorbachev, E. Khestanova, A. Mishchenko, K. S. Novoselov, J. C. Maan, and U. Zeitler *"Magnetotransport in single-layer graphene in a large parallel magnetic field"*, Physical Review B **94**, 085302 (2016).

- F. Chiappini, S. Wiedmann, K. Novoselov, A. Mishchenko, A. K. Geim, J. C. Maan, and U. Zeitler *"Lifting of the Landau level degeneracy in graphene devices in a tilted magnetic field"*, Physical Review B **92**, 201412(R) (2015).

- G. L. Yu, R. Jalil, B. Belle, A. S. Mayorov, P. Blake, F. Schedin, S. V. Morozov, L. A. Ponomarenko, F. Chiappini, S. Wiedmann, U. Zeitler, M. I. Katsnelson, A. K. Geim, K. S. Novoselov, and D. C. Elias *"Interaction phenomena in graphene seen through quantum capacitance"*, PNAS **110**, 9, 3282-6 (2013).

- M. Petrushevsky, E. Lahoud, A. Ron, E. Maniv, I. Diamant, I. Neder, S. Wiedmann, V. K. Guduru, F. Chiappini, U. Zeitler, J. C. Maan, K. Chashka, A. Kanigel, and Y. Dagan *"Probing the surface states in Bi_2Se_3 using the Shubnikov-de Haas effect"*, Physical Review B **86**, 045131 (2012).